

Plasma cleaning of diagnostic first mirrors for the nuclear fusion machine ITER

INAUGURALDISSERTATION

zur

Erlangung der Würde eines Doktors der Philosophie

vorgelegt der

Philosophisch-Naturwissenschaftlichen Fakultät

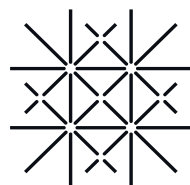
der Universität Basel

von

Lucas Moser

aus Frankreich

Basel, 2017



**University
of Basel**

Genehmigt von der Philosophisch-Naturwissenschaftlichen Fakultät
auf Antrag von:

Dr. Laurent Marot
Prof. Dr. Ilaria Zardo
Prof. Dr. Ernst Meyer

Basel, den 20.06.2017

Prof. Dr. Martin Spiess, Dekan

“Logic will get you from A to B. Imagination will take you everywhere.”
A. Einstein

To Ondine, Margot and ...

Abstract

FIRST Mirrors (FMs) will play a crucial role in optical diagnostic systems of future fusion devices like the International Thermonuclear Experimental Reactor (ITER). Unlike today's tokamaks, forthcoming reactors are expected to produce a high level of radiations and neutrons, preventing the use of common optical components (windows, fibers). Instead, an alternative solution based on an optical labyrinth embedded in the neutron shielding and employing metallic mirrors was proposed. Being the first element of the optical path which allows light to cross the neutron shielding, FMs will be placed close to the thermonuclear plasma and will, therefore, be subject to intense thermal and radiations loads, bombardment by plasma particles (mainly charge-exchange neutrals, CXNs) and deposition of material eroded from the plasma-facing components. Especially net deposition of particles eroded from the First Wall (FW), i.e. mainly beryllium (Be) and tungsten (W), can degrade the reflectivity of FMs severely compromising the reliability of the optical diagnostics. Although passive mitigation techniques are predicted to reduce the amount of Be and W on FMs, optical degradation cannot be fully suppressed; in situ mirror cleaning techniques are indispensable. Discharge plasma cleaning is currently considered as the most promising method to tackle this issue.

The main goal of this thesis is to provide an exhaustive study of plasma cleaning techniques of FMs in conditions as close as possible to future fusion reactors. To obtain suitable results for the fusion community and in particular for ITER, experiments were not only conducted in the University of Basel but in numerous international facility as the Swiss Plasma Center in Lausanne, the Paul Scherrer Institute in Villigen, the National Institute for Laser, Plasma and Radiation Physics (INFLPR) in Bucharest or in two tokamaks, the Joint European Torus (JET) and the Experimental Advanced Superconducting Tokamak (EAST), respectively located in England and China.

Significant outcomes have been obtained from the experimental investigations. Several types of plasma generation processes were considered and one of them exhibited very promising results, namely capacitively coupled radio-frequency (RF) discharge. Different types of deposits, trying to mimic the one that could be found in ITER were obtained by magnetron sputtering technique and intensively studied. Cleaning tests done on typical ITER contaminant material (Be or W) as well as on a Be proxy (Be is toxic), aluminium (Al), either in pure or mixed thin films, obtained from existing tokamak or deposited in laboratory showed very promising results.

After that, cleaning experiments using larger mirrors up to $200 \times 300 \text{ mm}^2$, approaching the final design of ITER's edge Thomson scattering (ETS) FM, were performed in Basel and provided encouraging results. Despite the type of dielectric properties of the mirror's surface (conducting, insulating or half-insulating/half-conducting) the cleaning process systematically exhibited homogeneous etching over the surface. Furthermore, as a strong magnetic field (up to 3.5 T on the mirror locations) will be present in ITER, a thorough experimental investigation

Contents

on the effect of external B-field on the etching proprieties was conducted. The strength (up to 3.5 T) and orientation of the B-field to the normal of the mirror surface (from 0 to 90°) were shown to be parameters strongly affecting etching rate and homogeneity of the cleaning process. With the B-field being always more tangential to the surface, the etching was getting more and more inhomogeneous. When the B-field was at 90°, e.g. parallel to the surface, the sputtering was impossible on half the mirror. This observation led to a major review of some ITER diagnostics designs with all first mirrors being now repositioned to have a maximum angle of 85° between their normal and the B-field. The first ever cleaning trials in an existing tokamak (EAST) performed on the ETS mock-up will be introduced.

Finally, in the optic of in situ RF plasma cleaning integration in ITER, extensive work was started on the so-called driven grounded electrode technique, where the idea is to ground (e.g. short-circuit) the FMs to ease the implementation in ITER.

Contents

Abstract	i
Introduction	1
1 First Mirrors for nuclear fusion reactor	5
1.1 Nuclear fusion on Earth	5
1.2 Tokamaks and ITER	7
1.3 First mirrors for optical diagnostic systems in ITER	10
1.3.1 Optical plasma diagnostics	10
1.3.2 First mirrors	12
1.3.3 Plasma Erosion	12
1.3.4 Deposition	13
1.4 Mitigation and recovery techniques	15
1.4.1 Mitigation	15
1.4.2 Recovery	15
2 Theoretical background	19
2.1 Low-temperature plasma	19
2.2 Capacitively coupled RF plasma	20
2.3 Driven grounded electrodes in CCP	22
2.4 Plasma in magnetic field	24
2.4.1 Single particle motion	24
2.4.2 Magnetized plasma	25
2.5 Sputtering	26
3 Experimental	31
3.1 Plasma exposure facilities	31
3.1.1 ESCA-1 facility	31
3.1.2 Be chamber	33
3.1.3 B-field Chamber	34
3.2 Sample characterization	34
3.2.1 Photoelectron spectroscopy	35
3.2.2 Scanning electron microscopy	36
3.2.3 Optical techniques	38
3.2.4 Other characterization methods	40
3.3 Plasma characterization	41

Contents

3.4	Deposits on FM: coating technique	41
3.4.1	Physical Vapor Deposition	42
3.4.2	Sample preparation	42
3.4.3	Magnetron sputtering	42
4	Plasma cleaning techniques	45
4.1	Selection of the most appropriate cleaning technique	45
4.1.1	Plasma cleaning procedure	45
4.1.2	External plasma source	46
4.1.3	Kaufman source	48
4.1.4	Capacitively coupled plasma	48
4.1.5	Summary	48
4.2	CCP: discharge properties	48
4.2.1	Influence of discharge parameters	49
4.2.2	Effect of the wall area	51
4.2.3	Influence of driven electrode area	53
4.2.4	Spatial homogeneity of a discharge	54
4.2.5	Driven grounded electrode	55
4.2.6	Influence of magnetic field	59
5	Influence of deposits	61
5.1	Laboratory deposits	61
5.1.1	Production of contaminants film	61
5.1.2	Cleaning of Al/W based deposits	62
5.1.3	Be/W based laboratory deposits	66
5.2	Tokamak deposits	75
5.2.1	Mirrors in JET-ILW tokamak	75
5.2.2	Cleaning in the Be chamber	77
5.3	Summary	79
6	Plasma cleaning in ITER-like conditions	81
6.1	Influence of size on the homogeneity	81
6.1.1	48 mm diameter mirror	81
6.1.2	98 mm diameter mirror	84
6.1.3	Edge Thomson scattering mirror mock-up	84
6.2	Plasma cleaning in the presence of a B-field	86
6.2.1	Cleaning in the B-field chamber	86
6.2.2	Cleaning in EAST tokamak	92
6.3	Driven grounded electrode configuration	93
6.3.1	48 mm diameter mirror	93
6.3.2	Edge Thomson scattering mirror mock-up	94
6.3.3	Oblique and high B-field: $\alpha = 85^\circ$, $+/-3.5$ T	96
6.3.4	Integration in ITER	97
6.4	Double electrode	97
6.4.1	Phase shift influence	98
6.4.2	Etching profiles	98
7	Conclusions and perspectives	101
7.1	Summary	101
7.2	Guidebook	103
	Bibliography	A
	List of symbols & abbreviations	I

Acknowledgements	K
List of publications & communications	M

Introduction

IN the near future, the growth of the world population accompanied by better living standards will lead to a strong increase in energy consumption. Yet, 80 % of the energy comes from fossil fuels, accompanied with severe environmental and geopolitical problems posing a serious threat to humanity. Among those, emission of greenhouse gases, responsible for global warming, destruction of precious ecosystems or geopolitical instabilities, only represent the pit of the iceberg. Although developments in the field of renewable energy exhibit more and more efficient devices, it is unlikely that a single technology will fulfil the world demand. The best way to address those issues while taking care of sustainability and environmental protection would be to consider a mix of power sources based on renewables and to combine them, in the near future, with nuclear fission to reduce greenhouse emissions as fast as possible. Still, for the latter, recent incidents and issues attributed to radioactive waste management have posed serious concerns regarding nuclear fission as long term prospect.

Nuclear fusion is, on the other side, and extremely attractive solution for future generations for several reasons. Firstly, fusion power will not emit greenhouse gases and works with cheap and quasi-unlimited fuel located everywhere around the globe. Also, fusion reactor will solely produce short-lived radioactive waste (recyclable within 100 years) and are inherently safe.

The driving idea of scientists working in nuclear fusion was to reproduce on Earth what makes our Sun shine. Currently, more than 35 countries are represented in the ITER project with a budget of about 15 billion euro. The construction is ongoing in Cadarache (France) with a first plasma expected in 2025 and a deuterium-tritium (D-T) phase planned for 2035. The main goal of ITER is to demonstrate a positive energy output from fusion reactions, opening the path for commercial reactors.

For the success of this project, proper control of the fusion plasma is mandatory to reach the ambitious objectives set while preserving the machine's integrity which requests a large number of plasma diagnostic systems. One class of diagnostic is especially important for ITER: optical diagnostic systems. Due to the large neutron flux expected in ITER, regular windows or fibre optics are unusable and were replaced by so-called metallic FMs embedded in the neutron shielding, forming an optical labyrinth. The light emitted by the plasma will thus be transmitted by a chain of mirrors towards detectors while the radiological shielding will stop neutrons. Being the first element of the optical path, a high and calibrated transmission of light is mandatory to improve both sensitivity and accuracy of the optical diagnostics to ensure well-controlled fusion reactions. Therefore one main requirement for these FMs is the ability to reflect stray light to the next mirror with as small losses as possible during the whole ITER operation time. Due to their close position to the fusion plasma, FMs will suffer from high particle fluxes (CXNs and neutrons, ultraviolet, X-ray and gamma radiations) leading to erosion and/or deposition. To avoid high CXNs flux, FMs were retrieved as far as possible from the FW and the main

concern for FMs reflectivity is now the deposition of impurities sputtered from the main wall of ITER, i.e. mainly Be [1, 2]. Based on predictions, 30 optical diagnostic systems, operating in the UV/Vis range, will be directly affected by this phenomenon potentially leading to a strong decrease of the optical properties of FMs and will require mirror surface recovery techniques. Two of them are worthy of interest: laser and plasma cleaning where the latter is considered as the most promising method to remove contaminants from FMs [3, 4].

This doctoral thesis was performed in close collaboration with the diagnostic team of the ITER Organization and aimed at the development of RF plasma cleaning of FMs in ITER relevant conditions, the final objective being the implementation of this technique in all optical diagnostic systems requiring active deposition mitigation techniques. Based on the results obtained in this thesis and by other groups, RF plasma cleaning technique is already foreseen in several diagnostics such as Thomson Scattering (TS) [5] or Charge-eXchange Recombination Spectroscopy (CXRS).

A basic introduction to nuclear fusion on earth, with specific attention paid to magnetic confinement, to the *tokamak* concept, and to ITER will be given in Chapter 1. The problem of FMs in optical diagnostic systems regarding erosion and contaminant deposition will be addressed, emphasizing the deposition issue and giving potential cleaning techniques.

The principal cleaning technique employed in this work is based on plasma sputtering and is created in a capacitively coupled plasma (CCP) mode. The necessary theoretical notions in plasma physics relevant to this work will be introduced in Chapter 2. As this thesis was based on an experimental approach, the main characterization methods and various systems used to conduct experiment campaigns will be described in Chapter 3.

Plasma sputtering can be performed with numerous methods where the driving idea is always the same: excitation of gas to generate a plasma and acceleration of ions towards the sample to cause sputtering. Typically, this can be achieved by employing an external plasma source with a bias applied to the target, or by supplying alternative current (AC) or direct current (DC) directly to the sample with creation of a plasma and simultaneous acceleration of ions (DC glow discharge, CCP ...). One other solution to sputter a surface consists of using an ion beam that could be neutralized by an electron source. ITER-relevant contaminants were etched using different sputtering methods and based on the results presented in Chapter 4, the most adequate cleaning technique for ITER, namely CCP, was chosen and further investigated. With this method, also labelled as in situ RF plasma cleaning, RF is directly applied to the electrode (in our case the mirror to clean) and the specific discharge configuration leads to the formation of the so-called self-bias, influencing the ion energy distribution on the mirror. Because the discharge properties (ion energy, density ...) strongly influence the cleaning process, the impact of several parameters such as pressure, excitation frequency and power or geometrical configurations of the electrodes were thoroughly analysed in the second part of Chapter 4. In addition, this chapter includes first results obtained in a specific case: the driven grounded electrode mode. Indeed, this configuration eases the integration in ITER as will be shown in Chapter 6.

To confirm the viability of in situ RF plasma cleaning for ITER FMs, one should prove that ITER-relevant contaminants can effectively be removed while preserving the optical properties of the mirrors. Two main experimental campaigns were therefore conducted and presented in Chapter 5. The first one was based on Al, used as a Be proxy due to the toxicity of the latter. Several types of contaminant films covering the wide range of deposit types found in existing tokamaks (dense, porous, insulating, conducting) were deposited on molybdenum (Mo) mirrors in laboratory and successively cleaned. Based on the promising results obtained with Be proxy, a second cleaning campaign was performed on Be and W laboratory-made deposits as well as on tokamak deposits from JET ITER-Like Wall (JET-ILW) in a specific chamber built for this purpose.

In situ RF plasma cleaning should not only be effective in the removal of ITER-relevant contaminants, it should also work for large FMs in ITER environment. Indeed, FMs can be, for example, as large as $410 \times 210 \text{ mm}^2$ in the Core Plasma Thomson Scattering (CPTS), in complex geometries (one mirror facing the other) and positioned in locations with magnetic fields up to

3.5 T. To validate in situ RF plasma cleaning for ITER, tests were conducted on real-size FM mock-ups or in the presence of 3.5 T magnetic fields and are described in Chapter 6. This chapter also includes an implementation scheme for ITER as well as ITER relevant experiments such as cleaning in the driven grounded electrode case or double electrode configuration. Besides, the first cleaning trials in an existing tokamak (EAST) are presented.

Finally, Chapter 7 presents the main conclusions of this work with perspectives regarding future developments.

The thesis work has offered 5 articles [6–10] to the scientific community under the first authorship of Lucas Moser. Please cite these articles instead of the thesis.

Enjoy reading this thesis!

First Mirrors for nuclear fusion reactor

In this chapter, the fundamental concepts of nuclear fusion on earth and especially for ITER will be introduced. The first section (1.1) will focus on the basic principles of fusion, energy balance of such reactions as well as mean to confine them. In the continuation of the first chapter, magnetic confinement via devices called *tokamaks* will be described (1.2) with particular attention given to the future reactor currently under construction: ITER. To achieve a safe operation and control of the nuclear fusion process, tens of diagnostics are necessary for ITER (1.3). Essential components of optical diagnostic systems are FMs, one of the big challenges that the fusion community has still to address. As will be shown later, the interaction of the fusion plasma with FMs can lead to severe degradation of their optical properties, posing a serious threat to reliability and usefulness of spectroscopic diagnostic systems. Deposition of impurities sputtered from the main wall is assumed to be the main concern for FMs. Mitigation and in situ cleaning techniques have to be developed, which represents the main topic of this Ph.D. thesis (1.4).

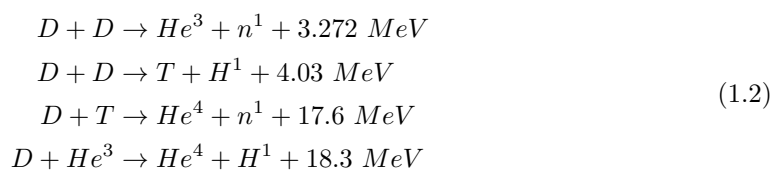
1.1 Nuclear fusion on Earth

Basic principle

Nuclear fusion reaction is a process in which two atoms fuse together to form a heavier nucleus. This reaction releases energy E , given by the famous equivalence between energy and mass postulated by Einstein:

$$E = \Delta mc^2 \quad (1.1)$$

where c is the speed of light and Δm stands for the mass defect. However, before the fusion can take place, the nuclei which are supposed to join have to overcome a large energetic barrier, the Coulomb repulsion, due to the positive charges of the nuclei which are repulsing each other. To overcome the Coulomb barrier, the reactants need to be at very high temperatures, typically above 100 million Kelvin. As the Coulomb barrier increases with atomic number, fusion reactions based on hydrogen (H) isotopes containing only a single positive charge are the most favourable reaction for commercial energy production. Equation 1.2 gives some of the most interesting fusion reactions with H isotopes:



A large choice of reaction is thus possible, but each reaction does not have the same probability to occur. This probability is a factor of the cross-section of each reaction. Figure 1.1 gives the cross section of the above reactions versus the light particle energy (D). It appears that the D–T reaction is the most attractive due to a higher cross section, a low energy required to make the reaction possible and a significant energy release (17.6 MeV). With helium (He), the D–He³ would also be interesting for fusion, but He³ is extremely rare on Earth. The D–T reaction is therefore envisaged for future fusion reactors. The released energy comprises an α particle (He^{2+} , 3.5 MeV) and an energetic neutron (14.1 MeV).

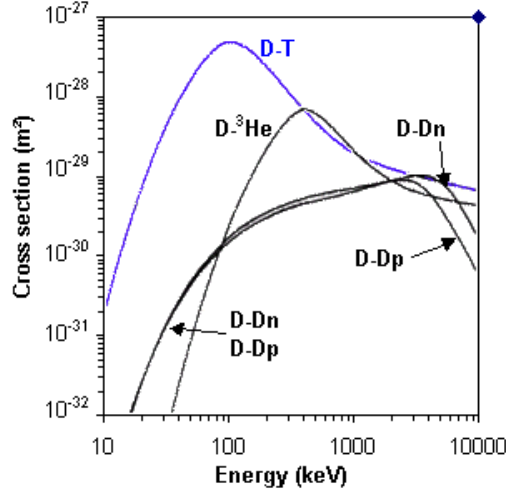


Figure 1.1: Fusion reactions cross sections as a function of particle energy. *n* and *p* stand for neutron and proton.

As stated above, very high temperatures (10 keV) are required for fusion and in those conditions, the fuel (D–T) is fully ionized in a quasi-neutral gas called plasma. Hence, the mixtures will be composed of charged particles (ions and electrons) that respond to electromagnetic fields. This specificity is employed to control the plasma and will be introduced later.

Energy balance

The neutrons produced by the reaction will leave the plasma almost without interactions, whereas the α particles which are charged, transfer their energy and heat up the plasma through collisions. During the fusion, a part of the energy will be lost, mainly through radiative processes such as Bremsstrahlung or diffusion and is labelled P_{loss} . To compensate for these losses, external heating can be provided to the plasma, P_{heat} . The total power balance in a steady-state plasma can be written as:

$$P_{loss} = P_{\alpha} + P_{heat} \quad (1.3)$$

where P_{α} represents the total α -particle heating. The efficiency of the reactor is given by Q , the ratio between the thermonuclear power produced and the heating power supplied.

$$Q = \frac{P_{\alpha}}{P_{heat}} \quad (1.4)$$

Break-even is reached for $Q = 1$, and when the energy losses are entirely compensated by the energy provided by the α particles and need no additional heating, $Q \rightarrow \infty$ and the plasma reached the ignition point and is self-sustained.

Confinement regimes

According to Lawson criterion [11], the ignition for a temperature of 10 keV is obtained if:

$$n\tau_E > 10^{20} \text{m}^{-3} \text{s} \quad (1.5)$$

where n is the plasma density and τ_E is the energy confinement time. This condition can be satisfied with two different approaches, either by creating a very dense plasma for a short time or by having a less dense plasma for a longer period. Two different approaches can satisfy the Lawson criterion:

- **Inertial confinement** This method is based on high plasma densities ($\approx 10^{31} \text{m}^{-3}$) and extremely low confinement times ($\approx 10^{-11} \text{s}$). This is achieved by strongly compressing fuel pellets with high-energy laser or particle beams. More information can be found in [12].
- **Magnetic confinement** The second approach is based on magnetic confinement of the plasma as it is made of charged particles. Longer confinement times are thus achieved (several seconds) and hence, lower plasma densities are requested (10^{20}m^{-3}). This method is the one currently envisaged in ITER.

1.2 Tokamaks and ITER

The tokamak

The word tokamak comes from the Russian acronym *toroidal'naya kamera s magnitnymi katushkami* (Toroidal Chamber in Magnetic Coils) is a device based on magnetic confinement and a schematic view of it is presented in Figure 1.2. The plasma is confined in a donut-shaped vacuum vessel by generating a strong toroidal magnetic field using external poloidal wound magnetic coils. As the sole toroidal field is not uniform within the major radius, the resulting $\nabla\mathbf{B}\times\mathbf{B}$ drift separates ions and electrons, thus creating a vertical electric field. The motion of the charge carriers leads to an $\mathbf{E}\times\mathbf{B}$ outward drift. One way to overcome this problem is to twist the field lines by adding a poloidal component to the toroidal field, leading to a helical B field. This is achieved by running a toroidal current into the plasma itself. The plasma current is driven by transformer action using a solenoid placed in the middle of the torus. The inner poloidal field coils work as the primary and the plasma as secondary transformer circuit. The device based on this magnetic field configuration is the tokamak. Finally, the shape of the plasma can be controlled by additional coils.

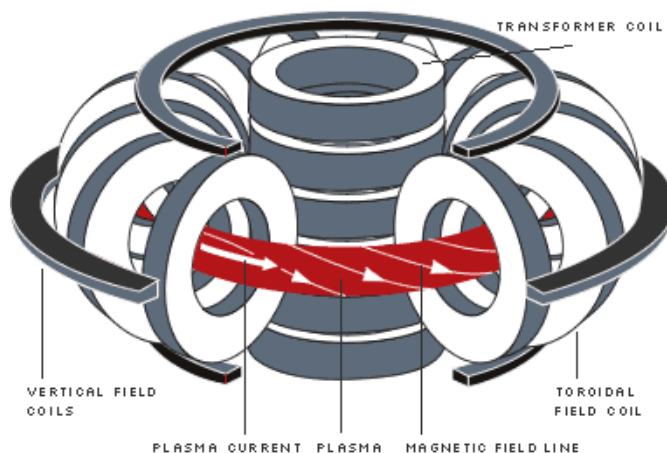


Figure 1.2: Schematic view of a tokamak.

To bring enough heat to the fuel mixture, the first step is to use ohmic heating. As the temperature of the plasma increases, the ohmic heating becomes less efficient and therefore, additional heating sources are necessary. Injection of energetic neutral beams or resonant absorption of radio-frequency electromagnetic waves are employed in nowadays tokamaks.

Two different approaches were developed to minimize and control plasma-wall interactions in a tokamak. The first method employs a so-called limiter, limiting the plasma radius physically. The second method uses an external magnetic field to create an X-point where the poloidal magnetic field vanishes (see Figure 1.3). The outermost poloidal field lines are opened and diverted toward toroidally symmetric plates: the divertor target. The scrape-off layer which contains the major fraction of impurities is thus directed towards the divertor targets. In the divertor configuration, the plasma surface interactions occur away from the confined fusion plasma (on the divertor targets) and this configuration was therefore chosen in modern tokamaks and ITER. More information regarding edge plasma physics can be found in [13].

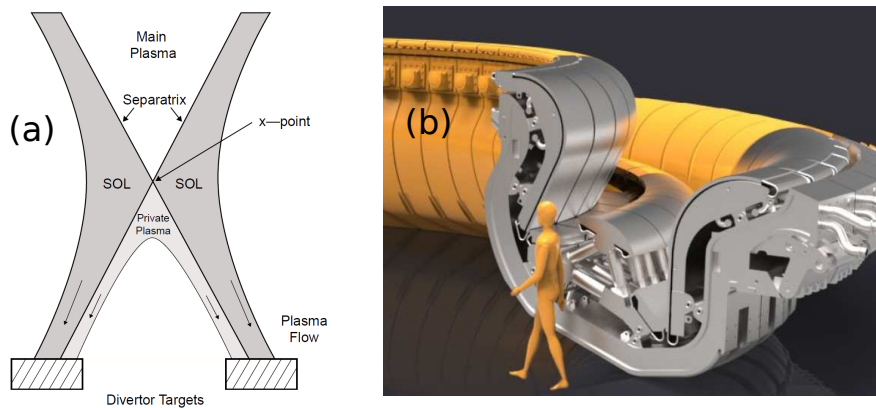


Figure 1.3: Plasma configuration in correspondence of the divertor region [13] and (b) ITER divertor design [14].

ITER

Most present tokamaks operate with deuterium fuel due to safety issue inherent to tritium. Only two reactors, the Tokamak Fusion Test Reactor and JET respectively located in the USA and UK, operated with a mixture of D-T. The former achieved $Q \approx 0.27$ in 1994 while $Q \approx 0.65$ were achieved in JET in 1997, the all-time record for magnetic confinement fusion. ITER, which also means “The Way” in Latin, is an international tokamak designed to demonstrate the potential for commercial fusion energy, producing 500 MW of fusion power for 400 seconds [14]. Some of the expected objectives which should be reached in ITER are:

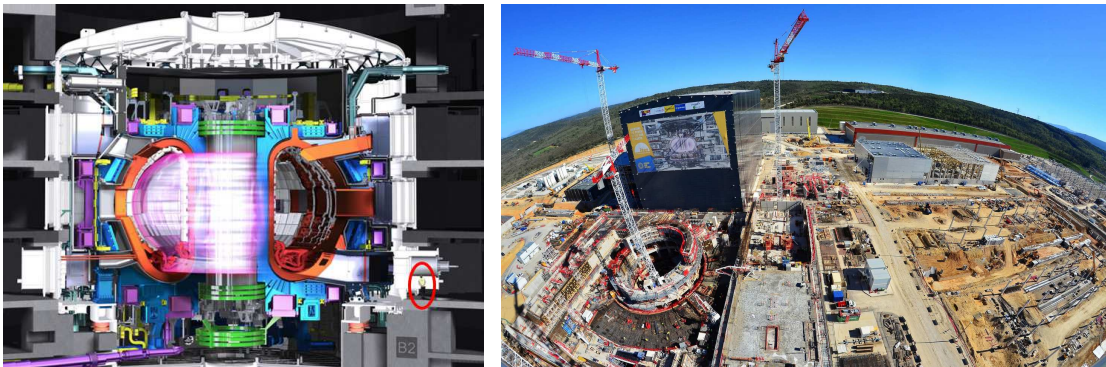
- Production of a steady-state plasma with $Q \geq 10$.
- Development of technologies and processes needed for a fusion power plant.
- Achieve a D-T plasma sustained through internal heating
- Test tritium breeding: because of the limited availability of tritium, it should be produced in ITER through the interaction of escaping neutrons with lithium.

The main parameters of ITER are listed in Table 1.1 as defined in [15].

A schematic view of the ITER tokamak is shown in Figure 1.4. The first plasma is expected for 2025 and the beginning of D-T operation is planned for 2035. Construction started a few years ago and showed important progress over the past months (see Figure 1.4).

Table 1.1: *Main parameters of ITER*

Total fusion power	500 MW
Gain factor Q	≥ 10
Plasma major radius	6.2 m
Toroidal field	5.3 T
Plasma current	15 MA
Average 14.1 MeV neutron wall loading	0.57 MW/m ²
Plasma volume	840 m ³
Plasma surface	678 m ²
Auxiliary heating power	73 MW
Plasma burning time	≥ 400 s

**Figure 1.4:** *Schematic of the ITER tokamak and latest view of the construction site located in Cadarache, France. Images are taken from [14].*

Diagnostic systems are essential to monitor and control the fusion reaction within ITER. The full range of plasma parameters will be covered by different types of diagnostics: magnetic, neutronic, electrostatic, optical ... Due to their importance for this work, optical diagnostic systems and inherent issues associated to FMs will be presented in 1.3.

Material choice for Plasma Facing Components (PFC)

The selection of the materials directly facing the plasma has to fulfil two important requirements. The first is the minimization of the contamination of the plasma by impurities and the second is a high component lifetime. Therefore, for the FW (area of about 700 m²) Be was chosen. In fact, Be ensures low fuel retention and low *Bremsstrahlung*, is a very good oxygen getter and has a good thermal conductivity. Nevertheless, D-T and He have a non-negligible sputtering yield on Be and Be has a low melting point (1560 K), and W was preferred to Be for the divertor region. Indeed, W is a high-Z material with a low sputtering yield, a high melting temperature (3695 K) and can thus handle high fluxes of particles and heat loads expected in the divertor regions. The plasma will therefore contain Be and W impurities eroded from the FW. The layout of the PFC is shown in Figure 1.5.

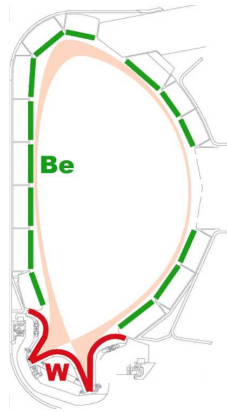


Figure 1.5: Cutaway showing the layout of the Plasma Facing Components in ITER with the selected materials.

1.3 First mirrors for optical diagnostic systems in ITER

1.3.1 Optical plasma diagnostics

As mentioned earlier, many diagnostics will be employed in ITER to ensure a controlled fusion reaction. ITER will have 50 diagnostics where almost all of them are used for real-time operation of the tokamak [16]. An overview of the whole diagnostic set-up is shown in Figure 1.6. Although this overview depicts a picture with lot of empty space, the real situation is much more complex and crowded as diagnostics sit in between the FW and the Vacuum Vessel.

Among all types of diagnostics, optical diagnostics are of prime importance as they allow to determine fundamental plasma parameters such as electron temperature or density, effective atomic number as well as impurity concentration. They are sorted as passive or active spectroscopic systems, depending on the measurement process. An example of optical diagnostic is the Thomson Scattering. This diagnostic is based on the interaction of free charges with radiations, exploiting the elastic scattering process between a high power laser and electrons, allowing one to determine T_e . In current tokamaks, optical diagnostic systems are collecting light from the plasma through optical windows or optical fibers. Nevertheless, ITER is planned to maintain plasma discharges for up to several hundreds of seconds at very high temperatures, leading to a high level of neutron production as well as gamma, UV and X-ray radiations. Typically, the flux

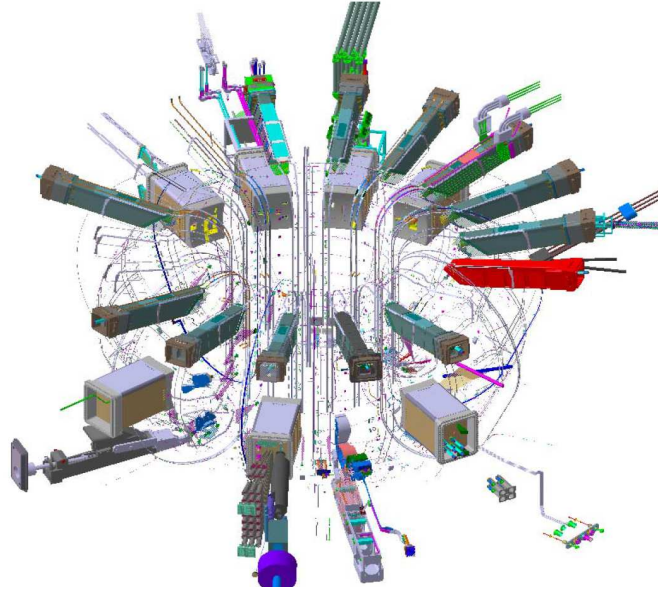


Figure 1.6: An overview of the diagnostic systems to be installed on ITER. Image is taken from [16].

of fast neutrons at the entrance of the diagnostic blocks is expected to be $\approx 10^{16} \text{m}^{-2} \text{s}^{-1}$ [17]. These harsh conditions make it impossible to use windows. In fact, silica-based windows experience a decrease of their transmittance due to radiation-induced absorption whereas materials as sapphire suffer from radiation-induced luminescence after high gamma radiation. Windows and optical fibres should, therefore, be recessed from the plasma, beyond the radiological shield. In fact, to avoid neutron leakage, the whole chamber will be surrounded by a shielding material. Obviously, windows cannot be placed directly behind a few metres of concrete. Therefore it was proposed for ITER to use a labyrinth of metallic mirrors embedded in the shielding material, to transmit the light from the plasma to the diagnostic systems [16]. This method will ensure a significant weakening of the radiation levels at the end of the labyrinth. These metallic mirrors called FMs will be the first and closest element of the plasma diagnostic system in ITER. The proposed layout of ITER CXRS and CPTS is shown in Figure 1.7.

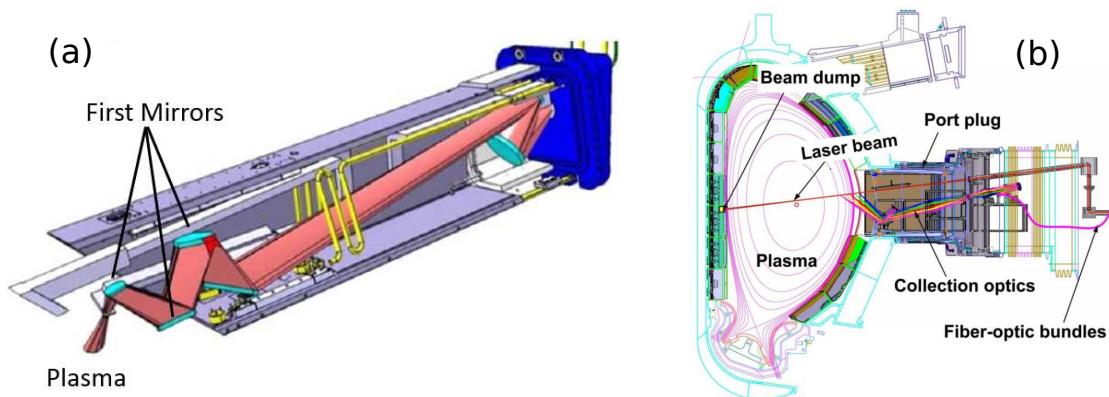


Figure 1.7: Optical layout for CXRS (a) and CPTS (b) diagnostics. In the second, collection optics stands for FMs.

1.3.2 First mirrors

Optical diagnostics will cover a wide wavelength range, from 5 nm to 100 μm and about 80 FMs will be installed in ITER, located all around the reactor (see Figure 1.8). Their size will vary from few cm^2 to large size mirrors (for example, $410 \times 210 \text{ mm}^2$ for the CPTS diagnostic).

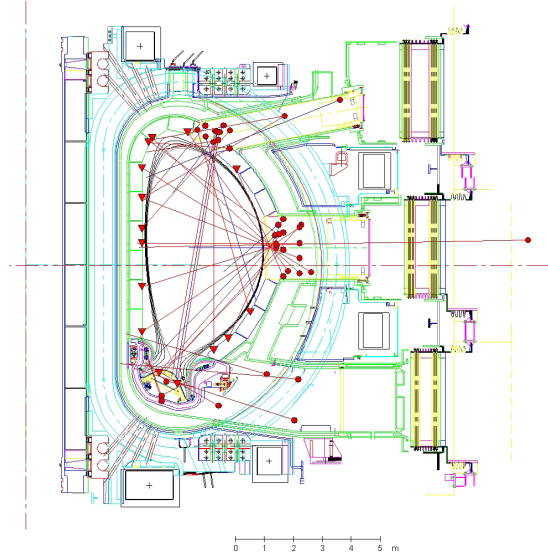


Figure 1.8: *Poloidal section of ITER with the location of the FMs (red dots) and their main lines of sight (red lines) [18].*

Being the closest element to the plasma, FMs will suffer from intense radiation, bombardment by CXNs and deposition of impurities coming from the eroded FW. Despite those conditions, they will have to maintain their optical properties over the full ITER operational time to ensure proper plasma diagnostic. For security diagnostic, severe degradation of the mirrors performance could lead to the failure of the diagnostic and imply a shut-down of the fusion reactor. Erosion and deposition are believed to be the two main phenomena that could affect the FMs optical properties.

1.3.3 Plasma Erosion

Plasma erosion of FMs is based on physical sputtering (removal of atoms from a surface due to an incoming ion or neutral with a certain energy) that is thoroughly described in section 2.5. As ions are confined by the magnetic field, the sputtering of FMs is mainly driven by neutrals such as CXNs with fluxes up to 2×10^{19} atoms/ $\text{m}^2 \cdot \text{s}$, average energies estimated to lie between 200 and 300 eV [19, 20] with maximum energies up to several keV [21] depending on the locations of FMs. In the case of polycrystalline materials composed of many grains with random faces orientation, each of the grains will be eroded with different rates. This causes an initially polished surface to evolve towards a stepped/rough structure. Such an increase of the mirror surface roughness causes strong reflectivity decrease (see equation 3.5) through increase of diffuse reflection (scattering). Experiments conducted in [21] report the loss of specular reflectivity for D bombardment as a function of the eroded thickness for W mirrors. As shown in Figure 1.9, polycrystalline materials behave extremely badly under erosion conditions for eroded thickness of 7 μm . To avoid such roughening effects, mirrors should have small grain sizes and preferably similar crystal orientation to be homogeneously sputtered. The two possibilities for FMs are thus single crystal mirrors and nanostructured films deposited on a suitable substrate. In Figure 1.9, single crystalline materials maintain good optical properties even for eroded thickness of 7 μm . Nanocrystalline mirrors exhibit similar properties and FMs mock-ups with a stainless steel (SS)

or TZM (Titanium-Zirconium-Molybdenum alloy) substrate and rhodium (Rh) or Mo coating have recently been achieved with a diameter of 109 mm [22]. Each crystalline structure exhibits advantages and drawbacks. Single crystals mirrors preserve their specular reflectivity even after the removal of microns of material, but the production of large size single crystals mirrors remains challenging. Nanocrystalline mirrors can be obtained by evaporation, magnetron sputtering or pulsed laser deposition. Large surface can be coated with highly reflective materials, but one open issue resides in the possible delamination of the nano-crystalline film under the harsh ITER conditions (high neutron and CXNs fluxes).

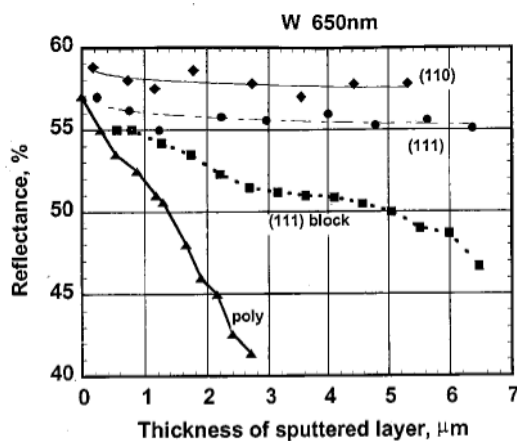


Figure 1.9: Reflectance of W mirrors (polycrystal, block monocrystal and single crystal) at $\lambda = 650$ nm depending on the eroded thickness [21]. Monoblock crystal is not a real single crystal but has a given crystal orientation for almost all grains.

The choice of the material for the FMs should fulfil following requirements: high optical reflectivity, chemical stability, no transmutation due to high neutron fluxes, high thermal conductivity for efficient cooling and a low sputtering yield (to avoid excessive sputtering). At first sight, copper (Cu), SS, W, Mo and Rh are ideal candidates. However, Cu and SS exhibit poor reflectivity below $\lambda = 500$ nm and Cu is sensitive to sputtering [19]. Compared to Mo and Rh, W has the lowest reflectivity and the fabrication of large single crystal mirrors is extremely challenging. The top candidates for ITER FMs are currently Mo and Rh as single or nanocrystalline form. Due to the high cost of Rh, its use as FM material is limited to the nanocrystalline form and as delamination is still an issue, single crystal Mo mirrors are mainly considered.

1.3.4 Deposition

In parallel to erosion, FMs will be subject to deposition. In fact, materials eroded from the FW through physical or chemical sputtering will end up somewhere else. The eroded material will mainly be re-deposited close to its original location, e.g. on the FW. Still, some of the impurities will enter the plasma and migrate to further locations. Before discussing the implications of re-deposition for ITER, a brief summary of results obtained experimentally in JET-ILW and other systems will be given subsequently.

In the past years, extensive tests were conducted in several tokamaks, trying to understand the nature of the deposits (chemical and morphology analysis) as well as their implication on optical performance of mirrors. Although experiments were conducted in many tokamaks, the most relevant results are the one obtained in tokamaks approaching ITER such as JET or the one obtained using Be and W with conditions mimicking ITER as for example in a linear plasma device. Before coming to those results, a brief statement can be made for other machines. Deposits containing FW materials were found to grow in JET-Carbon (JET-C), in the Axially Symmetric Divertor Experiment (ASDEX) Upgrade, in the Tokamak Experiment for Technology

Oriented Research (TEXTOR), Tore Supra ... [23–26] where mirrors exhibited modifications of their optical properties. Various morphologies were observed, from porous to compact films. For example, in JET-C, some mirrors experienced a catastrophic loss of reflectivity (up to 80–90 %). Additional campaigns were performed in JET-ILW, with the aim of mimicking ITER FW. The main results are presented in [27] and similarly to previous campaigns, mirrors experienced strong reflectivity losses, mainly driven by deposition. The presence of Be, carbon (C), D, nitrogen (N), oxygen (O) and W was measured on mirrors where Be was found to be the main constituent. Depending on the position of the mirrors in JET, the contaminant layer was either non-existent (net-erosion region) or up to 600 nm thick with respectively no impact and impact on the reflectivity. As shown in Figure 1.10, the reflectivity strongly decreased in some cases with losses unacceptable for ITER (50–85 %).

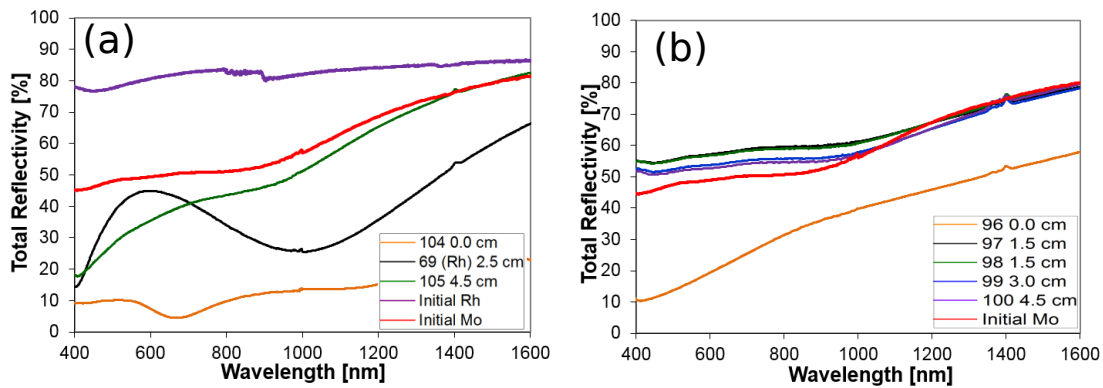


Figure 1.10: Total reflectivity of test mirrors exposed in (a) the inner divertor and (b) main chamber wall of JET-ILW. Images are taken from [27].

Chemical analysis revealed that O was present throughout the whole thickness of the film [27] and that the films were strongly oxidized (BeO measured by X-ray photoelectron spectroscopy (XPS), [28]). This will have some severe consequences for plasma-based cleaning techniques as discussed later.

As Be based reactor are not common, further tests were performed in a linear plasma device based in San Diego: PISCES-B. The aim of the tests was to deposit Be in conditions relevant for ITER and to investigate the nature of the deposits [29]. Be was thus deposited on mirrors after having been eroded from a Be target with a deuterium plasma. These deposits led to strong reflectivity decrease, even with low thicknesses of Be as displayed in Figure 1.11. Also, deposits were found to be porous in some cases.

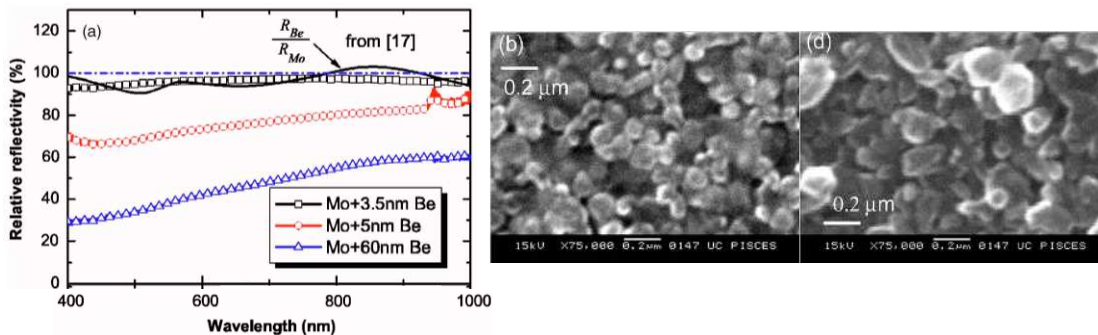


Figure 1.11: Relative reflectivity of Be deposits on Mo and scanning electron microscopy images of Be deposited on W (respectively 75 and 90 nm). Images are taken from [29].

Up to now, all tests performed in tokamaks or linear plasma devices have systematically

exhibited reflectivity losses for some mirrors depending on their locations. Generally speaking, a higher amount of deposition and thus stronger impact on the optical properties were observed in divertor regions but other locations were not spared by this phenomenon. Erosion and deposition are both affecting the mirrors reflectivity, but both processes are not complementary. Still, in ITER, it is believed that deposition will dominate most mirrors. Issues attributed to deposition therefore became a priority for ITER. Indeed, although the deposition in ITER cannot yet be known, simulations performed by Kotov [30, 31] showed that deposition of Be on FMs could be as high as $0.1 \text{ nm}\cdot\text{s}^{-1}$ depending on the location. Taking into account the simultaneous erosion and specific diagnostic geometry (see section 1.4.1), net deposition was calculated to be between 5×10^{-5} and $6 \times 10^{-3} \text{ nm}\cdot\text{s}^{-1}$, leading to 2.5 nm deposits per 400 s long pulse. Impurity deposition could, therefore, be a serious issue. According to the author, the results for deposition should be taken with great care due to large unknowns. Research on deposition mitigation techniques as well as on surface recovery is thus mandatory for ITER. The latter represents the scope of this Ph.D. thesis.

1.4 Mitigation and recovery techniques

1.4.1 Mitigation

As described above, high deposition rates are expected on ITER FMs and should be minimized. For that purpose, several mitigation techniques were investigated. Before entering into details, let us just recall that the diagnostic system optics are enclosed in a box. At the front of this box, there is a small opening (entrance pupil) directed towards the plasma allowing light to be collected. The mirrors form a labyrinth to extract the light towards detectors and are embedded in the bio-shielding forming a so-called diagnostic duct. Based on his simulations, Kotov proposed to recess the FMs as far as possible at the end of the diagnostic ducts (duct geometry: length L and diameter D) [32]. For large L/D ratios, the Be deposition can be strongly attenuated, with attenuation factor up to 5000 for $L/D = 30$. By adding fins to the duct (see Figure 1 [32]), the attenuation factor can almost be multiplied by 10. In addition to specific designs, active mitigation techniques might be employed such as gas puffing in front of the mirrors [33] and shutters (which will close in between measurements) [34]. Although those mitigations techniques will strongly reduce deposition, they do not guarantee a full suppression. Gas puffing is promising, but it is not yet decided if this technique will be employed in ITER while for shutters, they will only protect FMs when measurements are not required. Finally, regarding optical designs with long ducts and fins, recent experiments performed in TEXTOR to validate modeling predictions of Kotov exhibited contradictive trend [35]. One as thus to assume that deposition will occur on FMs and that deposits will form layers strongly impacting FMs optical performances.

1.4.2 Recovery

FM cleaning techniques capable of removing the contaminant layer should have the following characteristics:

1. Applicable in situ, without having to break the vacuum of the machine
2. Effective on all types of contaminant, from Be to W in metallic form to oxidized and potentially insulating films
3. Adaptable to ITER with relevant constraints (magnetic field, large size mirrors, low available space in diagnostic port plugs ...)
4. Harmless for the surface of FMs

Two techniques are worthy of interest: laser and plasma cleaning. The former one is based laser-matter interactions where a laser beam is focused on the FM surface, leading to contaminant ablation either by vaporization or due to thermo-mechanical forces. Initially, the pristine

mirrors are tested for damage thresholds (i.e. the laser fluence at which damage occurs) and the laser energy and wavelength are tuned to preserve the mirror's integrity in succeeding cleanings. Several experimental attempts were done on mirrors exposed in tokamaks or coated with ITER-relevant deposits and showed promising results [36, 37]. In most cases, the reflectivity of the mirror was improved towards initial values but for some deposits, either highly reflective or highly transparent, the contaminants were not removed. This poses a serious threat regarding the universality of the method. Moreover, the question of integrating such in situ laser cleaning is not yet satisfactorily addressed. For those reasons, the second method based on sputtering via plasma exposure is currently considered as the most promising technique and was investigated by more than seven groups worldwide including the University of Basel. At the moment, five groups are still involved in the FM plasma cleaning field.

Two different configurations can be used to achieve plasma cleaning. The first one is based on an external plasma source, located in the vicinity of the mirror. Ions can either be accelerated within the source or by applying a negative bias on the sample. For example, Litnovsky *et al.* generated an external He plasma through Electron Cyclotron Resonance and applied a negative bias (-100 V) on \varnothing 18 mm Mo mirrors coated with 100 nm Al [35]. They obtained a complete removal of the Al deposits with recovery of the optical properties of the mirror. Another group from the Frumkin Institute of Physical Chemistry and Electrochemistry based in Moscow led by I. Arkhipov employed a DC glow discharge with external negative DC biasing of the samples. Etching experiments were conducted on \varnothing 18 mm samples without magnetic field. The first study was conducted on hydrocarbon films (initially the ITER divertor was supposed to contain carbon) with -50 V bias and showed a removal of those contaminants with stability of the reflectivity between 1000 and 1100 nm [38]. A further study was performed on W, Al and Be deposits in a D_2/O_2 discharge [39]. They found that the sputtering yields were maximized by adding between 2 and 4 mol.% oxygen to the deuterium at a bias of -100 V and attribute this phenomenon to the formation of weakly bound surface oxides and hydroxides. In this case, a partial oxidation of the contaminant was not an issue due to the low amount of oxygen added in the process and the oxide formation is thus limited by sputtering. However, for larger oxygen concentration, slower etching processes or already oxidized films, insulating properties of the films might develop (Al_2O_3 and BeO are insulators) as in the well-known target poisoning phenomenon [40]. In that case, the surface of the film can charge up and inhibit sputtering. The major disadvantages of such cleaning techniques reside in the difficulties of implementing an external plasma source close to each FM to be cleaned as well as on the impossibility to sputter the contaminants in the case of insulating deposits.

The second option for plasma sputtering uses the mirror itself as a "plasma source", by applying DC, pulsed DC or AC directly on it. The surrounding gas is ionized and a self-sustaining discharge is obtained. Research led by the Kurchatov Institute focused on the application of Penning discharge for cleaning FMs where DC or pulsed DC is applied on the FM, serving as a cathode and where the second electrode can be the second mirror [41]. The discharge cell is operated in the presence of magnetic field up to 0.5 T. The system was proven to efficiently remove 200 nm Al deposits from a \varnothing 23 mm Mo mirror placed on a 45×45 mm² electrode at discharge voltages up to 750 V. When DC was used, micro-arcs were observed in the discharge (due to surface charging of the insulating deposits) and dielectric breakdown led to severe degradation of the mirrors. This issue could be solved by employing pulsed DC.

Instead of DC or pulsed DC, it would also be possible to use RF with frequencies varying between 13.56 and 81.4 MHz in CCP mode. This technique is commonly named as RF plasma cleaning and was employed in the majority of this thesis as well as in three other laboratories. The latest results of the group from Ioffe Institute in St. Petersburg exhibited promising results [42]. Using RF at 81.4 MHz, they were able to remove a 25 nm thick Al film from a \varnothing 80 mm mirror with either Ne or D_2 and ion energies equal to 220 and 300 eV, respectively. In addition, they performed a first etching homogeneity test on \varnothing 80 mm sample coated with gold in the presence of a B-field perpendicular to the surface with $B = 0.05$ T. The etching was found to be homogeneous with enhanced erosion in the centre of the sample attributed to re-deposition from the opposite electrode. A group from the Institute of Plasma Physics in Hefei, China, added

magnets behind the samples to improve the etching rate [43,44]. They obtained satisfactory results with removal of carbon contaminants but the magnetic field configuration they used poses a serious question regarding the homogeneity of the etching process. The last group working on RF plasma sputtering is part of the Netherlands Organisation for Applied Scientific Research and is performing FM cleaning R&D on behalf of the Upper Wide Angle Viewing System (UWAVS) diagnostic for ITER. They designed and constructed a mirror test cleaning setup to quantify optimal cleaning discharge parameters in an ITER-like environment [45]. First results are expected in the near future.

Theoretical background

THIS chapter provides a brief summary of low-temperature plasma (LTP) physics and its application for in situ cleaning for ITER. Theoretical background on plasmas will be given in section 2.1. The main method used to generate plasma in this work, namely capacitively coupled RF plasma will be discussed in section 2.2 with specific attention given to asymmetric RF discharges. The third section (2.3) will be devoted to a specific case of RF discharges where the driven electrode is DC-grounded. Focus will be given on the physical concept of such discharges as well as on the way to obtain them. Because some cleaning experiments will take place in the presence of a magnetic field, a brief insight in magnetized plasmas will be given in section 2.4. Finally, as the idea behind in situ cleaning for ITER is based on etching of the surface of FMs that was used throughout this Ph.D. thesis, physical sputtering will be introduced in section 2.5.

2.1 Low-temperature plasma

Plasma is considered to be the 4th state of matter and is the most abundant one in the universe, similar to a gas containing ions, electrons and neutral species. Examples of naturally occurring plasmas are stars, interstellar medium, lightning, polar lights ... One important parameter defining plasma is the ionization degree that can vary from 100 % for fully ionized gases, like the fusion plasma in ITER, to very low values for partially ionized gases as the ones used throughout this work. Another important characteristic of plasma is its quasi-neutrality. Assuming that ions are singly and positively charged with n_i and n_e the ion, respectively electron density, the plasma should satisfy:

$$n_i \approx n_e = n_0$$

where n_0 is the plasma density. All the plasmas observed in the universe or man-made cover an extremely wide range of plasma density and electronic temperature (T_e) as shown in Figure 1.7 of [46] and can be divided in high and low-temperature plasmas. A further subdivision can be made between plasmas in thermal equilibrium ($T_e = T_i$) and non-thermal equilibrium, where T_i stands for ionic temperature. In the latest category, electrons are at much higher temperature than heavy particles (ions, neutrals) that are usually at room temperature. Typically, LTP have $T_e = 1-3$ eV $\gg T_i$ and $n_0 \approx 10^{16}$ m⁻³. The fundamental length of a plasma is the Debye length (λ_D) defined as:

$$\lambda_D = \sqrt{\frac{\epsilon_0 T_e}{e^2 n_0}} \quad (2.1)$$

where ϵ_0 is the vacuum permittivity and e is the elementary charge. An ionized gas is a plasma if it fulfils $n_0 \lambda_D^3 \gg 1$.

Igniting and sustaining a plasma discharge can be done by applying an electric field to a neutral gas. Initially, the neutral gas present in the vacuum chamber contains very few charged particles. When an electric field (DC or AC) is applied, the free charged particles are accelerated and collide with gas molecules leading to exchange of energy and/or creation of new charged particles (ions and electrons). Those new particles are in turn accelerated and subject to collisions, resulting in an avalanche multiplication of charged particles. Simultaneously, charged particles are lost either through recombination or diffusion to the walls leading to equilibrium (steady-state). Due to the non-negligible number of charge carrier present in it, plasmas are electrically conductive and have a strong response to external electromagnetic fields.

Due to the higher mobility and energy of electrons, they will more rapidly leave the plasma than ions and hence, to conserve quasi-neutrality within the plasma bulk, a region adjacent to the walls (or electrodes) will charge up positively: the sheath, where the quasi-neutrality condition will fail. This region is characterized by a strong electric field accelerating ions towards the walls while, at the same time, repelling electrons into the plasma. Thus ions will gain energy during their travel through the sheath and will bombard the surface.

2.2 Capacitively coupled RF plasma

CCP is the most commonly used method to sustain discharge in industry and laboratory. One of the main interest of this technique is that it can be applied both on conducting and insulating electrodes as it is sustained by RF. In contrary, DC glow discharges can only be used on conducting samples as insulating surfaces would charge up. The discharge is generally run at 13.56 MHz, a standard industrial RF frequency. A schematic of a discharge chamber is shown in Figure 2.1 and is composed of a vacuum chamber, a driven/powerd and grounded electrode with area A_d and A_g respectively, and an RF source. The distance between both electrodes is called electrode gap and is denoted d in most of the literature. An impedance matching network can additionally be inserted between the RF power source and the driven electrode to adjust the impedance of the load (plasma + electrode + coaxial cable) to the 50Ω of the RF generator. By doing so, the reflected RF power is minimized, thus enabling a maximum power transfer to the plasma. If the driven and grounded electrodes area are equal, the system is labelled symmetric CCP. Usually, the walls of the chamber are connected to the grounded electrode. Hence the grounded area is much larger than the driven electrode area and the discharge is run in a strongly asymmetric configuration. In this work, asymmetric discharge systematically describes configurations with large grounded areas and small driven areas.

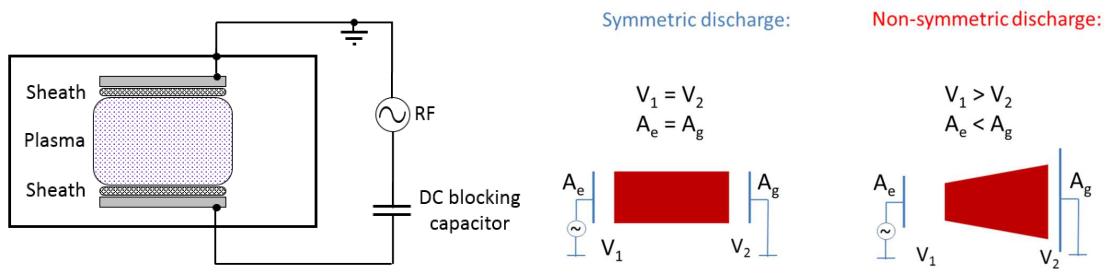


Figure 2.1: Schematic of a simplified capacitively coupled plasma with plane parallel electrodes. Illustration of symmetric and non-symmetric discharge and its influence on both sheaths voltage drop.

Self-bias

Because of the blocking capacitor, no DC can flow to both electrodes and, due to the greater mobility of electrons over ions, the plasma potential V_p must be positive with respect to either electrode as otherwise, more electrons than ions will be collected by the electrodes. In the

case of symmetric CCP, both electrodes have the same area and hence sheaths with similar capacitance. This results in an equal voltage drop across both sheaths. For an asymmetric discharge, the capacitance of the driven electrode sheath is much smaller leading to a larger voltage drop across this sheath. Due to the blocking capacitor, a negative DC self-bias voltage (V_{bias}) builds up on the driven electrode, accelerating ions to the electrode while repulsing electrons so that total charge flow per cycle sums to zero [47,48]. In 1999 Kawamura *et al.* [49] gave a theoretical formula linking the self-bias, the RF voltage V_0 and the area of the grounded and driven electrodes (respectively A_g and A_d):

$$V_{bias} = V_0 \sin\left(\frac{\pi}{2} \times \frac{A_g - A_d}{A_g + A_d}\right) \quad (2.2)$$

The value of the self-bias is extremely important for the following work as it is an important “control knob” for the ion energy. When they enter the driven electrode sheath, ions acquire an average energy (in eV) equivalent to the sum of DC self-bias and the plasma potential (V_p): $V_{bias} + V_p$.

RF breakdown

To ignite the plasma, a gas breakdown is necessary. This occurs when the number of charged particles created by collisions in the plasma or through secondary electron emission from the electrodes exceeds the losses due to recombination or diffusion to the walls. The condition to ignite the gas are among other parameters dependent on the pressure p , the electrode gap d and the applied voltage (here RF). Obviously, the electric field should be large enough for electrons to gain sufficient energy to cause further ionization. The pressure should also be high enough so that the mean free path λ_{MFP} is much smaller than d and electrons can collide with other atoms before reaching the electrode. If the pressure is too high, there are too many collisions randomizing the direction of electrons, and in turn, they will give up their energy in a series of non-ionising collisions. Frederic Paschen empirically describes this phenomenon through the Paschen’s law:

$$V_{Brk} = \frac{Bpd}{\ln(Apd) - \ln(\ln(1 + \gamma_{se}^{-1}))} \quad (2.3)$$

where V_{Brk} is the DC breakdown voltage in volts, p is in Pascal, d in meters, γ_{se} is the secondary electron coefficient. A and B are constants determined experimentally. RF breakdown works in a similar manner except for surface processes (secondary electron emission) which are not so important at higher frequencies due to confinement of electrons by field oscillations. Hence RF Paschen curves are not as dependent on the electrode material than for DC voltages [50,51].

Heating mechanisms

To sustain a discharge, production of new ions is necessary and is mainly done through electron impact ionization. This requires electrons with sufficient energy that needs to be heated. Three distinct modes of heating were determined for CCP:

1. **Sheath heating** This first mode, also termed stochastic heating, is dominant in low-pressure discharges (0.1–1 Pa) and is based on sheath oscillations. A simple analogy can be made with a tennis player hitting a ball. Electrons gain energy with the sheath while it is expanding and lose energy if it is retracting. On average there is an energy gain [52].
2. **Ohmic heating** At higher pressures, λ_{MFP} is smaller than the electrode gap d leading to ionization within the plasma bulk. Bulk low energy electrons will be heated by the RF field and further contribute to ionization. When this mechanism is dominant, the discharge is said to be in α mode.
3. **Secondary electron heating** When ions accelerated in the sheath bombard the surface of the driven electrode, secondary electrons (SE) can be released and accelerated by the

oscillating sheath. If the discharge pressure is high enough, significant ionization will take place in the plasma-sheath boundary. Hence more ions are attracted to the surface and more SE are released, leading to an electron avalanche. Relatively high pressures are requested for this mode to be dominant (tens to hundreds of Pascal) as otherwise, SE thermalize in the plasma bulk or escape the discharge without a collision. This heating mechanism is also called γ mode heating.

The main heating mode present in the discharges used throughout this Ph.D. thesis has strong implications on the ion density and electron temperature and will be discussed in section 4.2.1.

2.3 Driven grounded electrodes in CCP

In addition to normal capacitively coupled plasma cleaning with DC blocking capacitor, experiments were conducted by short-circuiting/grounding the DC component of the driven electrode (see section 4.2.5 and 6.3). This specific configuration was investigated on request of ITER Diagnostic team and is currently denoted as Notch filter technique in ITER Organization. It presents an easier integration scheme using a stop band filter (see Figure 2.2) as will be discussed later. First, let us briefly describe such discharges analytically.

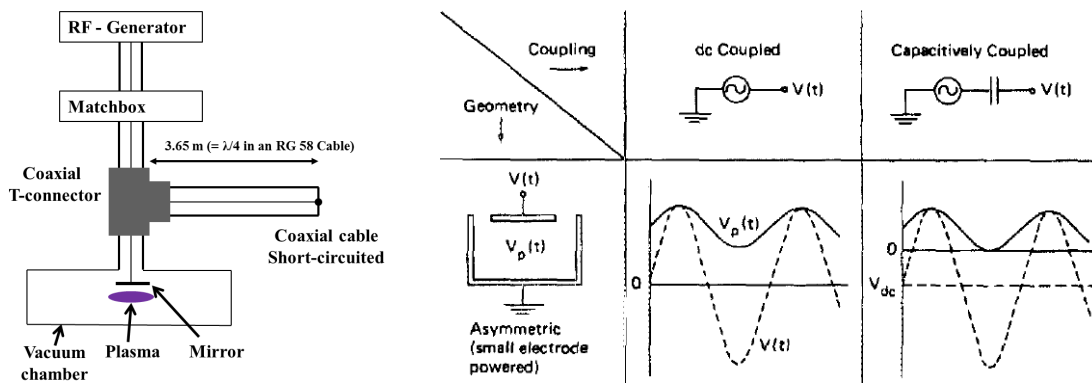


Figure 2.2: Schematic of driven grounded electrode configuration where the DC short-circuit is done with a stop band filter ($\lambda_{cable}/4$ grounded cable). λ_{cable} stands for the wavelength in the cable (for RG 58 cable, the propagation speed is $0.66 \times c$). Illustration of the plasma potential $V_p(t)$ (solid curves) and excitation voltage $V(t)$ (V_0 in this work, dashed curves) for DC-coupled and capacitively coupled driven electrodes. Right image is taken from [47].

As stated above, an asymmetric CCP with blocking capacitor will see a negative self-bias develop onto the driven electrode. If this DC bias is short-circuited, both electrodes will be at ground potential. As the electrical circuit is now closed, a direct current is allowed to flow through the grounded electrodes and the current to the driven electrode (I_d) must be equal to the one flowing to the grounded wall (I_g). As will be shown later, this has strong implications on the plasma potential that is usually around 30 V in the normal CCP case and that increases up to several hundreds of volts for the driven grounded electrode geometry as observed experimentally by [47, 53]. The first attempt to explain this phenomenon was done by K. Köhler *et al.* in 1985 [47] and is based on sheath analysis. Although we always consider the plasma potential to be constant in the rest of the work (and it is the case for ions), the succeeding model is mainly based on electron motion and one should consider the oscillating plasma potential:

$$V_p(t) = \bar{V}_p + \Delta V_p \sin(\omega t) \quad (2.4)$$

where ω is the excitation frequency and by assuming that sheaths are capacitive, ΔV_p is

determined by capacitive voltage division:

$$\Delta V_p = V_0 \left(\frac{C_d}{C_d + C_g} \right) \quad (2.5)$$

where C_d and C_g are the sheath capacitances of the driven and grounded (wall) electrodes, and V_0 is the RF voltage. Due to high electron mobility, the instantaneous plasma potential cannot be less than the instantaneous potential of any surface in contact with plasma. The following equations are written for the capacitive case where the DC bias is grounded (e.g. equal to zero) or supplied by an external DC source:

$$\begin{aligned} \bar{V}_p + \Delta V_p &\geq V_0 + V_{bias} \\ \bar{V}_p - \Delta V_p &\geq 0 \end{aligned} \quad (2.6)$$

For the case where a current can actually flow through the driven electrode, one of those inequalities becomes an equality depending on $V_0 + V_{bias}$. In our strongly asymmetric configuration, we have $V_{bias} + V_0 \geq 2\Delta V_p$ and the first inequality determines \bar{V}_p :

$$\bar{V}_p = V_{bias} + V_0 \left(\frac{C_g}{C_d + C_g} \right) \quad (2.7)$$

Finally, the driven grounded case has a bias of zero volts. As both sheaths have a similar voltage drop, the capacitances difference is mainly driven by the change in area. Hence, if the wall area is much larger than the driven area, the mean plasma potential is extremely dependent on the applied RF voltage. Figure 2.2 illustrates both configurations used in this work.

In addition to this model based on capacitive sheaths, A. Aanesland developed an analytical model of grounded discharges by looking at the direct currents flowing in the system [54]. It is assumed that electrons can only reach the grounded electrode when the instantaneous applied RF voltage $V_0(t)$ is larger than the time-averaged plasma potential, e.g. when $V_0 \cos(\omega t) - \bar{V}_p > 0$. Electrons can reach the system during a fraction of the RF period (ϕ/π) where ϕ is defined as:

$$\phi = \cos^{-1} \left(\frac{\bar{V}_p}{V_0} \right) \quad (2.8)$$

If the average plasma potential is large and hence close to the RF voltage electrons can only be collected during a short time. For a low plasma potential, much smaller than the RF voltage, electrons will be collected during half of the RF period. As a collection time is now defined for electrons and assuming that ions are collected on the driven electrode for the entire RF cycle, the electron, ion and total current can be defined on this electrode. Additionally, by assuming that at the large grounded electrode, ΔV_p is small compared to \bar{V}_p , the total current at the grounded electrode can be expressed. Finally, as $I_d = I_g$, one can obtain:

$$\cos^{-1} \left(\frac{\bar{V}_p}{V_0} \right) = \pi \left[0.61 \left(\frac{2\pi m_e}{m_i} \right)^{1/2} - \exp \left(-\frac{e\bar{V}_p}{kT_e} \right) \right] \frac{A_g}{A_d} \quad (2.9)$$

where m_e and m_i are the electron and ion mass respectively. When $A_g/A_d > 80$, \bar{V}_p approaches an asymptote for all applied RF voltages (equal to 15.5 V for a 3 eV Ar plasma). Hence when the driven electrode is too small, it has a very limited effect on the plasma potential. If $1 < A_g/A_d < 80$, which was the case throughout the thesis, the driven electrode strongly influences the plasma potential that can increase to the order of the applied RF voltage. An extremely important result found experimentally is that the plasma potential in the grounded case can be equal to the sum of the plasma potential and self-bias in the capacitive case [55]. Measurements performed in section 4.2.5 and 6.3 showed that the plasma potential significantly increases towards the sum of self-bias and plasma potential in the normal case, but never to the full extent. Typically, a few additional watts were needed. This discrepancy is due to additional

power losses introduced by the additional T-connector and $\lambda_{cable}/4$ long cable needed for this specific configuration. Due to the high positive plasma potential, the driven grounded electrode can still be sputtered by ions accelerated in the sheath and ion energies equivalent to the normal capacitively coupled case can be attained (by slightly increasing the RF power). However, in the driven grounded electrode case, the walls of the chambers will also be sputtered by energetic ions while in the normal case, these ions would only have a few tens of eV ($V_p = 20\text{--}30$ V).

On an electrical point of view, there are several ways to ground the DC while having a normal circuit for the RF. One solution would consist in a grounded low-pass filter using, for example, a coil. Another possibility would be to use a stop band filter. For that purpose, an RF transmission line with an electrical length of $\lambda_{cable}/4$ and short-circuited at its end is added to the system (via T-connector). This specific section has an infinite impedance at the feed point and the RF does not “see” the DC short-circuit. Plasma cleaning in the driven grounded electrode case was investigated in this Ph.D. thesis as it facilitates implementation in ITER (see section 6.3).

2.4 Plasma in magnetic field

2.4.1 Single particle motion

In the presence of a static and uniform external magnetic field, the motion of charged particles can be solved using the Newton equation with the Lorentz force:

$$m \frac{d\vec{v}}{dt} = q(\vec{v} \times \vec{B}) \quad (2.10)$$

with m and q the mass and charge of the particle, \vec{v} the velocity of the particle and \vec{B} the magnetic field. The velocity can be decomposed into two components, respectively parallel and perpendicular to the magnetic field as following: $\vec{v} = \vec{v}_{\parallel} + \vec{v}_{\perp}$. Projecting the Newton equation along those two directions implies that \vec{v}_{\parallel} and \vec{v}_{\perp} are constant and in the perpendicular plan, the particle is driven by a uniform circular motion where the radius of the circular motion, also called Larmor or cyclotron radius (ρ_i) is given by:

$$\rho_i = \frac{mv_{\perp}}{|q|B} \quad (2.11)$$

The combined parallel and perpendicular motion of a charged particle therefore results in a helical trajectory. In other words, ions or electrons gyrate around the magnetic field and drift parallel to the field according to the initial parallel velocity. Assuming electrons have a kinetic energy of 3 eV, ρ_i will be equal to 1.7×10^{-6} m. Non-magnetized low-pressure plasmas are usually non-thermal and characterized by a high electron temperature ($T_e \gg T_i$). Still, in magnetically confined discharges, $T_e \approx T_i$ can hold due to the increased loss times to the walls (electrons have sufficient time to transfer their energy to ions). Hence, for ions with similar energy, the Larmor radius would be equal to 1×10^{-4} m.

If a force \vec{F} is further added to the system, the Newton equation becomes:

$$m \frac{d\vec{v}}{dt} = q(\vec{v} \times \vec{B}) + \vec{F} \quad (2.12)$$

For the parallel motion, this leads to an acceleration $m \frac{dv_{\parallel}}{dt} = F_{\parallel}$ while the perpendicular motion is the sum of the cyclotron motion plus a drift velocity $\vec{v}_{\vec{F}}$ defined as:

$$\vec{v}_{\vec{F}} = \frac{\vec{F} \times \vec{B}}{qB^2} \quad (2.13)$$

In typical fusion plasma, drifts can occur due to electric fields or inhomogeneous magnetic fields as well as from the B-field curvature. For the present study, the sole force that was

considered in the particle motion was the E-field originating from the self-bias. In fact, within the magnet, B-field lines are assumed to be parallel and the field gradient is in the same direction as the field orientation, e.g. $\nabla \mathbf{B} \times \mathbf{B} = 0$. Coming back to the electric field and assuming that the force $\vec{F} = q\vec{E}$, the so-called $\mathbf{E} \times \mathbf{B}$ drift is given by:

$$\vec{v}_E = \frac{\vec{E} \times \vec{B}}{B^2} \quad (2.14)$$

This drift is independent of the charge as well as the mass of the particles and provides a motion of the plasma as a whole.

2.4.2 Magnetized plasma

When the magnetic field is perpendicular to the electrode, e.g. parallel to the E field, the guiding center of the particles is not modified when they enter the sheath and thus, the impact angle is normal to the surface. When the magnetic field is oblique to the surface (in our experiments 70 to 85° to the normal), a magnetized pre-sheath (MPS), also called Chodura sheath, develops [13,56]. The region close to the electrode is therefore comprised of three regions as shown in Figure 2.3:

1. The typical Debye sheath where $n_i > n_e$ and a few λ_D thick.
2. The quasineutral magnetic pre-sheath a few ρ_i thick.
3. The usual plasma pre-sheath which is the plasma itself.

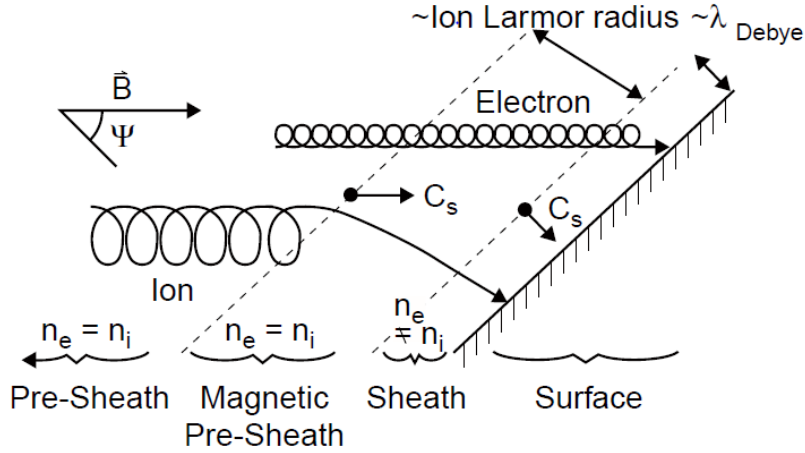


Figure 2.3: Near-surface of the electrode in the presence of an oblique magnetic field. Image is taken from [13].

Within the plasma, the charged particles gyrate and follow the magnetic field lines. In the Debye sheath, the ion gyro-motion is larger than the Debye sheath and this region is therefore dominated by the E-field, as if the B-field was non-existent. This implies that properties established without B-field are still valid like the Bohm criterion, and that ion must enter the sheath at sound speed C_s . When the ions are traversing the magnetic pre-sheath, the motion is turned from parallel to the B-field to perpendicular to the surface direction. Additional studies showed that the angle of ions when hitting the surface was indeed smaller than the angle of B-field to the normal but not equal to zero and with unchanged ion energy [57,58].

As discussed before, ion Larmor radius assuming same energy as for electrons was found to be 1×10^{-4} m. In literature, this value is also defined as the Larmor radius at sonic speed for cold ions ($T_i = 0$). As will be shown later, erosion rates were found to be almost factor 100

higher in the presence of 3.5 T B-field and, although no measurements were actually performed, one could assume to have electron densities hundred times higher than without B-field, hence electron densities around 10^{17} m^{-3} . Thus the assumptions above give a Debye length around $4.1 \times 10^{-5} \text{ m}$. A magnetization parameter ζ was defined in [59] as the ratio between ρ_i and λ_D . It was found that in the case where $\zeta > 1$ (in our case $\zeta \approx 2.5$), the MPS does exist. One can therefore assume that the ion energy is unchanged by the B-field even at oblique magnetized discharges and defined by the sheath voltage drop, and that the ions reach the surface at angles smaller than the B-field angle to the normal of the sample.

2.5 Sputtering

As stated before, electrons and ions are created in plasma, and their interaction with the surface can lead to different phenomena like heating, sputtering, implantation ... For FM in situ cleaning, sputtering is the main process involved where one has to distinguish physical and chemical sputtering. The latter involves chemical reactions at the surface, easing the removal of surface atoms. This mechanism was not studied in this thesis and will be developed more in details in the guidebook 7.2. Physical sputtering is the erosion of solid surfaces due to energetic particles bombardment. An incoming particle transfers its energy through collisions to the target atoms which can generate other recoils distributing the initial energy via a collision cascade. A surface atom can be removed from the surface, e.g. sputtered, if the energy transferred to it is directed towards the surface and is larger than the surface binding energy U_s . The schematic of such a collision cascade is displayed in Figure 2.4.

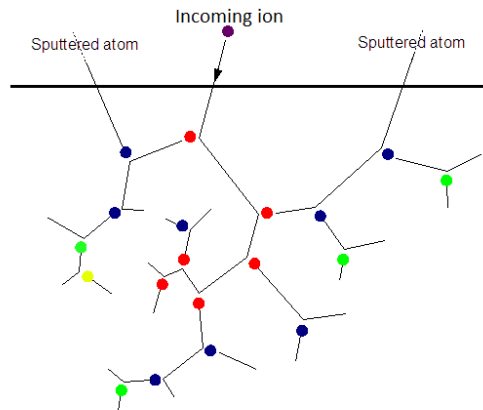


Figure 2.4: *Illustration of sputtering with a linear cascade regime.*

Three main collisions regimes were identified for sputtering:

1. **Single knock-on** This regime is observed when the primary recoil atoms have enough energy to be sputtered but not sufficiently to generate further recoils and is characterized by light incident particles or low energy heavy particles.
2. **Linear cascade** When medium or heavy particles with few hundreds eVs energy are bombarding the target, primary recoil atoms can generate further recoils. This regime is the most studied.
3. **Spike regime** The last regime is characteristic of heavy particles with large collision cross-section and is defined by a large recoil density.

In this work, sputtering was mainly driven by single knock-on and linear cascade regime, depending on the gas type and energy while the incoming particles responsible for sputtering are considered to be ions.

When ions hit the target, atoms are removed and the surface is eroded. A way to quantify the sputtering is to look at the sputtering yield (Y) defined as the number of atoms ejected from the solid per incident ion. The sputtering yield depends on various parameters such as ion energy, binding energy, ion and target atomic mass, impact angle ... Yamamura *et al.* [60] proposed an energy dependence sputtering yield formulae of monoatomic solids for normal incidence of ions:

$$Y(E) = 0.042 \frac{Q(Z_2)\alpha^*(M_2/M_1)}{U_s} \frac{S_n(E)}{1 + \Gamma k \epsilon^{0.3}} \left[1 - \sqrt{\frac{E_{th}}{E}} \right]^s \quad (2.15)$$

where E is projectile energy and M_1 , M_2 are the masses of a projectile and a target atom in a.m.u., respectively, and the numerical factor in units of \AA^{-2} . The factor Γ is defined as:

$$\Gamma = \frac{W(Z_2)}{1 + (M_1/7)^3}$$

The dimensionless parameters $W(Z_2)$, $Q(Z_2)$, α^* and s are best-fit values and are tabulated in [60]. S_n is the nuclear stopping cross section, k is the Lindhard electronic stopping coefficient and ϵ is the reduced LSS energy. Finally, E_{th} is the sputtering threshold energy. When the incoming ion energy is below this threshold, the target atoms are not sputtered. The Yamamura formulae was also successfully applied to multicomponent targets and is still widely used in the plasma community to calculate sputtering yields. Several trends regarding the evolution of the sputtering yield were observed experimentally, confirmed theoretically and are illustrated in Figure 2.5.

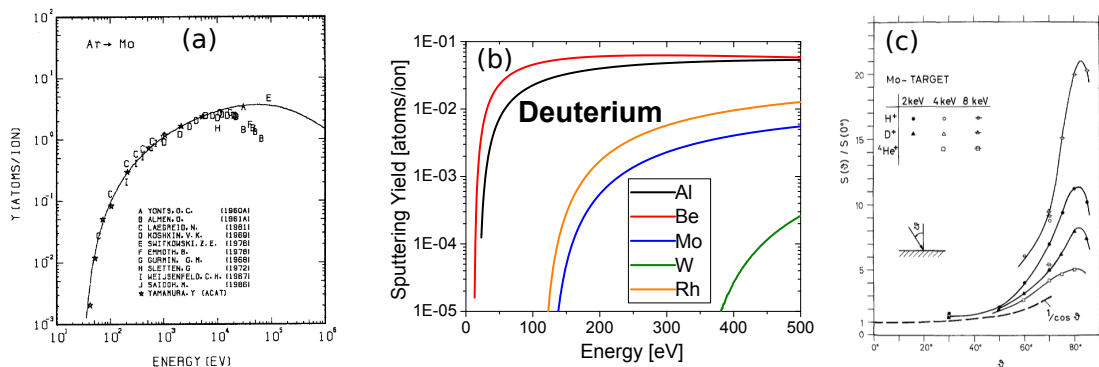


Figure 2.5: Sputtering yield as a function of (a) argon (Ar) energy on Mo , (b) D energy on several ITER materials [61] and (c) normalized sputtering yield as a function of angle of incidence for H , D and He ions on Mo target. Figures are taken from [60] (a) and [62] (c).

- The sputtering yield increases as the mass of the sputtered species increases. Furthermore, if the mass of the ions and the atoms from the solid are similar, this will also increase the sputtering yield.
- When the energy of the incoming ions increases, the sputtering yield increases. When the beam energy is higher than 100 keV, the sputtering yield decreases as ions penetrate too deep into the sample.
- When the incidence angle (measured from the surface normal) increases, the sputtering yield increases up to $\theta \approx 70-80^\circ$. For very steep angles, the sputtering yield decreases again as ions are mainly reflected by the surface. In this work, the ions are considered to bombard the surface at normal angle of incidence ($\theta = 0^\circ$), except for sputtering in the presence of oblique magnetic field (see section 6.2).

Chapter 2. Theoretical background

- The temperature of the target can also affect the sputtering process. In fact, when the temperature gets higher, the surface binding energies typically decreases and thus, higher sputtering yield values are obtained.
- The contaminants which will be deposited on the surface of FMs in ITER could form a rough surface. The sputtering yield of surfaces with high roughnesses is lower than for smooth surfaces.
- The sputtering yield of a given material depends on its crystallographic structure and can vary by a factor of 2 for individual grains with different crystallographic orientations. This is of particular importance for polycrystalline materials.

In ITER the deposits will be mainly composed of Be and W. In our laboratory these deposits were mimicked by using Al and W. Indeed, Be dust is extremely toxic [63] and Al can be used as a good proxy [64]. Since tokamaks contain residual oxygen, eroded material from the FW redeposited on the FMs could be partially or fully oxidized. Sputtering yield values at 200 eV with several gases (H_2 , D_2 , He, Ne and Ar) are summarized in Table 2.1 for the aforementioned elements where Mo and Rh were added as they are the prime candidate for FMs. For molecular ions, this energy has to be divided by the mass ratio between a constituting atom and the molecule to obtain the deposition energy per atom. Assuming that the sputtering yield at a given deposition energy is the same for atomic and molecular ions, the yield for D_2^+ at 200 eV is equal to the yield of D^+ at 100 eV multiplied by 2 (D_2 contains two D atoms) [65,66]. Data of chemical sputtering of Be by deuterium [67] were added in Table 2.1 for 30 eV energies but will not be discussed before section 7.2.

Table 2.1: *Sputtering yield of different materials as a function of gas used for plasma cleaning at 200 eV. The sputtering yields of BeD by D^+ , D_2^+ and D_3^+ are given for an energy of 30 eV. Data are extracted from [60, 67, 68].*

Sputtering yield (10^{-3} at./ions)	Mo	Rh	Be	BeO	BeD	Al	Al ₂ O ₃	W
H^+	0.01	0.1	25	12	-	14	5	0
H_2^+	0	0	40	6	-	14	1	0
D^+	1	4	50	30	35	40	20	0
D_2^+	0.02	0.2	80	26	20	44	1.5	0
D_3^+	0	0	80	18	15	39	0	0
He^+	10	26	100	40	-	100	8	1
Ne^+	20	400	400	-	-	500	-	80
Ar^+	300	600	200	-	-	500	40	210

An important input for plasma cleaning is the appropriate choice of gas and acceleration energy based on sputtering yields. In ITER the deposits must be removed as fast as possible (with ion energy greater than the sputtering threshold, see Table 2.2) while on the other hand, the FMs material should withstand the erosion. According to Table 2.1, He seems to be the best option to remove Be or BeO while having a small impact on Mo. For laboratory experiments with Al, Ne appears to be the best choice to erode Al but has a low sputtering yield on W. For subsequent experiments, Ar was chosen over Ne due to its high sputtering yield on both Al and W.

Table 2.2: *Damage threshold (in eV) of different materials for various gases [60].*

Material	D	He	Ne	Ar
Mo	100	70	35	35
Rh	100	60	27	29
W	250	150	55	55
Al	22	16	21	29
Be	14	15	30	47

Experimental

THIS chapter presents the experimental facilities (3.1) as well as the main characterization methods (3.2) used to pursue the specific objectives of the thesis. Two steps were mandatory to reach those objectives: (i) production of tailored films by physical vapor deposition (PVD) either to obtain reflective metallic coatings or contaminants mimicking ITER deposits and (ii) physical sputtering of contaminants using ions, and were performed in several vacuum chambers. Those points are respectively labelled as process (I) and (II) in the succeeding sections. A brief introduction to thin films production, especially with magnetron sputtering, will be given in section 3.4.

3.1 Plasma exposure facilities

Several vacuum systems were developed and used throughout the Ph.D. thesis depending on the needs and constraints of the experimental campaigns (Be contamination, presence of high magnetic field, large size electrodes ...). With ongoing experiments, specific points were improved such as RF electrical feedthrough, sample holder ...

3.1.1 ESCA-1 facility

The main facility used throughout the Ph.D thesis consists of 4 ultra-high vacuum (UHV) chambers connected together and pumped independently with conventional pumping systems. A loadlock chamber is used to introduced the samples in the facility while the transfer chamber is connecting the “sputter chamber” to the XPS chamber and allows in situ transfer of samples from one chamber to another. The complete system is shown in Figure 3.1. The prime chamber of the system is the experimental chamber with a base pressure of 2×10^{-5} Pa and denoted as sputter chamber. In this chamber, process (I) and (II) can be performed. The chamber was equipped with an external plasma source, magnetrons as well as with a carousel including biasable and heatable sample holders where the mirrors were mounted. Process gases were directly introduced into the chamber or through the plasma source.

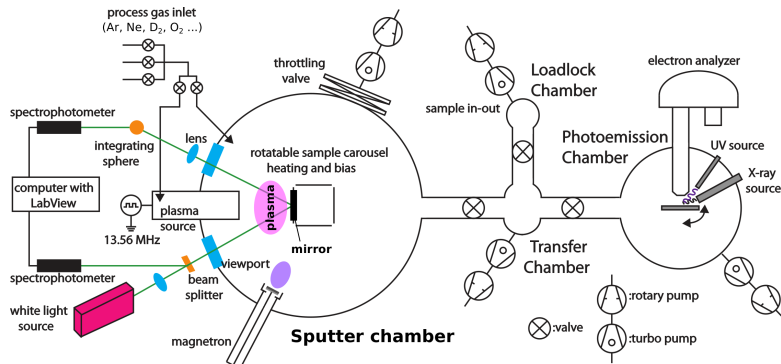


Figure 3.1: Drawing of ESCA-1 facility.

For process (I), samples are coated either with mirror materials (Mo or Rh) or with tokamak-like contaminants (Al and W) as described in section 3.4.3. For process (II), three different methods were employed to create a plasma and accelerate ions to a surface for the removal of contaminants and are briefly described thereafter:

1. **Capacitively coupled RF plasma** The mirror is directly connected to the driven electrode and gas is introduced in the chamber (see Figure 3.2). An RF source provides power applied to the electrode where a matching network is placed in between to automatically match the impedance of the load to the 50Ω impedance of the generator. This matching box also contains the blocking capacitor and DC measuring unit (for V_{bias}). The transmission of power is done through low-loss cables. Finally, the back and side of the electrode is shielded (if not it will be stated) to have a plasma only in the front (where the sample is located). The distance between shielding and electrode was kept small (less than 4 mm) to avoid parasitic discharges in the gap (see Paschen law 2.3). If not otherwise mentioned, 13.56 MHz was employed as excitation frequency.
2. **External plasma source** Plasma is created externally in a Pyrex tube of $\varnothing 120$ mm and 400 mm length mounted on the vacuum chamber (see Figure 3.1). A surfatron (wave launcher) is used to couple the RF power (13.56 MHz) from the RF system (generator + matchbox) to the tube. The plasma is created with 90 W RF power at 3 Pa pressure. As the plasma expands out of the tube towards the vacuum chamber where the sample is located, if the sample is negatively biased, ions can be attracted with a defined energy. The ion energy is then given by the difference between plasma potential (36 V) and applied bias.
3. **Kaufman source** Finally, the last cleaning technique employed an ion beam (not exactly a plasma) produced by a Kaufman source (Ion Tech Inc 3.0–1500–100). Using a neutraliser (W filament), electrons can be added to the ion beam providing neutrality and giving raise to a “plasma” beam. The ion energy is directly controlled in the source by setting up a given negative voltage on the acceleration grid.

ESCA-1 facility was fully equipped with typical diagnostic instruments like pressure gauges, mass spectrometer, temperature sensors and quartz microbalance and other equipment could have been added for specific purposes (ion gun, Langmuir probe ...).

Two main characterizations techniques were employed in this facility, namely in situ XPS and in situ reflectometry both respectively described extensively in section 3.2.1 and 3.2.3. The former was used to determine the chemical composition of the surface of samples either after a coating or before/after a cleaning step to estimate the cleaning advancement. The latter was employed directly during a coating or cleaning process to monitor the change of reflectivity of the sample.

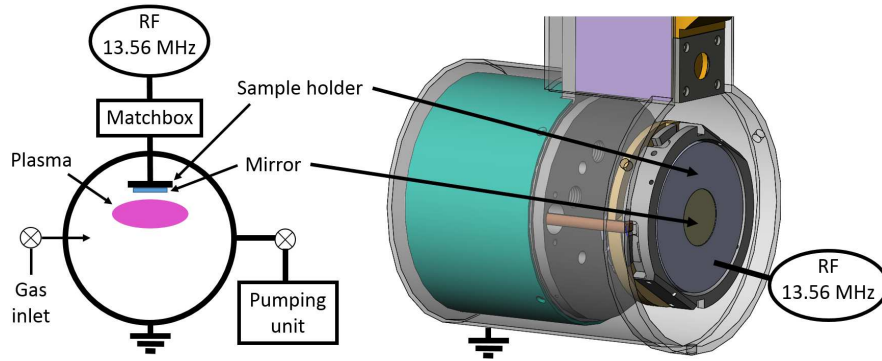


Figure 3.2: Illustration of the system used for capacitively coupled plasma and CAD drawing of the driven electrode with sample holder mounted in a grounded shielding (appears in transparent). The driven electrode is fully shielded except on the front (where mirrors are located) and the gap between shielding and electrode is fixed at 4 mm.

3.1.2 Be chamber

As Be is extremely toxic, a special vacuum chamber was designed and installed in the JET Beryllium Handling Facility (BeHF) to perform cleaning experiments (process (II)) on Be contaminated samples. As many equipments as possible was left outside of the BeHF (in a non-contaminated environment) to allow its reuse. Both vacuum chamber and exterior set-up are shown in Figure 3.3. Inside of the BeHF, a small vacuum chamber was mounted on a frame to be on the same height than the BeHF window for in situ reflectometry measurements (see section 3.2.3). A base pressure below 1×10^{-4} Pa was obtained with a turbo and molecular pump. The plasma necessary for cleaning was obtained using capacitively coupled RF plasma with either Ar, He or a combination of both as processing gas. The electrode could contain up to 12 mirrors with different geometries and was fully shielded except on a few centimetres square where the plasma was created and where the cleaning of a unique mirror took place. To bring the correct mirror on this specific location the electrode was rotated with a motor controlled from outside. In addition, the RF generator and matching box, gas bottles and mass flow controller, pressure display, optical material for ex situ and in situ reflectivity measurements were also located outside of the BeHF. The gas, the light for optical measurements and the electrical power were delivered to the BeHF through feedthroughs located in the BeHF wall.

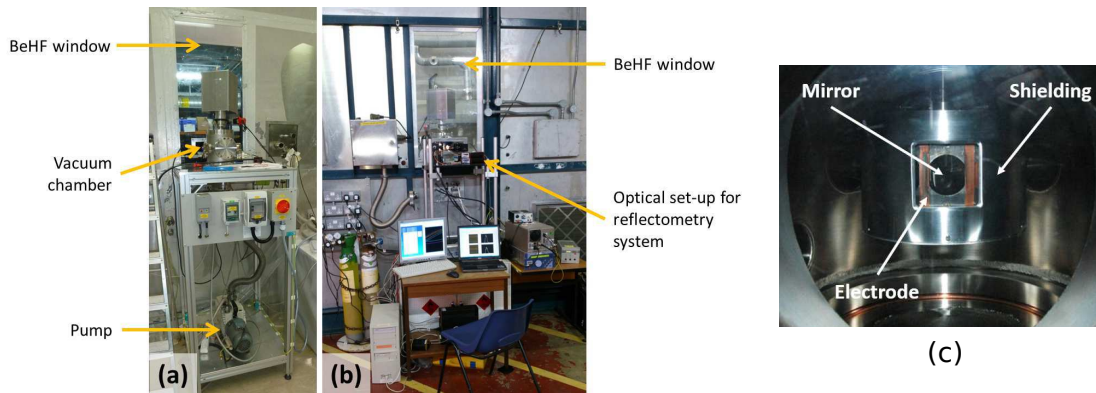


Figure 3.3: (a) Picture of the vacuum chamber installed inside the JET-BeHF in front of a window, (b) of the equipment needed to control the experiments located outside of the JET-BeHF and (c) of the shielded electrode.

As no surface characterisation techniques were directly available at JET, the advancement of the cleaning process was evaluated by monitoring the change of reflectivity of the sample during cleaning. To allow proper light transmission (the BeHF window is made of Plexiglas) a $10 \times 30 \text{ cm}^2$ safety glass was inserted in the window.

3.1.3 B-field Chamber

As mentioned earlier, in situ cleaning in ITER should also be effective in the presence of a strong magnetic field (up to 3.5 T). To obtain such high fields in a vacuum chamber, one possibility is to employ a superconducting magnet used to operate a gyrotron located at the Swiss Plasma Center (SPC) at the Ecole Polytechnique Federale de Lausanne (EPFL) [69] and to insert a specifically designed vacuum chamber in it. The whole experimental set-up is presented in Figure 3.4 and aimed at cleaning samples in B-field (process (II)) using capacitively coupled RF plasma. Depending on the depth where the chamber is inserted in the superconducting magnet, the magnetic field strength will vary between 1 and 3.5 T (Figure 3.4 (a)). Also, by modulating the current provided to the magnet, the magnetic field strength can be increased from zero to its maximum value and its direction can be inverted. The rotatable electrode provides the possibility to perform experiments for various angles α between the magnetic field lines and the sample's surface. First experiments in high B-field were conducted with 3 mirrors inserted in a Cu electrode (see Figure 3.4 (c)) while the second campaign was based on full Cu mirror polished electrodes and coated industrially with 200 nm thick Mo.

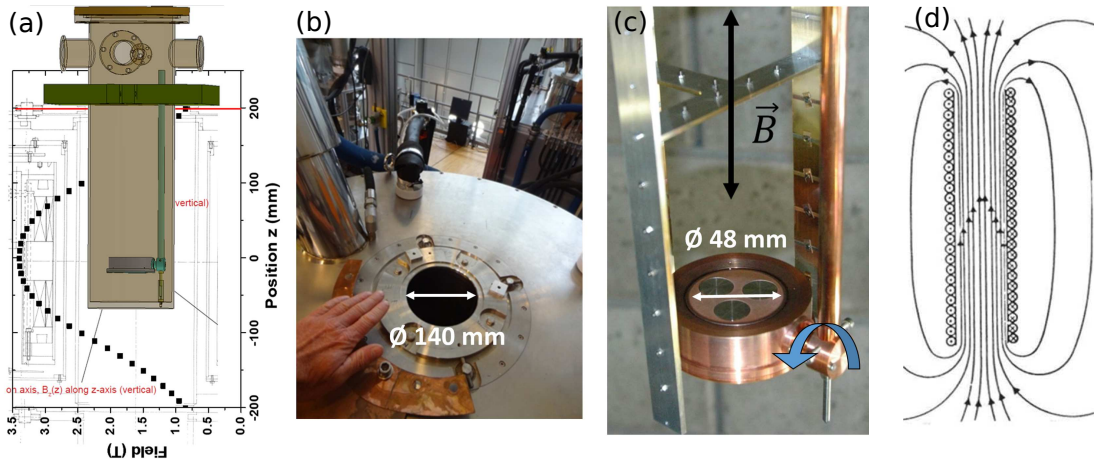


Figure 3.4: (a) Schematic of the superconducting magnet including the magnetic field intensity profile and inserted B-field chamber. (b) Hole in the magnet where the chamber was inserted. (c) Illustration of the electrode (Cu) with 3 mounted mirrors (Mo) and (d) illustration of the magnetic field lines in a solenoid.

Similarly to the two other experimental chamber, a base pressure below $1 \times 10^{-4} \text{ Pa}$ was achieved with conventional pumping. The electrode was fully shielded except on the front where the samples were located. The superconducting magnet consists of solenoids and the magnetic field within the magnet can be considered to be parallel (see Figure 3.4 (d)) with the same strength on the plane located at a given Z position (see Figure 3.4 (a) for Z axis).

3.2 Sample characterization

In this work, samples were thoroughly characterized when possible: before coating, after coating, before cleaning, after cleaning. Depending on the availability and specific requirements of the numerous experimental campaigns, different methods were employed and will be recalled in each of the subsequent experimental chapters. Two techniques enabled to monitor the cleaning

advancement without breaking the vacuum: XPS and in situ reflectometry. The former is only employed in ESCA-1 facility while the latter was used in ESCA-1 facility as well as in the Be chamber.

3.2.1 Photoelectron spectroscopy

XPS is a widely used method for the determination of the chemical composition of the surface of a material and is therefore also called Electron Spectroscopy for Chemical Analysis (ESCA).

XPS is used to investigate core level electrons, ejected from the surface by irradiating the sample with soft X-rays (based on the photoelectric effect [70]). The working principle is as follow: an electron from the sample is excited by an incoming photon, then moves towards the sample's surface where it is ejected. Finally, the electron's kinetic energy is measured with a spectrometer (using a concentric hemispherical analyser). The ejected electrons are called photoelectrons.

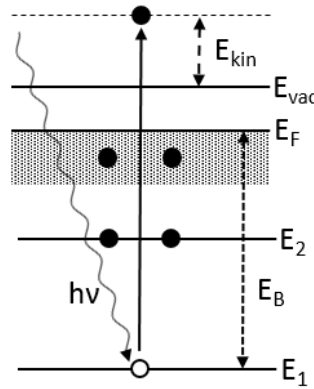


Figure 3.5: Schematic view of XPS.

The binding energy of photoelectrons is an intrinsic material property. Therefore, knowing this value directly informs one about the chemical composition of the surface. Slight changes in the binding energy can be observed for a particular element and energy level, directly depending on the chemical environment of the atom (presence of other elements, alloy formation ...). Knowing the energy of the incoming photon $h\nu$, the kinetic energy of the photoelectron E_{kin} and the sample's workfunction θ , the original binding energy E_B of the photoelectron can be calculated.

$$E_B = h\nu - \theta - E_{kin} \quad (3.1)$$

The work-function θ is the minimum energy needed to remove an electron from the material immediately outside the surface in vacuum (E_{vac}). The binding energy is independent of the materials work-function and only depends on the work-function of the spectrometer which can be measured and is constant.

When photo-emitted electrons escape the material towards the detector, they experience collisions within the material but also in the vacuum. The typical depth of analysis for XPS is given between 2 and 5 nm [71]. To avoid too many losses in the vacuum and absorption of residual gas on the surface, the pressure within the XPS chamber never exceeded 10^{-6} Pa.

The fitting procedure of core level lines was performed with UNIFIT Version 2016 [72] using a convolution of a Gaussian and a Lorentzian and was already described by B. Eren in [73]. Once the peaks are fitted, their binding energies as well as their relative concentrations can be extracted.

In ESCA-1 facility (3.1.1), XPS was performed without breaking the vacuum as samples can be transferred from the loadlock or sputter chamber to the UHV XPS chamber as shown in Figure 3.1. The spectrometer includes a hemispherical analyzer and an X-ray source (Mg $K\alpha$

excitation, $h\nu = 1253.6$ eV) for core-level spectroscopy. The electron binding energy calibration was done by setting the Au $4f_{7/2}$ line of a gold sample to 84.0 eV. The typical resolution of the system is 1 eV at 30 eV pass energy (used for narrow scans).

3.2.2 Scanning electron microscopy

Surface Imaging

Observation of the surface morphology was done by Scanning Electron Microscopy (SEM). A SEM is an electron microscope where a focused electron beam is scanned over the sample's surface. The electrons interact with the sample, emitting various signals that can be processed to obtain information regarding morphology or composition.

Amongst all different signals produced by a SEM, SE and back-scattered electrons are the two signals used to analyse the surface of samples in this Ph.D. thesis. SE are emitted by inelastic scattering between the electron beam and the sample and are collected to produce a topographic image of the sample surface while back-scattered electrons are the result of elastic scattering between the electron beam and the sample and their emission strongly depends on the atomic number of the element. The 'Nano Imaging Lab' in Basel is equipped with an Hitachi S-4800 microscope capable of high-resolution imaging. At 1 kV, the SE image resolution can be 2 nm and it can reach 1 nm with 15 kV. The magnification of the sample can go from $\times 30$ to $\times 800.000$

Energy-dispersive X-ray Analysis

In addition to electrons emitted by the surface and used for imaging, the interaction of the primary electron beam with the matter leads to the emission of X-ray. The principle of the technique is based on a two steps process: (i) the focused electron beam interacts with an atom and can excite an electron upon its ejection, followed by an electron-hole creation. (ii) An electron from an outer shell fills the hole where the difference in energy between the two shells may be released in the form of an X-ray where the energy of the emitted X-ray is characteristic for each element. The X-ray signal can be sorted by energy or wavelength and in this work, Energy-dispersive X-ray spectroscopy (EDX) was employed. As electrons penetrate through the sample, they will experience collisions and loose part of their initial energy. The deeper they penetrate, the more energy they loose up to the point where their energy is insufficient to cause any X-ray emission. If the initial energy is high, they will obviously attain higher penetration depth and thus be able to excite atoms present in deeper sub-surface regions. Figure 3.6 taken from [74] illustrate the aforementioned effect.

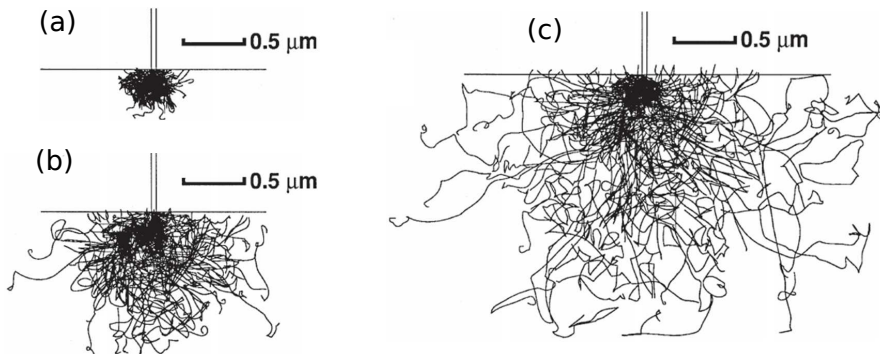


Figure 3.6: Monte Carlo electron-trajectory simulations of the interaction volume in Fe for (a) 10 keV, (b) 20 keV and (c) 30 keV [74].

Although EDX is widely used as a chemical analysis tool to assess the composition of a sample, this technique also provides information regarding the depth distribution of species

for the first hundreds of nanometers. Especially when looking at Figure 3.6, one can observe that X-ray and hence elemental composition information, can be obtained from deeper region when increasing the electron energy. For example, if one imagines a multilayer composed of Mo (few hundreds of nanometers thick) on top of a Cu substrate, having a low acceleration voltage for electrons will result in the absence of X-ray characteristic from Cu. By increasing the electron beam's energy, deeper region can be attained and X-rays from Mo and Cu will be present in the EDX spectrum. The EDX analysis was performed on a SEM-FEI Nova Nano SEM23 microscope, varying the acceleration voltage from 2 to 30 kV.

Thickness estimation with STRATAGem software

EDX measurements are performed for several electron energies and quantified. The quantification results are then fitted with a STRATAGem software that estimates the amount of material (e.g. the thickness if the density is known) of each layer according to the obtained X-ray counts and element properties [75–77].

This method was employed to quantify the amount of Mo on Cu electrodes (with some O due to air contamination) and obtain the Mo film thickness. Figure 3.7 illustrates the EDX analysis, including a view of the fitting software, horizontal and vertical profile lines as well as their location on the Mo-coated Cu sample (approx. 160 nm). The software calculates an amount of material pro area ($\mu\text{g}\cdot\text{cm}^{-2}$) which can be converted to a thickness knowing the density. In our case, we always assumed to have a constant density corresponding to bulk Mo, e.g. $d = 10.2$.

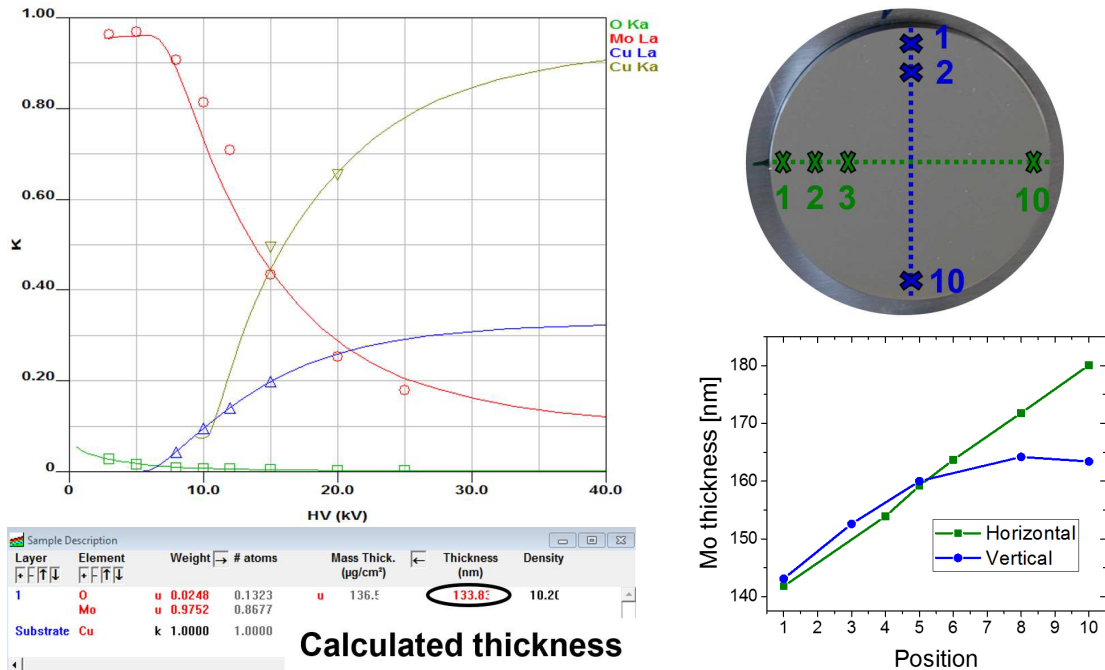


Figure 3.7: Illustration of STRATAGem software fitting the thickness of a Mo thin film on Cu substrate, picture of a Mo coated sample where the mark is indicated with an arrow and profile lines are depicted, and Mo thickness for vertical and horizontal line in function of position for a random non-cleaned sample.

Each sample had a distinctive mark to systematically perform measurements in the same positions (horizontal and vertical to the mark). Usually, 10 equidistant points are measured on one line, the first point (labelled $n^\circ 1$) is made at 1.5 mm from the edge. Each following measurement point is located 5 mm further. As the Mo deposits were not homogeneous over the surface, the thin film thickness could vary from one sample to another but also on the sample itself. Therefore initial characterization of the Mo deposits were performed (with less than 10

points per line) as shown in Figure 3.7. Finally, by estimating the remaining Mo thickness after the cleaning cycle, erosion rates on the different locations can be calculated. This procedure was applied to samples cleaned in the B-field chamber either with or without magnetic field (section 6.1.1, 6.2.1, 6.3 and 6.4).

3.2.3 Optical techniques

Theoretical background

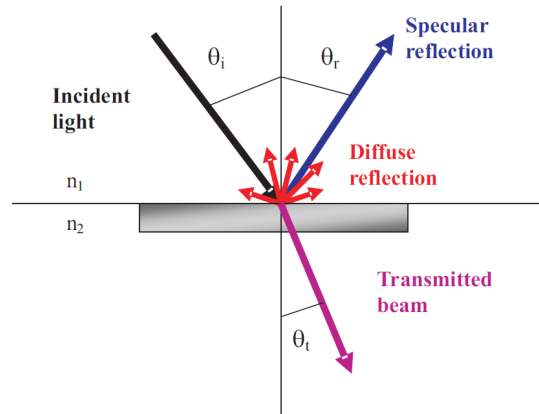


Figure 3.8: Description of the behaviour of the light at the interface between two media.

Let us consider the interface between two media (labelled 1 and 2) with different absolute refractive indexes (respectively n_1 and n_2), e.g. optical properties (see Figure 3.8). When an electromagnetic wave propagating in media 1 encounters this interface with an incident angle θ_i , it is split in a reflected and transmitted part where the angle of reflection θ_r is equal to θ_i . According to the Snell's law,

$$n_1 \sin \theta_i = n_2 \sin \theta_t \quad (3.2)$$

where θ_t represents the transmission angle. The reflectance R represents the ratio between the intensity of the reflected light to the intensity of the incident light. Terminologically speaking, the reflectivity is defined for “thick” reflecting objects while the reflectance term also applies for thin layers and its value can vary with layer thickness. For thick films, reflectivity and reflectance are equivalent. The reflectivity at a certain wavelength depends on several parameters such as angle of incidence θ_i , materials properties (contained in n_1 and n_2) and polarization of the light. Regarding the light polarization, two cases can be distinguished namely s and p-polarized light (perpendicular and parallel to the incident/transmission/reflection plane, respectively). Assuming that the two media are linear, homogeneous and isotropic, one can apply Fresnel equations and evaluate the complex Fresnel coefficients r_s and r_p for the reflected beam for s and p-polarized light, and thus the reflectivity R_s and R_p . For a natural or unpolarized light (containing as much s and p-polarization), R is given by:

$$R = \frac{R_s + R_p}{2} \quad (3.3)$$

The description above only holds for a perfect surface of medium 2. If the surface roughness is comparable to the wavelength of the incident light, part of the reflected light is scattered in all directions and is called diffuse reflectivity. The specular reflectivity, also named mirror-like reflectivity denotes the ability of a surface to reflect the light in a certain direction where, as mentioned earlier, $\theta_i = \theta_r$. The diffuse (resp. specular) reflectivity is defined as the ratio between the intensity of the diffusively reflected light (resp. specularly) to the intensity of the incident

light. Finally, the total reflectivity (R_{tot}) is the sum of the specular and diffuse reflectivities (resp. R_{spec} and R_{diff})

$$R_{tot} = R_{spec} + R_{diff} \quad (3.4)$$

A relation between the surface roughness of a material and the specular reflectivity at normal incidence was given by Bennett in 1961 [78]:

$$R_{spec}(\lambda) = R_0(\lambda)e^{-(4\pi R_{rms})^2/\lambda^2} \quad (3.5)$$

where R_{rms} is the surface root-mean-square roughness, R_0 is the reflectivity of the same material ideally smooth and λ is the wavelength of the incident light. From this formulation, one can clearly set a limit for surface roughening for FMs. If the limit in specular reflectivity loss of FMs is set to 10 %, their roughness should be kept below $\lambda/40$. For diagnostics working in UV, for example at 250 nm, this implies that the roughness should not exceed 7 nm.

Ex situ reflectivity measurements

Most of ex situ UV-VIS-NIR specular and diffuse reflectivity measurements were measured with a Varian Cary 5 spectrophotometer (250–2500 nm) in Basel. A calibrated PolyTetraFluorEthylene (PTFE) probe is used as a reference to determine the absolute reflectivity of each sample. Therefore intensity measurements of the background, made by blocking the incident light ($I_{background}$), and of the PTFE reference ($I_{reference}$) are necessary to calibrate the spectrophotometer. The absolute reflectance is calculated with the formula:

$$R(\lambda) = C(\lambda) \times \frac{I_{sample} - I_{background}}{I_{reference} - I_{background}} \quad (3.6)$$

where $C(\lambda)$ is the absolute reflectance of the PTFE sample at a certain wavelength. The reflected light (total or diffuse) is measured with an 110 mm diameter integrating sphere (also called Ulbricht's sphere) coated with PTFE. The specific geometry of the integrating sphere allows collecting either the total or the diffuse reflectivity. When the incident light arrives on the sample with an incidence angle of approx 3° , the total reflected light is collected by the sphere. With another adjustment, the incident light hits the sample at normal incidence so that the direct reflected beam R_{spec} leaves the sample with the same normal incidence out of the sphere without being measured. In this case, only the diffuse component is measured. The specular reflectivity is obtained by subtracting the diffuse from the total reflectivity.

In some cases, reflectivity measurements were performed in the JET-BeHF for Be-related experiments. The set-up comprised an integrating sphere (PTFE coated), a PTFE reference sample and a spectrophotometer measuring from 400 to 1600 nm and allowed only R_{tot} measurements.

In situ reflectivity measurements

To follow changes of reflectivity during deposition or cleaning processes, an in situ reflectometry system was developed in Basel [79]. The reflectometer measurement part is composed of two spectrometers with a usable wavelength range going from 200 to 1100 nm. A 150 W tungsten halogen light source is providing the light beam to the beam sampler. Thus a small part of the beam (4 %) is reflected back to one of the two spectrometers. This reference signal, which did not travel through the vacuum chamber, is used to correct the reflected signal if the intensity of the light source changes during one experiment. At this point, it is important to notice that the reference signal is only used to account for intensity variations taking place before the entry of the light source into the plasma chamber. Therefore, if the transmittance of the vacuum chamber's windows change during one experiment (due to the coating of the windows), it will not be taken in account in the reference signal.

The main part of the beam is focused onto a 10 mm spot on the sample surface, where it is reflected and exits the vacuum chamber. The reflected beam is collected with an integrating

sphere and measured with the second spectrometer. Thanks to the high power light source, the plasma light has no influence on the reflectivity measurements. In a typical measurement, the dark current of the spectrophotometer is 200–300 counts at room temperature, while the reflected signal is 55000 counts: the dark current can be neglected. The actual light source only permits measurements between 400 and 800 nm.

The system has not been calibrated and is thus not measuring an absolute reflectivity but the evolution of the reflectivity spectrum relative to the first time slice. The evolution of the relative reflectivity (\check{R}) for a given wavelength and corrected with the evolution of the reference signal is given by:

$$\check{R}(\lambda, t) = \frac{I_s(\lambda, t)}{I_s(\lambda, 0)} \times \frac{I_r(\lambda, t)}{I_r(\lambda, 0)} \quad (3.7)$$

where $I_s(\lambda, t)$ is the number of counts at time t and wavelength λ measured by the spectrometer sampling the reflected beam. $I_s(\lambda, 0)$ is the first time slice taken prior plasma start. $I_r(\lambda, t)$ is the number of counts measured by the reference spectrometer and $I_r(\lambda, 0)$ is the average of a number of time slices taken before exposure start. For data acquisition, a LabVIEW program is used.

The in situ reflectometry system was installed on ESCA-1 facility (3.1.1 see Figure 3.1). The primary light beam enters the experiment chamber through a glass viewport, hits the sample surface and gets reflected, and finally exits from another viewport. Impinging and reflected light beams had an angle of 104° between them, and therefore the actual quantity which is measured was the relative reflectivity at $\theta_i = 52^\circ$.

The same system was transferred to JET and mounted on the Be chamber (3.1.2). Due to the geometry of the chamber, the angle between the incident and reflected light beam was approx. 30° .

3.2.4 Other characterization methods

Ion Beam Analysis

Several Ion Beam Analysis (IBA) techniques were employed to characterize samples, either after deposition or after cleaning. For depth-profiling, secondary ion mass spectroscopy (SIMS) was performed either with a VG IX70S double-focusing magnetic sector equipment in VTT Technical Research Centre of Finland or with a Tescan Lyra3 at the EMPA Thun, Switzerland. This technique is used to analyze the composition of surfaces by sputtering the sample with a focused ion beam while collecting and analyzing ejected secondary ions with a mass spectrometer. As the sample is sputtered, it allows one to quantify the elemental composition of a sample's surface in function of the depth.

While SIMS is used for depth measurements, elemental composition analysis of Be contaminated samples (see section 5.1.3) were often performed with nuclear reaction analysis (NRA) and Rutherford backscattering spectrometry (RBS) in the Instituto de Plasmas e Fusão Nuclear in Bobadela, Portugal. The two methods are complementary as they are sensible to different types of atomic masses. NRA is based on nuclear reactions that are induced within the sample due to an energetic primary beam. NRA is sensitive to low-Z elements (Bore, C, N, O ...). The RBS method lies on elastic collision between a high kinetic energy particle from the incident beam with atoms located in the sample. The energy of the scattered projectile is characteristic of the mass of the atoms within the sample. The number of counts allows a direct estimation of the amount of material located on the sample's surface. Both measurement techniques were performed with a 2.3 MeV ^3He beam. The backscattering spectra (RBS) was collected at a scattering angle of 150° and the NRA spectra at 135° . Finally, for some Be contaminated samples, elastic recoil detection analysis (ERDA) was performed in the Alfvén Laboratory of the Royal Institute of Technology in Stockholm, Sweden. The physics behind this technique is very similar to RBS, with the exception that the recoils are detected in the forward detection (for RBS it is the reflected direction). For that purpose, a 36 MeV $^{127}\text{I}^{8+}$ beam was employed to detect heavy

elements. To detect light and heavy elements, IBA methods were mixed, either RBS + NRA or ERDA + NRA. The choice of technique was ruled by the availability of equipments.

Roughness measurements

Roughness measurements of some sample were obtained by performing line profiles. A KLA-Tencor Alpha-Step D-100 device was employed for this purpose, typically averaging five measurements of 1 mm length. In this thesis, average of arithmetic roughness values (R_a) are given.

X-ray diffraction

X-ray scattering techniques reveal information about the composition and crystal structure of a sample. X-ray diffraction (XRD) is based on constructive interferences due to the atomic structure of crystals. XRD measurement were performed using a SIEMENS D500 instrument in θ - 2θ mode from 10 to 100° with a step-size of 0.020°.

3.3 Plasma characterization

In addition to samples, plasmas were also extensively characterized. Two techniques were mainly employed: Langmuir probe and Retarding Field Energy Analyser (RFEA). The former was employed in ESCA-1 and in the Be chamber while the latter served in the B-field chamber. However, both devices were only designed to work in a normal laboratory environment, e.g. without B-field.

Langmuir probe

A Langmuir probe is a plasma measurement device used for a wide range of plasma types and consists of an electrode that is immersed within the plasma bulk. In our case, the electrode was a thin W wire. A sweeping potential is then applied to the probe and electric charge carriers are collected leading to the formation of a current (positive for electrons, negative for ions). The analysis of the obtained current-voltage (I-V) curve allows one to extract typical plasma parameters such as electron temperature, floating and plasma potential, ion and electron density or Debye length [80]. Characterization of plasma used in this thesis was performed with a commercial HIDEN ESPion Langmuir probe.

Retarding Field Energy Analyser

Langmuir probe cannot measure the real ion flux (estimation from the ion density) nor the ion energy distribution of the sample. Therefore, additional measurements were performed with an RFEA, mounted on various systems in the same way as for samples, namely directly on the driven electrode. RFEA is measuring the current drawn to a collector plate (usually ions) as a function of a retarding electrostatic field (discriminating voltage). The measured current is then directly proportional to the number of ions hitting the electrode and by deriving the current in function of discriminating voltage, one can obtain the ion energy distribution function (see for example Figure 4.5 in chapter 4.2). The RFEA used to characterize plasma was the SEMionTM analyser, made by Impedans, Ltd [81] and specially designed to work in a strong RF environment.

3.4 Deposits on FM: coating technique

Different deposition methods were employed for the preparation of reflective metal films or contaminant deposits such as magnetron sputtering, atomic layer deposition (ALD), thermionic vacuum arc (TVA) method or deposition in a linear plasma device. All those methods are based on PVD except for ALD which is classified as a chemical vapor deposition method. Details

regarding the dynamics of PVD and experimental conditions for magnetron sputtering used in ESCA-1 facility (3.1.1) for process (I) are given below.

3.4.1 Physical Vapor Deposition

PVD describes a large variety of vacuum deposition techniques employed to produce thin films. The method is based on a 3-step process:

1. Vaporization of the selected material (target) from a solid source, in our case by plasma sputtering or evaporation.
2. Transport of the particles from the target towards the sample.
3. Reflection or absorption onto the sample's surface.

The thin film growth according to the Volmer-Weber model [82] follows several steps including nucleation, island growth, coalescence of islands to a continuous structure followed by vertical growth as depicted in Figure 3.9.

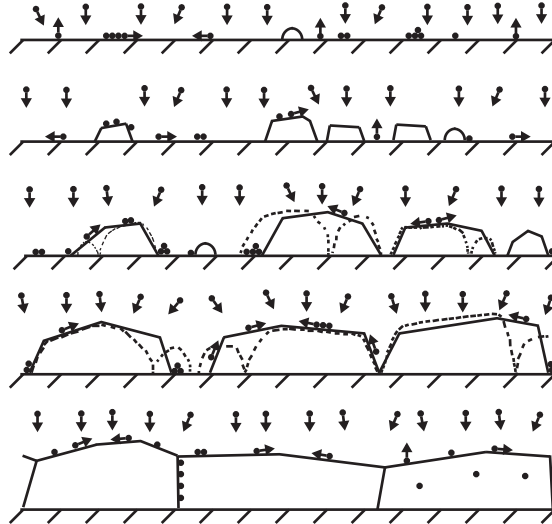


Figure 3.9: Evolution of thin films growing in the Volmer-Weber mode. Illustration is taken from [83].

3.4.2 Sample preparation

Before each deposition process, mirrors had to be prepared. The samples were polished in 3 steps: (i) SiC paper, (ii) diamond paste, and (iii) alumina powder of $0.05 \mu\text{m}$. With this polishing procedure, R_a between 5 and 10 nm was respectively obtained for SS or Mo substrates. The diffuse reflectivity was usually below 3 % for all the mirrors. Prior to installation in the UHV chamber, samples were systematically cleaned in acetone and ethanol in an ultrasonic bath.

3.4.3 Magnetron sputtering

Dense films

Dense films were deposited with magnetron sputtering technique where the magnetron target is facing the sample. The distance between them is kept small (few centimeters) to have a high deposition rate. Physically, a plasma is generated on the magnetron, ions are accelerated to the target with a negative bias causing physical sputtering and ejection of particles. As mentioned

earlier, these particles will condensate on the sample. The plasma can be generated with DC, pulsed DC or RF (for insulating targets). The process gas is commonly a noble gas such as Ar but in the case of reactive magnetron sputtering, O₂ or N₂ can be added for example. To deposit Mo thin films, Ar is used as a process gas and deposition rates in the order of 10 Å.s⁻¹ (measured with quartz microbalance, QMB) were achieved with pulsed DC. More information related to Mo coatings can be found in [84]. Facing magnetron sputtering was also used to produce dense alumina films, simulating ITER contaminants. In that case, the addition of O₂ to Ar during the deposition led to lower deposition rates and fully oxidized deposits using RF at 13.56 MHz. Films deposited with facing magnetron configuration or ALD are denoted by "dense films" hereafter.

Top/bottom magnetron configuration

For the production of tokamak-like films, magnetrons were inserted on the top and bottom of the vacuum vessel, an external plasma was driven using a surfatron and the samples were heated and DC-biased. This configuration was employed in ESCA-1 (see section 3.1.1) and is described in Figure 3.10.

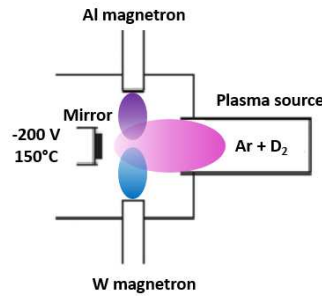


Figure 3.10: *Top/bottom magnetron configuration employed in ESCA-1 facility.*

A certain amount of Ar was included in the D₂ plasma to increase the deposition rates of Al and/or W (deposits of several tens of nanometres were needed) at a total pressure of 3 Pa. The Al or W magnetrons were powered with pulsed DC and the power was adjusted to obtain a given film composition for mixed porous Al/Al_{oxide}/W films (approximately 20 % of W and 80 % of Al). The film thicknesses were estimated with QMB and cross-checked with profilometry. The superposition of all these conditions led to the formation of porous and partially oxidized films (denoted by "porous films" hereafter).

Plasma cleaning techniques

THIS chapter describes the first cleaning attempts with different plasma sputtering methods. The obtained results were crucial to define the most appropriate cleaning technique for ITER which was then investigated thoroughly in the following chapters. One fundamental prerequisite to assess the effectiveness of a cleaning technique is to ensure ITER relevant deposits to be removed from the surface. All tests were performed in ESCA-1 facility (process (I) and (II)). The procedure employed in the various cleaning experiments as well as the results of three plasma cleaning techniques previously described in section 3.1.1 namely external plasma source, Kaufmann source and CCP are given in section 4.1. Section 4.2 is devoted to CCP for cleaning purposes as it was found to be the best technique for ITER. The impact of several external parameters as pressure, supplied RF power and frequency, geometrical conditions of the electrodes or presence of a magnetic field on the discharge's properties and their effect on the sputtering was investigated. The first cleaning results, plasma measurements and simulations for the driven grounded electrode configuration are shown in section 4.2.5.

4.1 Selection of the most appropriate cleaning technique

4.1.1 Plasma cleaning procedure

Samples used in the subsequent experiments were polished Mo mirrors (poly or single crystal), coated with Al and W. All mirrors exhibited similar reflectivity close to handbook reflectivity [85] with low diffuse reflectivity (less than 2 %) prior to deposition. To follow the evolution of the etching process, the evolution of \tilde{R} was recorded in situ. When possible, this method was carried out during deposition of contaminants and cleaning cycle. A reflectivity decrease was systematically observed during the deposition process as shown in Figure 4.1 (a) where \tilde{R} at 450, 575 and 700 nm are plotted. For each cleaning, the process was stopped right after a plateau was observed for \tilde{R} as seen for example in Figure 4.1 (b). The trends observed with this method are used to estimate the cleaning advancement. To confirm the tendency observed with in situ reflectivity measurements, plasma cleaning was occasionally suspended to control the surface composition of the mirror by XPS without breaking the vacuum. Once the deposits were removed, the cleaning was stopped. To avoid excess damage to the mirror, some experiments saw their cleaning being stopped from the moment where Mo was measured by XPS even if the contaminants were not fully removed (a few percent remaining on the surface). In addition to XPS and in situ reflectivity measurements, the efficiency of the cleaning was systematically evaluated with additional ex situ reflectivity measurement and SEM images. Although all aforementioned characterizations were always performed, they won't necessarily be displayed in the succeeding sections.

The influence of ion energy and gas type was not investigated for the selection of the optimum

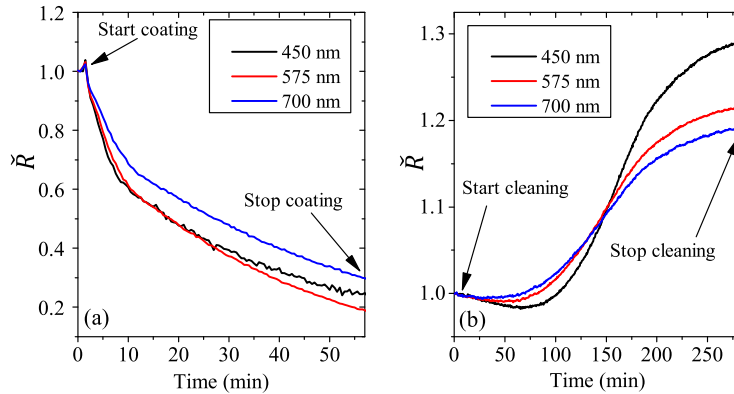


Figure 4.1: *In situ* relative reflectivity measurements of a Mo mirror during (a) deposition of a porous Al/Al_{oxide}/W film followed by (b) an RF cleaning using Ar at 286 eV.

plasma cleaning technique in this section; Ar was chosen due to its efficiency both on light and heavy materials with an ion energy exceeding the sputtering thresholds. The choice of energy and gas type for cleaning will be discussed more in details in chapter 5.

4.1.2 External plasma source

As described in section 3.1.1, the plasma is generated with a surfatron and the mirror is negatively biased. The source was driven with 13.56 MHz RF in an Ar environment where the pressure was set to 3 Pa [86]. The first etching experiment was conducted on a thin porous Al/Al_{oxide} film (see [7]) where Mo was still measured by XPS. The thickness of the contaminant film can thus be estimated to a few nanometres only. For the cleaning, the mirror was biased to -200 V for 1 h. The relative reflectivity evolution of the sample did not change distinctively either during the deposition or during the cleaning and is therefore not shown. No Al was detected by XPS after cleaning and the specular reflectivity was almost restored (loss of 3.36 and 0.8% at wavelengths of 385 and 2000 nm, respectively). Cleaning thin and partially conducting contaminant films seems therefore possible with an external plasma source and DC bias on the mirror.

The second experiment was performed on a 100 nm thick porous Al/Al_{oxide} film (see [7]), initially conducting. XPS measurements revealed the presence of 37 % of Al_{metal}, the rest being oxidized Al and O with the absence of any Mo traces. The cleaning was executed for 5 h 30 min at -100 V bias. No increase of the relative reflectivity nor presence of Mo on XPS after the allotted time have conducted to the increase of the DC bias to -200 V for two additional hours. XPS measurements performed before the cleaning and after each step of cleaning are shown in figure 4.2. It can be seen that the Al was not removed from the surface after the two successive cleaning cycles. With ongoing cleaning, metallic Al disappeared, the film was completely oxidized and became an insulator. In other words, a positive surface charging could build up with the implication that no more ions are attracted to the surface. Sputtering was therefore only effective as long as the film contained metallic species but stopped once the surface of the deposited layer became insulating. The change of a mixed Al/Al_{oxide} film to a pure Al_{oxide} film can be explained either by preferential sputtering, i.e. Al_{metal} is removed faster from the surface because the oxidized form has a lower sputtering yield than the metallic one (approximately factor 10, see table 2.1), or by the transformation of Al_{metal} into Al_{oxide}. Similar effect is known to take place during reactive magnetron sputtering using an Al target with Ar and O₂ as a process gas, and is called target poisoning [40]. During cleaning, incoming ions may transfer an O atom from the surface into subsurface regions, creating new surface sites for O chemisorption. In addition, incident ions might also activate the surface and create new adsorption sites. Finally, O originating either from the residual gas or from the sputtering can

4.1. Selection of the most appropriate cleaning technique

be ionized when travelling through the plasma and be accelerated towards the surface, leading to the formation of an oxide.

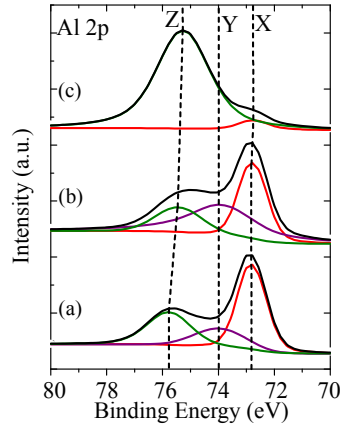


Figure 4.2: *Al 2p core level spectra of Mo mirror after (a) Al/Al_{oxide} deposits, (b) 1st cleaning with external plasma source (Ar⁺, 130 eV) and (c) 2nd cleaning with external plasma source (Ar⁺, 230 eV). The shown spectra are normalized for comparison. The open circles are the measured spectrum and the black lines correspond to the sum curve of all components represented in coloured lines. The vertical lines are given as eye guide for Al_{metal} (X), Al_{surface oxide} (Y) and Al_{oxide} (Z).*

This assumption is confirmed with SEM pictures performed after plasma exposure (see Figure 4.3) showing that the sputtering started but stopped as soon as the surface was fully insulating. The reflectivity especially suffered from the incomplete cleaning, with diffuse reflectivity up to 45 % and specular reflectivity below 5 %.

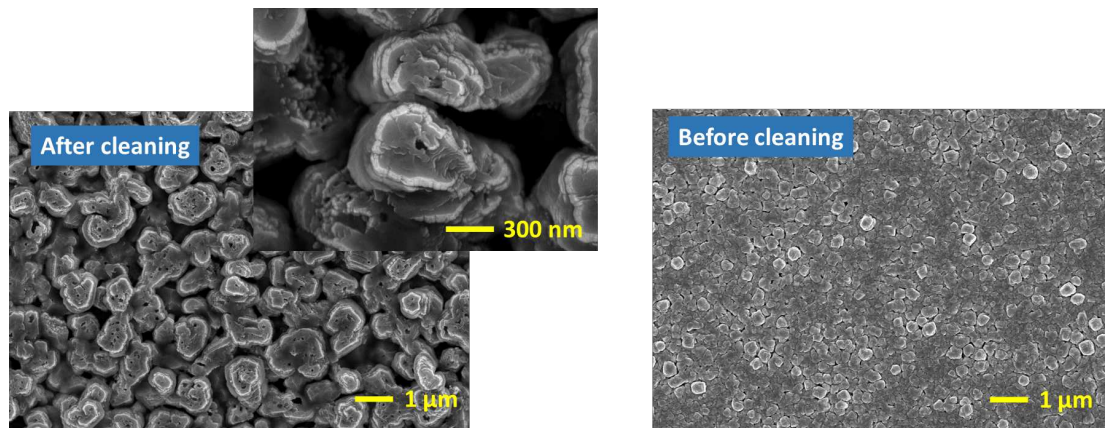


Figure 4.3: *SEM top-view of the sample after DC bias cleaning for a total of 7 h and morphology of the initial coating.*

Although the use of an external plasma source with DC bias on the mirror enabled the removal of thin and non-insulating films, cleaning was not possible for thick insulating coatings. As contaminant deposits could be thick and fully oxidized in ITER, this technique was discarded. Recently, one Russian group working on FMs cleaning started to investigate the use of pulsed DC to overcome charging issue, similarly to the thin film industry and demonstrated promising results [87].

4.1.3 Kaufman source

The working principle of the Kaufman source is described in section 3.1.1. Although possible, the ion beam was not neutralized for the cleaning of a 25 nm thick porous mixed Al/ Al_{oxide} /W film (see [7]) which was partially conducting (through the presence of W_{metal}). XPS measurements revealed 20 % of W_{metal} , 70 % of mixed metallic and oxidic Al and 10 % of O. An accelerating voltage of -300 V resulted in Ar sputtering with an energy of 300 eV and was applied for two hours. Subsequent XPS measurements revealed neither Al nor W. Reflectivity measurements showed a complete recovery of the specular reflectivity. Although this technique showed encouraging results and high versatility (gas, ion energy ...) its implementation in ITER would have required the installation of a plasma source close to all FMs. This aspect of R&D was not further investigated during this Ph.D. thesis and was even abandoned by ITER Organization due to the complexity of the implementation scheme.

4.1.4 Capacitively coupled plasma

The theoretic and working principle of CCP is given in section 2.2 and 3.1.1. Briefly recalling, a given RF power is applied on the mirror in order to achieve the desired self-bias, responsible for sputtering. The first test was performed on a fully insulating coating, namely a pure and dense Al_2O_3 film (18 nm thick). The cleaning was completed within 4 h 30 min with Ar at 0.5 Pa and a self-bias of -200 V. XPS measurements performed after the cleaning revealed the presence of the substrate (Mo) and remaining traces of Al, that could have been removed by extending the etching time, accompanied with an increase of the reflectivity (not shown here as several examples highlighting such recoveries are shown in consecutive chapters).

4.1.5 Summary

Three different techniques were employed to etch contaminants from mirrors. In the case of the external plasma source with DC bias applied to the electrode, the process was found to be effective for thin partially conducting film but limited for thicker insulating films and was therefore abandoned for the ITER in situ cleaning project. The Kaufman source, with its very versatile operation mode, is of prime interest for etching applications and showed promising results. The constraint of insulating surfaces could be overcome with the addition of a neutralizer filament. Nevertheless, due to the extremely complicated implementation of such a device in ITER, this ion generation technique was discarded. Finally, RF capacitively coupled plasma exhibited satisfactory results on the removal of insulating films. This method was therefore chosen for the in situ cleaning of ITER first mirrors. The discharge properties, etching results for a variety of contaminant types, cleaning properties on large mirrors and in strong magnetic fields are presented in the consecutive sections. A basic implementation scheme is discussed in section 6.3.

4.2 CCP: discharge properties

As already stated in section 2.5, the process involved in FMs cleaning is based on physical sputtering through ion bombardment. The efficiency of the sputtering is proportional to the number of ions available in the plasma, in other words to the ion density while the impact energy is determined by the difference between the positive plasma potential and the negative self-bias of the driven electrode. Three parameters were mainly investigated namely self-bias, plasma potential and ion flux using Langmuir probe and RFEA measurements. This whole section does not contain actual cleaning results but focuses on the acquirement of proper discharge parameters, especially when working in ITER-like conditions (large mirrors or presence of B-field).

4.2.1 Influence of discharge parameters

All measurements presented from now on are not issued from a single experiment performed in one vacuum chamber but from several campaigns done either in the ESCA-1 facility or in the B-field chamber. As we are systematically working in strong asymmetric capacitively coupled plasma discharges within given range of power and pressure, the fundamental physic is not changing from one experiment to another and the main outcomes obtained from one set-up, as for example the impact of increasing RF power on the self-bias, are perfectly applicable to another machine. However, as the RF feeding components (lines and connectors) and the electrodes geometry are not the same for the miscellaneous systems, plasma measurements cannot be directly compared.

Throughout the whole thesis, typical discharge pressure p ranged from 0.5 to 3 Pa while the gap d between the electrodes was always between 20 and 30 cm (except for some specific experiment, see section 4.2.2). The minimum and maximum pd parameter is thus equal to 75 and 675 mTorr.cm, respectively. The pd parameter is defining the heating mechanism of the discharge (see section 2.2). As the transition from sheath to ohmic heating (α mode) typically occurs around 200 mTorr.cms [88,89], we can assume that our discharges are governed by sheath and ohmic heating without one process being dominant. One important characteristic of the plasmas used in this work is that they are not dominated by γ mode heating (emission of SE due to ionic bombardment). Indeed, this heating mode requires an RF voltage amplitude > 200 V and neutral pressure ≥ 13 Pa [90] and is accompanied by electron temperatures smaller than unity [90,91]. In this work, discharges were sustained at pressures < 13 Pa and Langmuir probe measurements performed with several gas types and electrodes configurations systematically exhibited an average electron temperature > 1 eV (approx. 2 eV) ruling out γ mode as primary heating source. This finding is particularly important as it implies that the ion-induced SE emission coefficient, specific to each material, should have only minor effect on the discharge properties.

The impact of several parameters (pressure, RF power and frequency, gas type) on the discharge was investigated in the B Field chamber with an RFEA. Figure 4.4 shows the self-bias and the ion flux on the electrode as a function of the RF power applied in a 2.5 Pa, 13.56 MHz argon plasma.

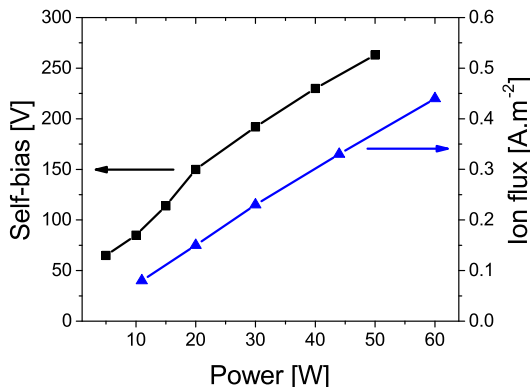


Figure 4.4: Self-bias and ion flux as a function of the applied RF power (13.56 MHz) in argon at 2.5 Pa.

One can observe that when the RF power is increased, the ion flux increases as well, due to the enhanced electron density, hence ionization rate [1,92]. As electrons respond to the fast time-varying electric field, much more electrons are attracted to the electrode when the RF power is larger (higher RF potential). Therefore, to ensure a net zero charge flow on the electrode, more ions have to be collected leading to a larger self-bias (see also Eq. 2.2). Ion flux and self-bias are both increasing almost linearly with applied RF power for the type of discharges used in this

work. Those two parameters cannot be tuned independently from each other.

Figure 4.5 displays several energy ion distributions obtained with RFEA for two excitation frequencies and pressures. Those curves were obtained by differentiating the measured current with respect to the ion energy. All the results acquired with RFEA or Langmuir probe are listed in Table 4.1.

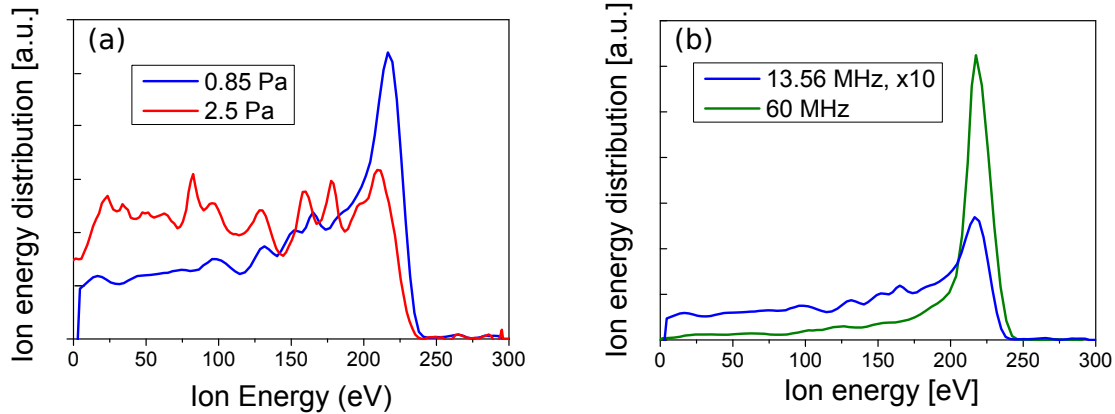


Figure 4.5: Ion energy distribution for argon plasma at -200 V self-bias. (a) 13.56 MHz excitation frequency at 0.85 and 2.5 Pa and (b) 13.56 and 60 MHz frequency at 0.85 Pa where the ion energy distribution at 13.56 MHz is multiplied by 10 for comparison.

At 13.56 MHz, for 0.85 and 2.5 Pa, the RF power was set in order to have a self-bias of approximately -200 V and for a similar self-bias potential, a higher pressure requested a larger RF voltage, hence a higher RF power. This can be explained by the fact that the discharge confinement increases with increasing pressure, leading to a smaller electron flow to the grounded wall and thus, a smaller self-bias on the driven electrode has to develop to ensure a zero net current. As expected the maximum ion energy is spread around a value corresponding to the potential difference between the plasma bulk (positive plasma potential) and the electrode (negative self-bias). As the electrode voltages were roughly the same in the experiment, the difference in maximum energy could originate from a smaller plasma potential for higher pressures [93]. This assumption was confirmed when performing another series of measurements (using Langmuir probe) and where the plasma potential was found to increase with decreasing pressure. In addition the pressure variations exhibited two significant effects as can be observed in Figure 4.5 (a). Firstly, going from 0.85 to 2.5 Pa, the total ion flux is growing. This phenomenon is related to the shorter mean free path at higher pressure, leading to more collisions in the plasma and therefore higher ionization. Secondly, the ion energy distribution function at lower pressure exhibits a sharper distribution around the maxima. The acceleration of ions from the plasma towards the electrode mainly happens within the sheath. The higher the neutral pressure, the more ions will suffer from collisions, decreasing the mean ion energy.

Table 4.1: Plasma parameters obtained for several excitation frequencies and pressures either with RFEA or Langmuir probe for argon plasma. N.A. stands for not measured.

Frequency (MHz)	Pressure (Pa)	V_{bias} (V)	V_p (V)	Max. ion energy (eV)	Ion current ($A \cdot m^{-2}$)
13.56	0.85	-200.0	25.5	217	0.17
	2.5	-199.2	19.0	211	0.23
60	0.85	-199.4	N.A.	217	1.54

At a constant argon pressure and self-bias, the influence of the exciting frequency is displayed

in Figure 4.5 (b). The first important point to mention that is not shown in this figure is the increase in RF power needed to reach a given self-bias. While 36 W were requested at 13.56 MHz, rising the frequency up to 60 MHz led to a needed power of 66 W, almost twice as much as for lower frequencies. This difference can be explained by two very different phenomena, the main effect coming from the physics of the discharge itself while the second is purely technical. The linear relation between the DC self-bias and the RF voltage amplitude (Eq. 2.2) given in section 2.2 is still valid for higher frequencies. Also, the total resistance of the discharge is linked to the RF voltage amplitude and input power (P_p) through the following equation [94]:

$$V_0^2/P_p = (R^2 + (2/\omega C)^2)/R \quad (4.1)$$

where R is the plasma resistance and $1/\omega C$ represents the sheath impedance. Since CCP discharges are mainly capacitive, $R \ll 1/\omega C$ and equation 4.1 becomes:

$$V_0^2 = \frac{P_p}{R} \left(\frac{2}{\omega C} \right)^2 \quad (4.2)$$

and for a given input power, a higher frequency (e.g. ω) implies a decrease of the RF voltage and hence a lower self-bias (observed experimentally). The second reason for a higher requested power emanates from the cables, providing the RF power from the source to the electrode, that experience capacitive losses. Although they are specifically designed for RF applications, a higher frequency brings up more losses, reducing the available power to sustain the discharge. Obviously, as more power can be injected in the discharge at a higher frequency (constant self-bias), the electron and ion density, and thus ion flux increase substantially [1]. Experimentally, the ion flux was observed to increase by a factor 9 when moving from 13.56 to 60 MHz. The last effect of RF frequency on discharge parameter was reported on the sheath thickness that decreases with increasing frequency [93]. This leads to a less collisional sheath and it follows that the ion energy distribution is much more anisotropic as can be observed in Figure 4.5 (b). Working with higher frequencies therefore induces high-density plasma with well defined ion energy distributions. Even if 60 MHz is interesting to get high ion fluxes, the use of this excitation frequency was not in the scope of this thesis and still poses some technical issues as for example matching issues (high reflected power) or melting of cables and connectors (high losses).

When looking for an optimum pressure, one has to take two components into account, namely the increase in ion flux and in the same time decrease of mean ion energy with increasing pressure. The most efficient pressure for argon discharge at 13.56 MHz was thus equal to 1.7 Pa and this value was chosen for the experiments performed in the B field chamber. For other experiments, the pressure was not only defined to optimize the efficiency but also chosen to meet experimental constraints. For example, experiments performed in ESCA-1 used a lower pressure (approx. 0.5 Pa) to decrease the requested RF power to achieve -200 V self-bias and to avoid overheating of cables. Another example of those experimental restraints was observed in the Be chamber, where a higher pressure (2 Pa) was requested to sustain a He plasma (harder to ionize compared to Ar). When possible the discharge parameters were optimized to gain time on the cleaning process. Still, it is necessary to recall that working at slightly lower or higher pressure (0.5 – 2 Pa) does not change the physics involved in the etching technique.

4.2.2 Effect of the wall area

Two points are crucial for in situ RF plasma cleaning in ITER: the possibility to (i) ignite a discharge and (ii) achieve a minimal self-bias ($|V_{bias}| > 100$ V) to sputter contaminants. This was easily achievable in laboratory but the complicated and tight geometry of the front end mirror assembly in ITER optical diagnostic systems might worsen the situation (see for example Figure 4.6).

A set of experiments was therefore performed in ESCA-1 facility with 13.56 MHz excitation frequency and aimed at finding out whether the diminution of the wall (grounded electrode)

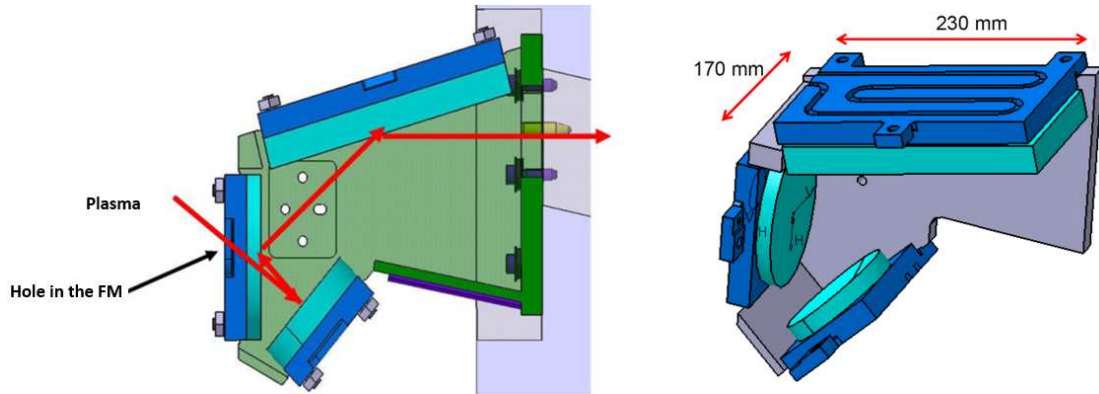


Figure 4.6: Illustration of the WAVS front end mirrors assembly composed of 3 mirrors (light blue in the image). The path of the light beam is represented in red.

area and the gap d between the driven and grounded electrodes had an impact on the discharge. As already stated in section 2.2, a minimum pressure, inter-electrode gap d and RF breakdown voltage are required for gas breakdown and hence ignition of the plasma (see equation 2.3) while the self-bias value depends, among other parameters, on the area of the driven and grounded electrode (see equation 2.2). V_{Brk} for Ar CCP was studied intensively and typical literature values for the minimum in the Paschen curve are around $pd = 0.3$ Torr.cm with $V_{Brk} = 70$ V [51]. In our systems, the inter-electrode gap d is usually around 30 cm. If the working pressure is fixed to 1 Pa, we end up with $pd = 0.225$ Torr.cm, close to the minimum of the Paschen curve. The requested V_{Brk} in our systems is thus only slightly higher than the minimal value of 70 V (e.g. 75–80 V).

To reproduce geometrical conditions that might occur in ITER, a grounded cage (electrode) was placed much closer to the driven electrode (30 mm inter-electrode gap d) with two different diameters (74 or 148 mm). The grounded cage is composed of a metallic disk and surrounding grid to confine the discharge (both are considered to be active grounded area). Such a configuration is displayed in Figure 4.7. Experimentally, without the grounded cage mounted around the electrode, a plasma could be ignited at low pressure, down to 0.1 Pa argon. By adding the grounded cage, the inter-electrode gap d is decreased and thus pd decreases for a constant pressure. To ignite a discharge, a higher V_{Brk} is therefore requested which cannot be increased infinitely (limited by the RF source capabilities). By increasing the pressure to 3 Pa, the pd parameter is again shifting towards the minima of the Paschen curve and it was possible to ignite the plasma at low RF voltages (< 200 V).

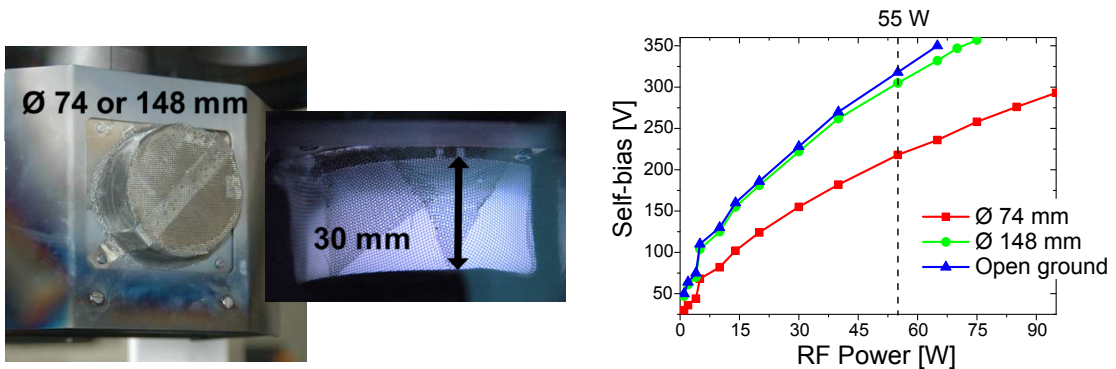


Figure 4.7: Smaller grounded electrodes configuration with here 74 mm diameter. The argon discharge can be seen burning within the grounded cage. Self-bias in function of RF power for Ar at 3 Pa with different ground configurations.

As the plasma can be ignited with the grounded cage at 3 Pa, the impact of different ground configurations was investigated on the self-bias at this pressure. The three configurations are the open geometry (only the walls of the vacuum chamber) and the two grounded cages with \varnothing 74 or 148 mm. The evolution of the self-bias in function of the RF power is illustrated in Figure 4.7 and it can be seen that the \varnothing 148 mm has almost no influence on V_{bias} while for the smaller grounded cage (\varnothing 74 mm), V_{bias} is smaller than for the open geometry. In section 2.2, it was stated that the main parameter influencing V_{bias} for a given RF power was the ratio between grounded and driven electrode area (A_g/A_d). The area of driven and grounded electrodes for the three configurations are given in Table 4.2 with calculated and measured V_{bias} .

Table 4.2: *Experimental and theoretical self-bias obtained for several grounded area configurations at 3 Pa Ar, 55 W RF power (13.56 MHz). The size of the driven electrode (\varnothing 68 mm) does not change.*

Ground geometry	A_g (cm ²)	A_d (cm ²)	Theoretical V_{bias} (V)	Measured V_{bias} (V)
Open	2520	36.3	$0.99 \times V_0 = -320$	-320
\varnothing 148 mm	311.5	36.3	$0.95 \times V_0 = -307$	-305
\varnothing 74 mm	112.7	36.3	$0.72 \times V_0 = -220$	-232

Looking more in details one given RF power, for example 55 W, a self-bias of -320 V was achieved in the open geometry. Equation 2.2 links V_{bias} , V_0 , A_g and A_d , and can be used to calculate V_{bias} . For the open grounded geometry, $A_g/A_d = 0.99$, $V_{bias} = 0.99 \times V_0$ and one can thus assume that V_0 is equal to 323 V. With the \varnothing 148 mm grounded cage, A_g decreases leading to a decrease of the calculated V_{bias} as confirmed experimentally (see Table 4.2). This effect was even more pronounced when the diameter of the grounded cage was further decreased to 74 mm. The calculated V_{bias} values using V_0 estimated from the open geometry are almost a perfect match to those measured during the tests. It was shown that a reasonable self-bias for etching could be achieved in laboratory even with challenging electrode configurations.

4.2.3 Influence of driven electrode area

Similarly to what was done in the previous section with different A_g , the influence of A_d was studied in ESCA-1 facility by increasing the size of the driven electrode in an open ground geometry (A_g is constant). The RF power needed to reach a given self-bias (-200 V) was set for three different driven electrode sizes: \varnothing 68 mm, \varnothing 98 mm and 200×300 mm². All the parameters are listed in Table 4.3.

Table 4.3: *Requested RF power for -200 V self-bias for different driven electrode areas at 0.5 Pa Ar (13.56 MHz). The size of the wall (grounded electrode) does not change.*

Driven electrode size	A_g (cm ²)	A_d (cm ²)	RF power (W)	RF power-per-unit area (W.cm ⁻²)
\varnothing 68 mm	2520	36.3	20	0.55
\varnothing 98 mm	2520	75.4	28	0.37
200×300 mm ²	2520	600	80	0.13

From table, 4.3 it can be seen that increasing the diameter of the driven electrode from 68 to 98 mm (area is approx. doubled), the RF power needed to reach -200 V grows from 20 to

28 W. In both cases, the ratio between A_g and A_d is well above 10 and, using equation 2.2, $V_{bias} > 0.99 \times V_0$. Although one would expect a similar power-per-unit-area (power density) for both electrode sizes, the larger diameter has a smaller value. This could be attributed to the losses that are not taken into account here. The RF power value is representing the total power fed into the system and it could easily be imagined that 12 W are lost between the power supply and mirror, independently of the final electrode size. The plasma generated onto the small and larger electrodes would therefore consume 8 and 16 W power respectively, thus leading to the expected factor of 2.

The size of the electrode was further increased to approach ITER geometry with a $200 \times 300 \text{ mm}^2$ mirror mimicking the ETS FM (see section 6.1.3). Two different materials were used to manufacture this mirror, either SS or anodized Al with $20 \text{ }\mu\text{m}$ of Al_2O_3 on the surface. Similarly, as for the intermediate diameter mirror, the total power requested to achieve -200 V self-bias is larger but the power density value is smaller than expected, probably due to losses not taken into account. Also, as the size of the electrode was increased while the grounded area remained constant, the self-bias should have become smaller according to equation 2.2 ($V_{bias} = 0.82 \times V_0$). The main expected trend namely an increase of the requested power with increasing driven area was observed experimentally. Although the power density should be constant for a given self-bias, it was not possible to prove this statement in the tests due to the RF losses that one could not measure.

4.2.4 Spatial homogeneity of a discharge

Capacitively coupled discharges driven with RF are known to exhibit homogeneous plasma properties over the surface of the electrode regarding ion flux and ion energy when the size of the electrode L is smaller than the vacuum wavelength of the RF excitation λ_0 as shown in [95] for example. The main threat to homogeneity is the standing wave effect that should not be critical (inhomogeneity $< 5 \%$) for $L/\lambda_0 \leq 1/10$ [96]. For clarity, λ_0 and λ_{cable} (wavelength in standard RF transmission cables) are listed in Table 4.4 for 13.56 and 60 MHz excitation frequency.

Table 4.4: Vacuum wavelength and cable wavelength for 13.56 and 60 MHz frequency. The latter is employed for driven grounded electrode mode and is calculated assuming a propagation velocity of $0.66 \times c$ and $0.86 \times c$ for 13.56 and 60 MHz respectively.

Frequency	λ_0 (m)	$\lambda_0/10$ (m)	λ_{cable} (m)	$\lambda_{cable}/4$ (m)
13.56 MHz	22.1	2.21	14.6	3.65
60 MHz	5	0.5	4.3	1.075

The spatial homogeneity study was performed on the ETS mirror mock-up in ESCA-1 facility at 13.56 MHz on the anodized alumina electrode. The largest dimension of the electrode is its diagonal with 360 mm, smaller than $\lambda_0/10$ (see Table 4.4) and no standing wave effect is expected. To confirm those assumptions, Langmuir probe characterisation of the plasma was performed while the actual etching results are presented in section 6.1.3. The Langmuir probe was inserted in the plasma bulk from the top of the chamber and measurements were performed along the surface of the ETS mock-up (see inset in Figure 4.8). Along the surface, both plasma potential and ion flux are constant (Figure 4.8) and homogeneous sputtering of the surface can be expected. The standard error of the mean was added to both measurements.

For larger frequencies that might be used in ITER such as 60 MHz (higher ion fluxes), the L/λ_0 ratio is still smaller than $1/10$ and standing wave effect should not be observed.

Another effect can strongly contribute to inhomogeneity in surface sputtering usually called edge effect. To avoid plasma burning behind the electrode, the backside as well as the side can be

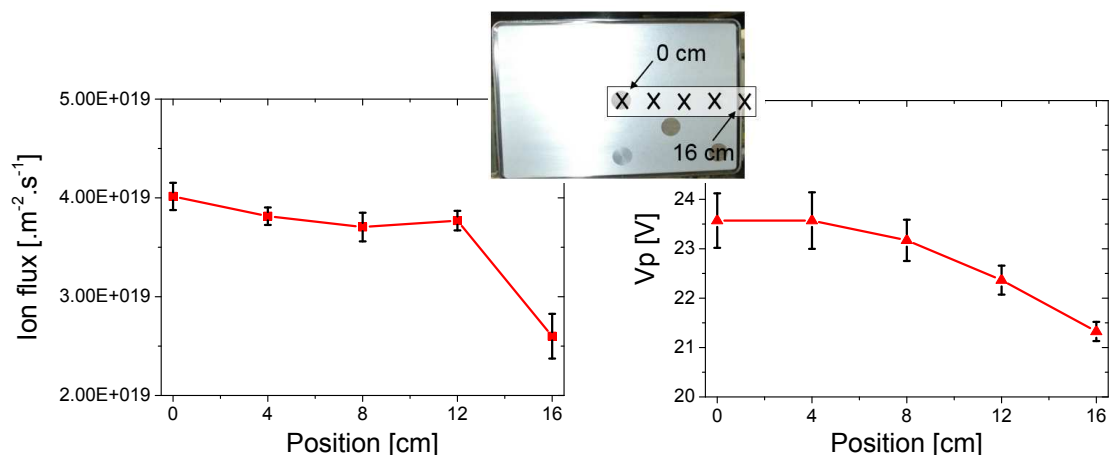


Figure 4.8: Ion flux (left) and plasma potential V_p (right) were measured along the ETS mock-up surface with Langmuir probe from the center (0 cm) to the edge. The discharge was sustained at 13.56 MHz, 0.5 Pa Ar, 90 W RF power for -200 V self-bias. The graphs include standard error of the mean.

shielded with a grounded component. A strong electric field therefore develops on the perimeter of the electrode and will impact, as implied by its name, the edges with a higher sputtering rate in the first millimetres. This effect will be described more in detail in section 6.1.1.

4.2.5 Driven grounded electrode

As previously mentioned in section 2.3, the DC component of a capacitively coupled plasma can be short-circuited by using a $\lambda_{\text{cable}}/4$ long cable grounded at its end (3.65 m for 13.56 MHz, see Table 4.4). By doing so, the driven electrode self-bias, normally responsible for accelerating ions, is obviously equal to zero. In case of a conducting electrode, the self-bias is effectively zero and a high plasma potential is expected (hypothesis I). On the other hand, an insulating surface will act as a capacitor and a negative bias can develop on the surface, although the RF generator will indicate 0 V (hypothesis II). Cleaning experiments and plasma measurements were both done in ESCA-1 facility using 13.56 MHz excitation frequency.

The first etching trial was done on a 50 nm thick pure and dense Al_2O_3 film deposited on a Mo mirror, with Ar as a process gas at a pressure of 1.5 Pa with 50 W RF power. After 1 h of etching, XPS measurements revealed a pure Mo mirror, free from any Al contaminants. Following this good result, another test with similar conditions was conducted on a metallic coating, namely 10 nm of Rh deposited on a Mo mirror. If the plasma potential would remain as usual (approx. 25 V), the ion energy should be below the damage threshold of Ar on Rh (see Table 2.2), and hence no sputtering of the Rh film was expected. After 40 min of etching in the aforementioned conditions, no more Rh was measured with XPS indicating a total removal of the conducting film, in agreement with a plasma potential increase. Measurements with Langmuir probe on the ETS mock-up and plasma simulations were additionally performed to verify the hypothesis I and II.

A plasma was sustained at RF power equivalent to the one needed to obtain -200 V self-bias in the normal CCP configuration. In the case of the anodized Al electrode, plasma potential similar to the normal case were measured, around 20–30 V. When the electrode was replaced by the conducting version, the estimation of the plasma potential was only possible at low RF power. The Langmuir probe voltage range is in fact limited from -100 to 100 V. The evaluation of the plasma parameters was therefore restricted to low RF power due to the positive charging of the plasma with a higher power. The evolution of the plasma potential with respect to the input RF power is depicted in Figure 4.9, with experimental values displayed up to a power of

30 W.

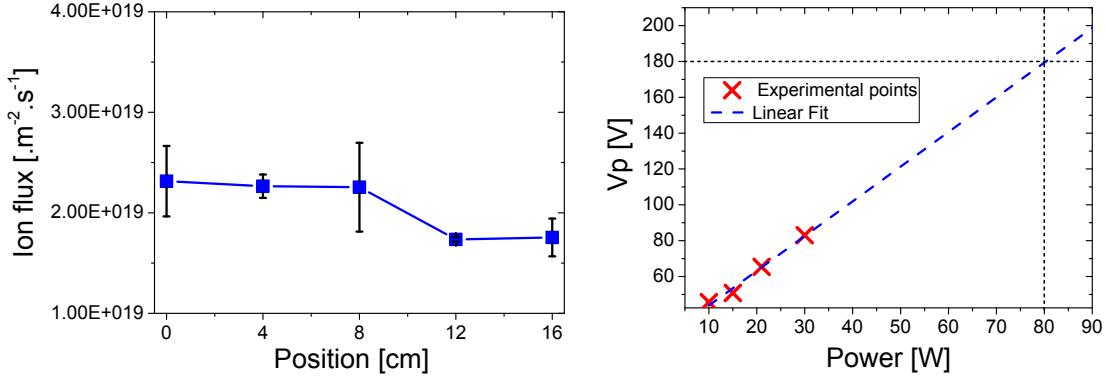


Figure 4.9: Ion flux (left) and plasma potential V_p (right) measured along the surface with Langmuir probe from the center (0 cm) to the edge of the SS ETS mock-up. The discharge was sustained at 13.56 MHz, 0.5 Pa Ar, 80 W RF power for 0 V bias. The graphs include standard error of the mean.

Assuming a linear increase of the plasma potential with increasing RF power, similarly to the evolution of the self-bias in Figure 4.4, a linear fit of the experimental data was performed. The plasma potential extrapolated from this fit corresponding to the RF power requested to obtain -200 V in the normal case, e.g. 80 W, was approximately 180 V. The same figure also shows that the ion flux along the surface of the mirror is almost constant, indicating a homogeneous etching process.

Plasma simulations were performed by Z. Donko and P. Hartmann from the Wigner Research Centre for Physics of the Hungarian Academy of Sciences in Budapest using particle in cell Monte Carlo code (PIC-MCC). The aim of this collaboration was to simulate the specific case of driven grounded electrode in CCP discharges and to compare the simulation with experimental results obtained in Basel. The method employed for the simulation is thoroughly described in [97]. The simulations were run in a strong asymmetric system, the driven electrode being \varnothing 84 mm with a counter grounded electrode of \varnothing 200 mm. The inter-electrode gap was fixed to 114 mm. In the simulations the electrons and Ar^+ ions are traced from their creation by gas phase electron impact ionization or secondary electron emission from surfaces to their absorption on the wall or electrode. The elementary processes included are elastic scattering of electrons on Ar atoms, electron-impact excitation and ionization, and elastic scattering of Ar^+ ions on Ar atoms. Surface processes include absorption and reflection of electrons and SE emission by impinging Ar^+ ions. In the case of the insulating electrode, a 13.56 MHz harmonic voltage waveform with amplitude V_0 and a uniform self-bias voltage V_{bias} is allowed to develop. V_{bias} is iteratively approximated by the simulation code by finding a value that provides a balance between electron and ion fluxes to the electrode area. For the conducting electrode, V_{bias} is forced to be equal to 0 V. The following parameters were used for the simulations, close to the one used experimentally:

- Ar pressure: $p = 1$ Pa.
- RF (13.56 MHz) amplitude: $V_0 = 180$ V.
- Gas temperature: $T = 350$ K.
- Electron reflection coefficient: $\alpha_e = 0.2$.
- SE emission yield: $\gamma = 0.1$.
- Computational grid (z,r): 512 x 512.

The main results obtained from the simulations are depicted in Figure 4.10 and are listed in Table 4.5. It should be noted that the vertical scales are not the same for the different configurations. It can be seen that for driven grounded electrode configuration with an insulating substrate (a, b and c), the plasma potential does not increase and a negative bias can develop on the electrode. The ion energy distributions obtained in this case by simulations are almost identical to the one obtained in the normal CCP mode (see Figure 4.5). When the driven grounded electrode is conducting (d, e and f), the plasma potential increases up to 180 V while the electrode stays at 0 V in simulations, similar to what was observed experimentally (see Figure 4.9). The maximum ion energy is spread around 175 and 150 eV for the insulating and conducting case respectively. In simulations, it appears that the ion energy is slightly lower for the driven grounded electrode case and was also confirmed experimentally in section 6.3. Figure 6.11.

Table 4.5: *Self-bias and average plasma potential extracted from PIC-MCC simulations.*

Electrode	Self-bias (V)	Plasma potential (V)
Conducting	- 164	21
Insulating	0	155
Half-insulating/ half-conducting	- 52	126

The performance of RF discharge with driven grounded electrode was investigated for both extreme cases, fully insulating or conducting. An intermediate case, where the surface of the \varnothing 84 mm electrode is 50 % conducting and 50 % insulating was explored in simulations. In the inner part (insulating) the self-bias is adjusted to reach flux balance of electrons and ions absorbed at the inner electrode, while at the outer ring $V_{bias} = 0$ V is set constant. The results are displayed in Figure 4.10 (h) and (i), and show a charging of the plasma potential to lower values than in the case of the pure conducting electrode while the insulating surface develops a bias voltage. The ion energy distribution, computed for the whole electrode therefore displays two defined energy peaks, one around 170 eV, the other around 120 eV. They respectively correspond to the insulating ($V_{bias} + V_p$) and conducting part of the electrode ($0 + V_p$). The results obtained from the simulations are, to our knowledge, the first ever showing that different ion energy distributions can be obtained on one single electrode exhibiting different material properties locally. Tests and measurements are still ongoing in Basel to support the simulation results.

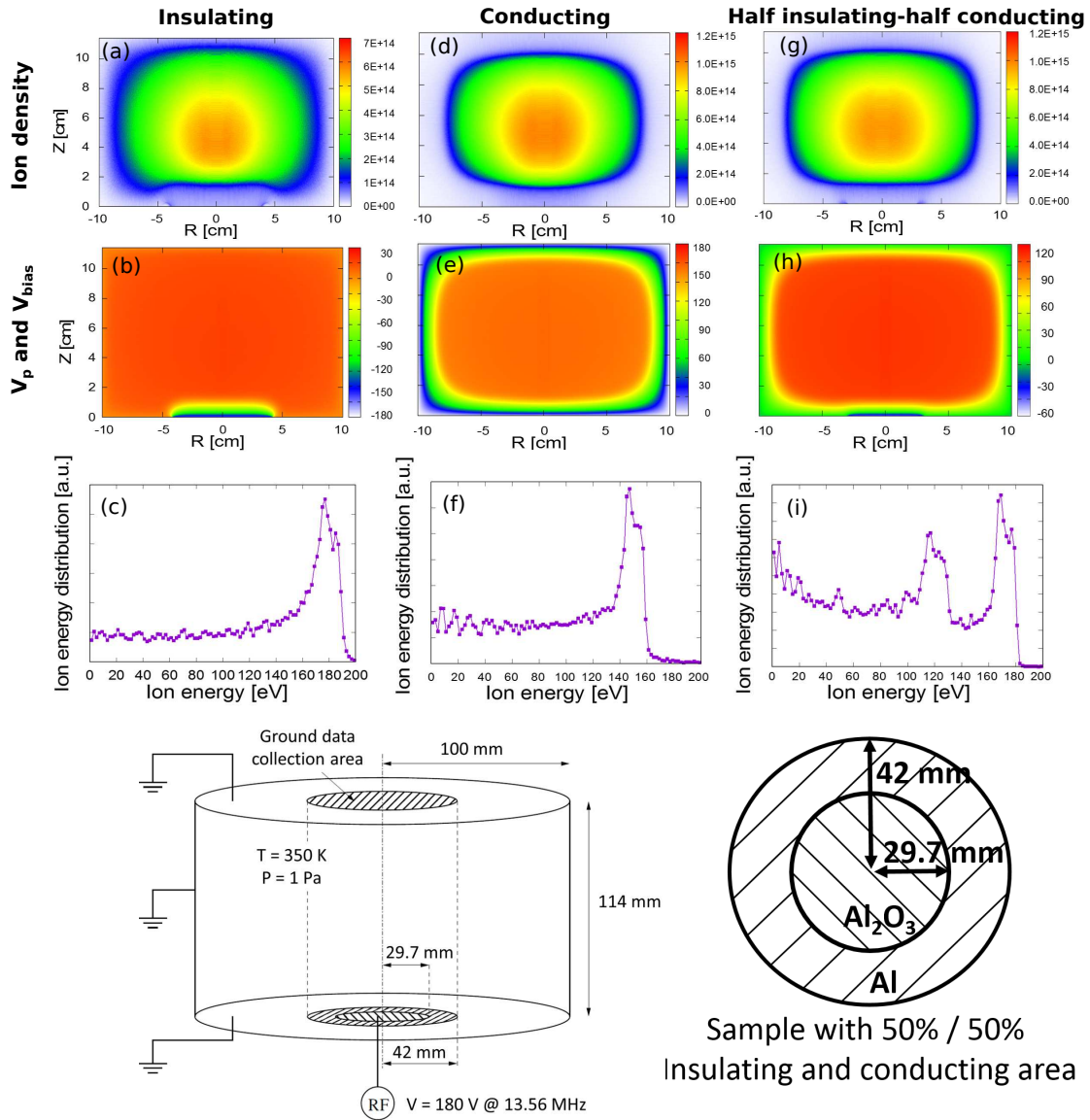


Figure 4.10: PIC-MCC simulation of CCP plasma discharge using Ar at 1 Pa, 13.56 MHz excitation frequency. The simulations were done on insulating (a, b, c), conducting (d, e, f) and half insulating-half conducting (g, h, i) driven grounded electrode. The spatial ion density in m^{-3} (a, d, g), plasma and electrode potentials in volts (b, e, h) as well as the ion energy distribution on the driven electrode (c, f, i) are shown. The simulation geometry and an illustration of the half insulating / half conducting sample are depicted.

4.2.6 Influence of magnetic field

Cleaning experiments were performed in magnetic field up to 3.5 T with various angle between the field lines and the samples surface normal using the B-field chamber. Because of the high magnetic field, the commercial plasma measurements systems (Langmuir probe and RFEA) could not be used to characterize the discharge. Regarding the electron temperature that is typically around 2 eV in non-magnetized discharges used throughout this work, T_e is supposed to increase by a few eVs with increasing magnetic field according to literature [98–101]. In fact, at low pressures, heating through collisions is not efficient due to the large mean free path of electrons. Applying a magnetic field, the electron gyro-motion enhances the probability of collisions and thus the collisional heating. Also, as electrons mainly move parallel to the field lines (no cross-diffusion), the electric conductivity of the bulk plasma decreases and hence, the electric field in the bulk increases. Yet, all the aforementioned studies were completed in weak magnetic fields < 20 mT and measurements of T_e shall be performed in future experimental campaigns in strong magnetic fields.

The evolution of the self-bias with magnetic field was the sole parameter that could be monitored in the present campaign. The results are displayed in Figure 4.11 for three angles between the surface normal and the B-field. For low B-field (< 25 mT), the self-bias strongly decreases due to the confinement of the discharge. Indeed electrons can only flow parallel to the B-field lines and the available grounded area strongly decreases, leading to a diminution of the self-bias (see equation 2.2). The situation gets even worse when the sample is tilted to the B-field (e.g. α close 0°) where the area of the driven electrode projected onto the top grounded wall decreases compared to the case where the electrode is perpendicular to the B-field. This phenomenon was already observed in several studies [102–104]. When the B-field is further increased towards 200 mT, the value of the self-bias increases again. This behaviour was never reported in literature and its origin is not clear. Obviously, as the area of the electrodes is not modified, this increase in self-bias could originate from a change in the collection of charged species by the driven electrode (less ions due to drifts) or a switch in plasma heating mode as reported in [100]. Finally, as the magnetic field is increased further, the absolute value of the self-bias decreases to a minimal value obtained at 3.5 T. Similar results were obtained for the ETS mirror mock-up installed in EAST tokamak (section 6.2.2), not shown in this thesis, but presented in our paper “*Plasma cleaning of ITER edge Thomson scattering mock-up mirror in EAST tokamak*” by R. Yan, currently under review in Nuclear Fusion.

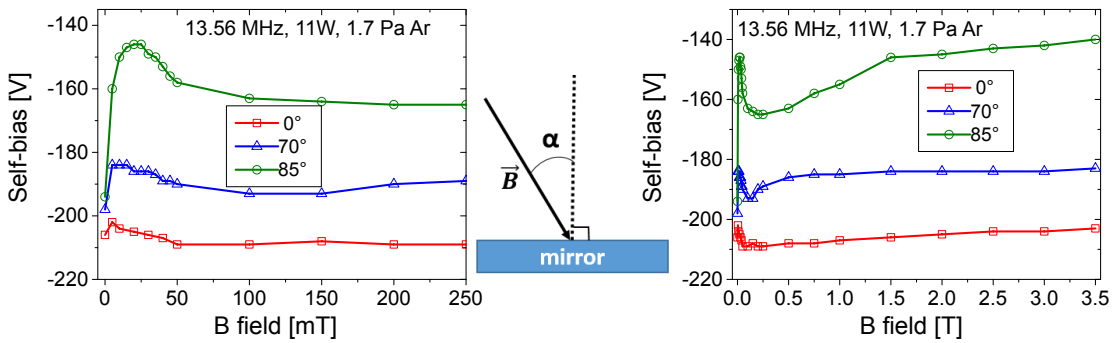


Figure 4.11: Evolution of self-bias with B-field strength at α equal to 0, 70 and 85° .

Influence of deposits

THIS chapter is devoted to the removal of several types of deposits using RF CCP with various process gases and ion energies. To assess pertinent results for the fusion community, the use of ITER mirror materials (Mo or Rh) as well as ITER-relevant deposits is of prime importance. In this work, magnetron sputtering, TVA and linear plasma were employed to produce laboratory deposits with properties as close as possible to those found in tokamaks. The cleaning results of laboratory deposits based on Al (used as a Be proxy) and W mixtures or composed of Be and W are presented in section 5.1. Also, mirrors exposed in JET-ILW were obtained for cleaning and results are presented in section 5.2. In all the trials, the amount of deposits was significantly reduced through physical sputtering, accompanied in the majority of the case with an increase of the specular reflectivity towards initial values. Finally, an outcome of the cleaning results will be given in 5.3.

5.1 Laboratory deposits

5.1.1 Production of contaminants film

The deposition of impurities and its implication on the optical properties of FMs was extensively reviewed in section 1.3.4. The main findings are the following: mirrors exposed in several tokamaks exhibited systematic modifications of their optical properties. Various morphologies were observed on the FMs, from porous structures to dense films. Analysis of mirrors after exposure in JET-ILW revealed a high oxygen contamination in the deposits and almost all species appeared oxidized.

The deposition of contaminants mimicking the one that could be found in ITER was done in several laboratories depending on the type of film to be obtained. Indeed, coatings employing Al as a Be proxy with the addition of W were produced in ESCA-1 facility, either with porous or dense structure and are fully described in our paper [7]. As the laboratory in Basel is not suited for Be due to its toxicity, pure Be films were produced at the University of California San Diego (UCSD) with porous or dense structure. Finally, as Be could not be mixed up with other species in UCSD, additional dense Be containing coatings with D₂ or O₂ as a process gas and W inclusions were done in INFLPR. Be containing deposits produced for this thesis were extensively characterized in our paper [9]. The different types of deposits are summarized in Table 5.1 and the main properties will be given below.

To produce porous Al or Al/W based contaminants in Basel, a specific technique was developed, where the magnetrons are not facing the mirror but are parallel to it. Simultaneously to the deposition, an external plasma source is driven and the sample is negatively biased and heated (to mimic ITER conditions). This is the so-called top/bottom configuration presented

Table 5.1: Types of contaminants produced in Basel, UCSD or INFLPR laboratories.

	ESCA-1	UCSD	INFLPR
Al	Dense and porous	-	-
Al/W	Porous	-	-
Be	-	Dense and porous	Dense
Be/W	-	-	Dense

in section 3.4.3 and depicted in Figure 3.10. Deuterium was used as a process gas (with the addition of 18 % of Ar to increase the deposition speed) and porous deposits similar to the one gathered in a linear plasma device with Be (see Figure 1.11) were obtained. The deposits were partially oxidized with oxygen present through the entire thickness of the deposits. Those type of deposits led to severe degradation of the reflectivity of mirrors, especially in the UV-Vis range and are also labelled as tokamak-like deposits. Also, compact and flat aluminium oxide films were deposited with facing magnetron configuration or with ALD.

The Be based deposits were produced in INFLPR with TVA method. The contaminants (Be and W) are evaporated and gases are included in the process to be more ITER relevant (either D₂ or O₂). Three different types of film were produced on Mo mirrors namely Be + D₂, Be + O₂ and Be + W + D₂ (up to 10% of W in the deposits) that systematically exhibited a dense structure. Be was always in oxidized (BeO) and metallic state, and additionally present as an alloy (Be₂W) for Be + W + D₂. In UCSD, the mirrors were coated with a linear plasma device (PISCES-B) or with magnetron technique. For the former, D ions are accelerated towards a Be target and ejected material is re-deposited on the mirror. The films are porous, oxidized and contain a high amount of D. Additional samples were coated with Be in a magnetron sputter system and exhibited dense layers, mainly metallic with a low amount of incorporated D. The contaminant film always led to a decrease of the reflectivity, with huge losses (up to 85 % at $\lambda = 250$ nm) for the most porous deposits done in PISCES-B.

5.1.2 Cleaning of Al/W based deposits

Cleaning experiments were performed on the porous and dense type of deposits. An example of porous Al/Al_{oxide} film deposited on a Mo mirror, approx. 30 nm thick is shown in Figure 5.1 and exhibits a 50 % loss at 450 nm. The losses are composed of: (i) an increase of the diffuse reflectivity due to the roughening of the surface (approx. 20 % loss) and (ii) a decrease of the total reflectivity because the deposited film is not perfectly transparent as well as from the deuterium exposure of the Mo surface, leading to deuterium implantation as already shown in [73].

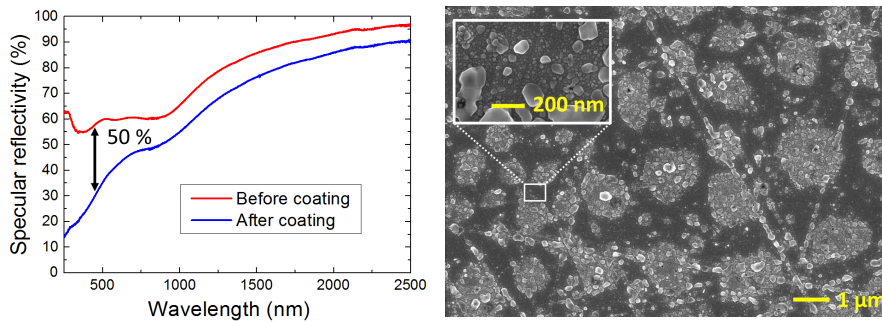


Figure 5.1: Specular reflectivity drop of 50 % at 450 nm of a Mo mirror (before coating; red line) after the deposition of porous Al/Al_{oxide} film approx. 30 nm thick (after deposition; blue line). The SEM image of the corresponding film is given.

In addition, dense Al_2O_3 films were also cleaned. A 25 nm thick layer is displayed in Figure 5.2 with a typical nanocrystalline morphology. This kind of films exhibited low roughnesses and thus, diffuse reflectivities similar to the substrate ones. The total reflectivity is impacted by the deposited alumina layer and calculation using a Mo substrate and an Al_2O_3 film of 32 nm thickness (using optical constants n, k from [85]) showed a perfect agreement with experimental values.

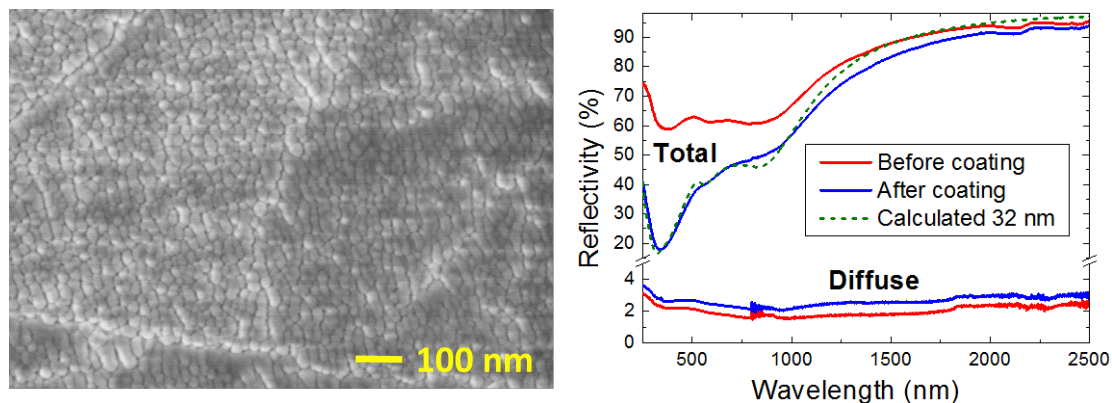


Figure 5.2: SEM image of 25 nm thick Al_2O_3 film deposited with facing magnetron on a polycrystalline Mo mirror and total and diffuse reflectivity before and after coating. Calculated reflectivity (with n, k from Palik [85]) were added for comparison with a Mo substrate and 32 nm of Al_2O_3 .

The plasma cleaning procedure mentioned in section 4.1.1 was employed for the subsequent experiments, using in situ reflectometry and XPS to quantify the cleaning advancement. SEM and ex situ reflectivity measurements were performed afterwards to characterize the cleaning efficiency. Experiments with Ar, Ar + D_2 and Ne were conducted with a pressure of 0.5 Pa. When the self-bias was swept from -150 to -260 V, the plasma potential was approx. 26 V and the maximum ion energy is given by the difference between the plasma potential and the self-bias. Using RF plasma at 13.56 MHz, the deposits were almost always fully etched, followed by a recovery of the reflectivity. Once the deposits were removed (total removal, e.g. “T.R.” in Table 5.2), the cleaning was stopped. To avoid excess damage to the mirror, the cleaning was stopped for few experiments from the moment where Mo was measured by XPS even if the contaminants were not fully removed (a few % remaining on the surface, denoted partial removal, e.g. “P.R.” in Table 5.2). To validate this technique for ITER, cleaning were performed on porous as well as on compact films, presented in Table 5.2 and summarized as follow:

- A 200 nm thick porous Al/ Al_{oxide} film was removed using Ar at 286 eV;
- Porous W film (80 nm) was withdrawn from a mirror using Ar at 286 eV;
- Mixed porous Al/ Al_{oxide} /W films (25–350 nm) were removed using Ar, Ar + D_2 or Ne (ion energy varied from 176 to 286 eV);
- A dense Al_2O_3 film deposited with magnetron (50 nm) was removed using Ar at 226 eV;
- A 50 nm thick Al_{oxide} film deposited by ALD was partially withdrawn with Ar at 226 eV.

To assess the efficiency of the cleaning on the optical properties, the total and diffuse reflectivity of each sample were measured before deposition of contaminants and after cleaning. The specular reflectivity change (in %) was calculated by subtracting the final to the initial reflectivity. An example of reflectivity measurements is shown in Figure 5.3.

Table 5.2: Cleaning results on various films deposited on Mo mirrors with RF discharge cleaning. The reflectivity change (in %) represents the difference in specular reflectivity between the bare Mo mirror and the Mo mirror after plasma cleaning of the deposits. The estimated sputter rate was obtained with the estimated thickness of the deposits (obtained with QMB) divided by the cleaning time. N.A. stands for not measured.

Deposited film	Cleaning conditions	Result	Reflectivity change (%)		Estimated sputter rate nm/min
			385 nm	2000 nm	
Porous W film (80 nm)	286 eV Ar	T.R.	- 1.9	- 2.5	0.21
Porous Al/Al _{oxide} film (200 nm)	286 eV Ar	P.R.	- 1.6	- 2.0	0.56
Porous Al/Al _{oxide} /W film (350 nm)	286 eV Ar	P.R.	- 1.5	+ 1.0	0.38
Porous Al/Al _{oxide} /W film (310 nm)	286 eV Ar/D ₂	T.R.	- 1.5	+ 0.4	0.31
Porous Al/Al _{oxide} /W film (40 nm)	286 eV Ne	T.R.	- 1.1	- 1.9	0.07
Porous Al/Al _{oxide} /W film (25 nm)	176 eV Ar	T.R.	+ 0.8	+ 1.0	0.19
Dense Al _{oxide} film (magnetron, 50 nm)	226 eV Ar	T.R.	N.A.	N.A.	0.02
Dense Al _{oxide} film (ALD, 50 nm)	226 eV Ar	P.R.	N.A.	N.A.	0.40

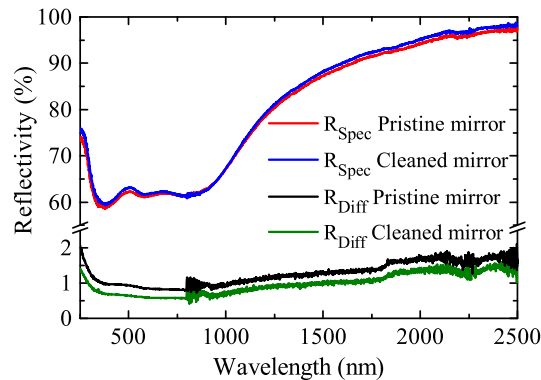


Figure 5.3: Specular and diffuse reflectivity of a Mo mirror before deposition of porous Al/Al_{oxide}/W film (Pristine mirror; resp. red and black line) and after cleaning of the deposits with Ar at 176 eV (Cleaned mirror; resp. blue and green lines).

Using the estimated sputter rate, the most efficient gas for sputtering appeared to be Ar (in comparison to Ar + D₂ or Ne) and higher energies lead to faster cleaning. Considering the film morphology, porous and not fully oxidized deposits were removed much faster than dense oxidized films. Finally, XPS measurements conducted before, in between and after cleaning of porous films indicated four trends:

- Similar to the results with the external plasma source, the ratio of Al metallic to oxidic Al decreased during the cleaning of porous Al/Al_{oxide} and Al/Al_{oxide}/W films (figure 5.4). This phenomenon can be explained through selective sputtering and/or continuous oxidation of the film (target poisoning [40]);
- Selective sputtering was also observed during the cleaning of porous Al/Al_{oxide}/W films where the Al/W ratio was decreasing with ongoing cleaning (sputtering yields at 200 eV for Al and W are 0.5 and 0.2 ejected atoms per incoming ion, respectively);
- During the cleaning of porous Al/Al_{oxide} and Al/Al_{oxide}/W films, the binding energy of the Al_{oxide} peak was shifting towards lower values (figure 5.4);
- For W, either in porous W or Al/Al_{oxide}/W films, no changes were observed for the XPS measurements as displayed in figure 5.4.

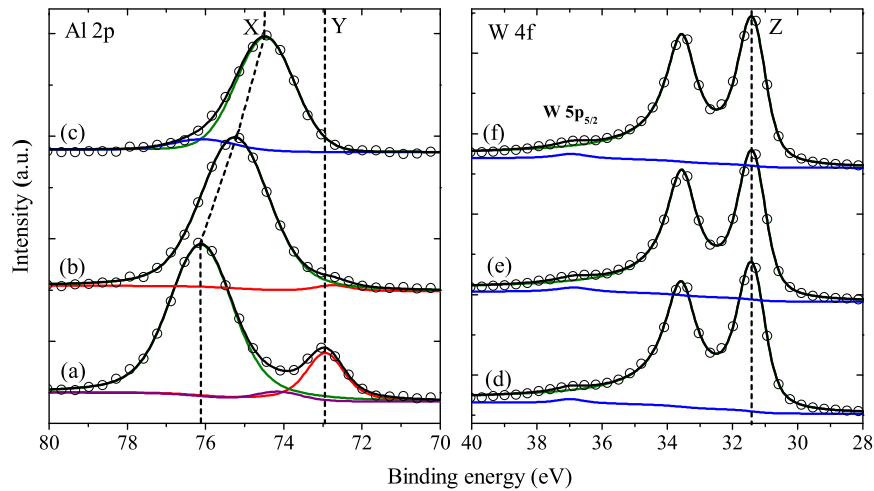


Figure 5.4: Core level spectra of (a) Mo mirror after the deposition of a porous Al/Al_{oxide} film followed by respectively two RF cleanings with Ar (resp. (b) and (c)), and (d) Mo mirror after the deposition of a porous W film followed by respectively two RF cleanings with Ar (resp. (e) and (f)). The shown spectra are normalized for comparison. The open circles are the measured spectra and the black lines correspond to the sum curve of all components represented in colored lines. The vertical lines are given as eye guide for Al_{oxide} (X), Al_{metal} (Y) and W_{metal} (Z).

To briefly summarize the obtained results, tokamak-like deposits containing Al and W as well as dense Al₂O₃ films were deposited on Mo mirrors and removed with RF plasma at 13.56 MHz. The RF discharge cleaning has demonstrated successful removal of deposits under a wide range of conditions (use of Ar, Ar + D₂ or Ne with ion energies ranging from 176 to 286 eV) while restoring the mirror's optical properties. As laboratory experiments are only possible with Al used as a Be proxy, the cleaning process of mirrors deposited with Be should be validated. This is the task of the subsequent sections, where production and cleaning of Be, BeO and BeW films using RF plasma will be reported.

5.1.3 Be/W based laboratory deposits

Because of the toxicity of Be, the first ever plasma sputtering experiments of tokamak-like films containing Be have been performed in the JET-BeHF installed in the Culham Science Centre in England. For a better understanding, samples belonging to a given type of deposit will share a root name. For example, two samples coated in INFLPR with Be + D₂ will be denoted as R1-1 and R1-2. A complete listing can be found in Table 5.3.

Table 5.3: List of mirrors indicating the deposition technique and the expected thickness of the contaminant film. Samples from UCSD (PISCES-B and Be coater) were characterised with RBS and NRA (units are 10¹⁵ atoms per cm²). Samples from INFLPR (TVA deposition) were quantified with XPS (relative amount of each species is given in %).

Mirror	Deposition technique	Expected thickness	Be	D
P1	PISCES-B: Be + D ₂	60 nm	369	238
P2	Be coater: Be + Ar + D ₂	60 nm	1569	94

Mirror	Deposition technique	Expected thickness	Be	W	O
R1	TVA: Be + D ₂	30 nm	70.2 %	-	29.1 %
R2	TVA: Be + O ₂	30 nm	70.7 %	-	29.3 %
R3	TVA: Be + W + D ₂	30 nm	67 %	10.8 %	22.2 %

Reflectivity measurements of the different types of samples before cleaning are presented in Figure 5.5.

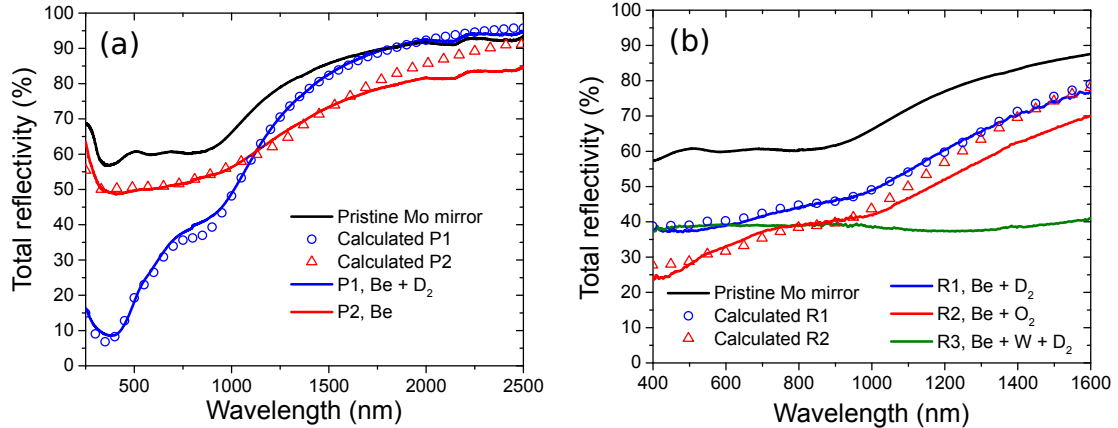


Figure 5.5: Total reflectivity of deposited mirror from (a) UCSD and (b) INFLPR with calculated reflectivity (with n, k from Palik [85]) were added for comparison. In (a) calculated P1 corresponds to a Mo substrate with an oxidized surface (5 nm MoO₃) and a 60 nm thick mixed BeO/Be layer (20% Be) with air inclusion (60%) while P2 was modelled with a Mo substrate (+ 5 nm MoO₃) covered with 60 nm of mixed Be/BeO layer (10 % BeO). In (b) R1 and R2 can be approached theoretically with an Mo substrate (+ 5 nm MoO₃) covered with a 30 nm mixed Be/BeO layer (respectively 30 and 45 % BeO for R1 and R2). The samples from INFLPR were measured in JET from 400 to 1600 nm.

The total reflectivities were approached with a theoretical fit using systematically a slightly oxidized Mo mirror as substrate (5 nm MoO₃ due to air storage between polishing and contaminants deposition). Mixed layer were then added to the Mo substrate to simulate the deposited contaminants calculated with optical constants (n, k) from [85] and described by the Bruggeman

effective approximation [105]. For P1, P2, R1 and R2-type films it was possible to match almost always perfectly the calculated reflectivity to the measured one as displayed in Figure 5.5 and fitting parameters are listed in Table 5.4. It was not possible to fit R3-type of layers.

Table 5.4: *Fitting parameters used to calculate reflectivities of Be coated mirrors with optical constants (n, k) from [85]. A Mo substrate with surface oxidation (5 nm MoO_3) was used.*

Mirror	Be	BeO	Thickness	Voids
P1	20 %	80 %	60 nm	60 %
P2	90 %	10 %	60 nm	0 %
R1	70 %	30 %	30 nm	0 %
R2	55 %	45 %	30 nm	0 %

The cleaning was performed in the Be chamber described in section 3.1.2 with CCP at 13.56 MHz. Langmuir probe measurements performed in Basel exhibited plasma potential around 30 V. For some samples, V_{bias} up to -600 V were requested, leading to a high RF power input. The collection of high ion fluxes with high ion energies on the mirrors was therefore enhanced and mirrors could have been heated up to a maximum of 100°C . All the discharge conditions (gas, pressure and ion energy) applied for the cleaning are listed in Table 5.5. In contrary of cleaning performed in Basel where in situ XPS was used to assess the etching advancement, in situ reflectometry was the sole characterization method available during the cleaning process. Ex situ total reflectivity measurement from 400 to 1600 nm was the only characterization technique available on-site. For IBA, XPS or SEM, the samples were sent to other facilities. The total reflectivity recovery (see Table 5.5) was calculated at two wavelengths, namely in the visible (400 nm) and in the infra-red (1600 nm) using measurements done ex situ on pristine, contaminated and cleaned mirrors according to equation 5.1:

$$\text{Total R recovery (\%)} = \frac{R_c - R_d}{R_i - R_d} \times 100 \quad (5.1)$$

where R_i , R_d and R_c correspond to the initial total reflectivity of the pristine Mo mirror, after deposition (before cleaning) and after cleaning, respectively. A complete recovery of the total reflectivity would give a value of 100 % while a degradation of the total reflectivity through cleaning would lead to a negative value.

The choice of appropriate gas for sputtering is fundamental. Deposits have to be removed as fast as possible and the mirror's integrity should be preserved. According to Table 2.1, He seems to be the better option with selective sputtering of Be while W can be removed, although with small rates (not possible with hydrogen), using for example 200 eV. Ar on the other hand seems to be effective on all types of materials. Therefore several experiments were conducted with pure He or Ar, to see the effect on removal but also on the mirror's optical properties. A mixture of them were also tried out.

All Mo mirrors were strongly oxidized after the cleanings performed in the JET-BeHF but some were Be free. To prove that optical properties could be recovered, some mirrors underwent a second cleaning in Basel ESCA-1 facility with conditions listed in Table 5.5.

Table 5.5: List of experimental conditions applied for each mirror in the JET-BeHF (J) and in Basel (B). For some samples, two cleanings were performed in one location with different conditions. In that case each of them is labelled separately (J-1/J-2 or B-1/B-2). When a gas mixture is used, the partial pressure ratio is expressed in brackets. NRA and RBS characterisations were performed after cleaning.

Mirror	Conditions (pressure in Pa)	Cleaning time	Total R recovery (%)		IBA, Be (10^{15} at./cm 2)
			400 nm	1600 nm	
P1-1	(J) 2 Pa He; 630 eV	6 h 50	60	62	0-10
P2-1	(J-1) 2 Pa He; 230 eV	12 h	-	-	0-20
	(J-2) 2 Pa He; 630 eV	9 h	14	81	
P2-2	(J-1) 0.5 Pa Ar; 230 eV	16 h	-	-	0
	(J-2) 0.5 Pa Ar; 630 eV	4 h	-5	92	
R1-1	(J) 1 Pa He + Ar (90/10); 330 eV	9 h 10	55	90	0
R1-2	(J) 2 Pa He; 330 eV	7 h	29	102	0-50
R2-1	(J) 1 Pa He + Ar (90/10); 330 eV	5 h	47	101	0
	(B) 1.5 Pa H $_2$ + Ar (50/50); 180 eV	5 h	100	97	
R2-2	(J) 2 Pa He; 630 eV	2 h 50	50	60	0
	(B-1) 2 Pa He; 430 eV	10 h	81	61	
	(B-2) 2 Pa He; 430 eV	7 h	104	83	
R3-1	(J) 2 Pa He; 630 eV	5 h 30	25	92	0
	(B-1) 1.5 Pa H $_2$; 100 eV	4 h	48	86	
	(B-2) 1.5 Pa H $_2$ + Ar (50/50); 180 eV	4 h	98	94	
R3-2	(J) 1 Pa He + Ar (90/10); 330 eV	8 h 20	51	101	0-50

Preliminary results

Initially, working with low ion energies was considered. In an attempt to characterize the cleaning speed, two mirrors were therefore cleaned with He and Ar at 230 eV ion energy.

Mirror	Conditions	Cleaning
P2-1, Be	(J-1) 2 Pa He; 230 eV	12 h
P2-2, Be	(J-1) 0.5 Pa Ar; 230 eV	16 h

Immediate off-site characterization with SIMS indicated a removal rate of 0.03 nm/min for both gases. Currently, there is no database for the sputtering yield of Ar on BeO. Langmuir probe measurements performed in Basel exhibited a 4 times higher ion flux for Ar and one can therefore assume that Ar possesses a 4 times smaller sputtering yield than He, e.g. 4×10^{-3} at./ions at 230 eV. Briefly recalling results from section 5.1.2, a dense Al_2O_3 film was etched using Ar at 230 eV with a sputter rate of 0.02 nm/min. The ion fluxes measured with Langmuir probe were similar for He in the Be chamber and Ar in ESCA-1, and the sputtering yield are equivalent (see table 2.1). As expected similar sputter rate were recorded for both samples cleaned in JET and ESCA-1. Erosion rates had to be increased due to the limited availability of the JET-BeHF and therefore the maximum ion energies were adjusted upwards (going from 230 eV to a range of 330 – 630 eV).

Cleaning at higher energies, P1 and P2 coatings

After the second cleaning at higher ion energies for the two aforementioned samples, all contaminants were nearly removed (traces of Be observed in the center of P2-1).

Mirror	Conditions (pressure in Pa)	Cleaning time	IBA, Be (10^{15} at./ cm^2)
P2-1, Be	(J-2) 2 Pa He; 630 eV	9 h	0-20
P2-2, Be	(J-2) 0.5 Pa Ar; 630 eV	4 h	0

The total reflectivity increased but the initial values were not reached especially in the UV-Vis range and is similar to the one of P1-1 after cleaning (see Figure 5.6). Oxidation of the Mo mirrors was measured in Basel by XPS (the oxide film is thicker than the typical escape length of photo-emitted electrons which is approx. 5 nm) and explains the low total reflectivity recovery in the UV-Vis range. The ion sputtering had two different effects depending on the process gas; for He the diffuse reflectivity increased by 1 % at most, whereas for Ar the diffusive component increased by 9 %. For mirror P1-1, coated with 300 nm of nanocrystalline Mo and exposed to Be in PISCES-B, almost all the Be was removed.

Mirror	Conditions (pressure in Pa)	Cleaning time	IBA, Be (10^{15} at./ cm^2)
P1-1, Be + D_2	2 Pa He; 630 eV	6 h 50	0-10

The total reflectivity increased significantly except for the UV-Vis range where the recovery was less pronounced (see Figure 5.6) due to oxidation of the mirror. The total reflectivity of 15 nm Mo oxide on a Mo substrate calculated with optical constants (n, k) from [85] fits well to the reflectivity of P1-1 after the cleaning. The diffusive component of the reflectivity increased by 1 % at most which is expected due to the nano-crystalline structure of the Mo surface. For P1-1 and P2-1 (see Figure 5.7 (a)) cleaned with He, the SEM images showed flat surfaces without any peculiar structures (except some remaining contaminants). On the opposite P2-2 displays a grain structure with clear evidence of selective sputtering of the various crystal orientations (polycrystalline Mo) as can be seen in Figure 5.7 (b). Roughness measurements performed on mirror P2-1 and P2-2 confirmed the visual impression with R_a equal to 15 and 47 nm respectively (R_a for pristine mirrors was approx. 10 nm).

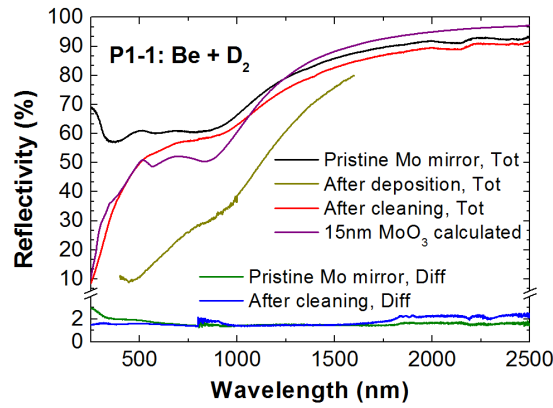


Figure 5.6: Total reflectivity and diffuse reflectivity of P1-1 as pristine mirror, after exposure to Be and after the cleaning in the Be chamber. The calculated total reflectivity of a Mo mirror with 15 nm of MoO_3 (with n,k from Palik [85]) are displayed with P1-1.

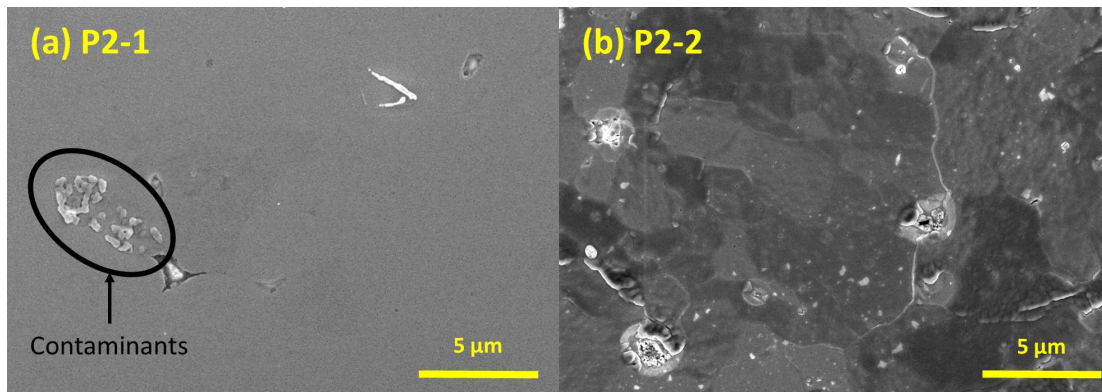


Figure 5.7: SEM images of mirror: (a) P2-1 after cleaning with He (J-1 + J-2) where remaining contaminants are surrounded in black and (b) P2-2 after cleaning with Ar (J-1 + J-2).

Comparing P1-1 and P2-1, both initially coated with 60 nm of Be and cleaned with He, the removal of contaminants from P1-1 seems faster. This is in conformance with the results obtained from IBA (see Table 5.3) where P1 deposits were found to be roughly a factor 4 less concentrated in Be than P2 deposits inducing a faster removal. For P2-1 and P2-2, respectively cleaned with He and Ar, the removal of contaminants should have taken approximatively the same time as we had similar erosion rates at 230 eV. However, cleaning with Ar appears to be much more effective as we do not have any Be residuals left on the surface after 4 hours. One explanation could be that part of the Be deposited on the mirror in the Be coater is slightly implanted within the Mo mirror due to the bias applied to it during the coating process. To fully remove the Be, one should remove not only the deposited film but also the implanted one. To do so, Mo has to be sputtered as well and in that particular case, Ar is much more effective than He. Thus the cleaning of P2-type mirrors is enhanced with Ar but as already stated before, due to the high sputtering yield on Mo, a strong increase of the diffuse reflectivity is observed if polycrystalline mirrors are used.

Cleaning at higher energies, R1, R2 and R3 coating

The 6 polycrystalline Mo mirrors coated in INFLPR with 30 nm thick deposits obtained with TVA technique were cleaned by using either He or He + Ar mixtures with various ion energies. To avoid a roughening of the mirror's surface, the ion energy of Ar ions was kept below 330 eV.

Mirror	Conditions (pressure in Pa)	Cleaning time	IBA, Be (10^{15} at./cm ²)
R1-1, Be + D ₂	1 Pa He + Ar (90/10); 330 eV	9 h 10	0
R1-2, Be + D ₂	2 Pa He; 330 eV	7 h	0-50
R2-1, Be + O ₂	1 Pa He + Ar (90/10); 330 eV	5 h	0
R2-2, Be + O ₂	2 Pa He; 630 eV	2 h 50	0
R3-1, Be + W + D ₂	2 Pa He; 630 eV	5 h 30	0
R3-2, Be + W + D ₂	1 Pa He + Ar (90/10); 330 eV	8 h 20	0-50

All the samples were nearly fully cleaned except R1-2 and R3-2 which still had traces of Be. No traces of W were detected on R3-1 and R3-2 although the use of He, which is an extremely positive result in the case of a He based in situ cleaning system for ITER. All the samples except R3-2 displayed a total reflectivity similar to the one of P1-1 after cleaning (see Figure 5.6) due to the oxidation of the Mo substrate. For R3-2 the total reflectivity (see Figure 5.8) is surprisingly high knowing that all the Be was not fully removed. This is because the Mo substrate is not as oxidized as for the other samples (7.5 nm Mo oxide for calculated reflectivity). The remaining BeO layer on the Mo mirror appears to have a protective influence on the metallic Mo reducing its oxidation.

For R1-1 and R2-1, the diffuse reflectivity underwent a small increase below 2 % in average. R3-2 exhibits a high diffuse reflectivity as can be seen in Figure 5.8 and originating from the remaining Be contaminants roughening the surface (they can be observed with SEM in Figure 5.9). This behaviour indicates the importance of a complete removal of contaminants for ITER FMs. The samples cleaned with He show following trends: (i) using He, even at 600 eV, does not damage the surface (no increase of the diffuse reflectivity for fully cleaned samples). R1-2, which still suffered from slight Be contamination, exhibited the same behaviour as R3-2 namely a high diffuse reflectivity in the UV-Vis range (up to 7 %).

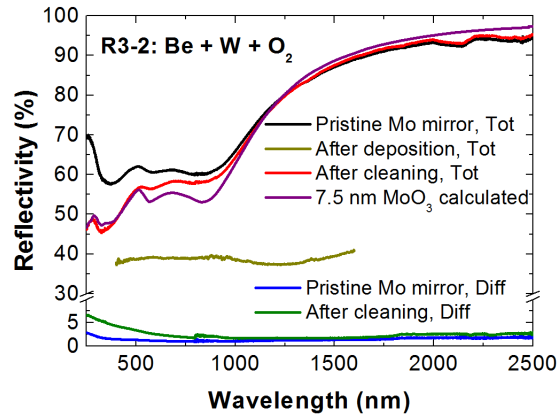


Figure 5.8: Total reflectivity and diffuse reflectivity of R3-2 as pristine mirror, after exposure to Be and after the cleaning in the Be chamber. The calculated total reflectivity of a Mo mirror with 7.5 nm of MoO₃ (with n,k from Palik [85]) are displayed with R3-2.

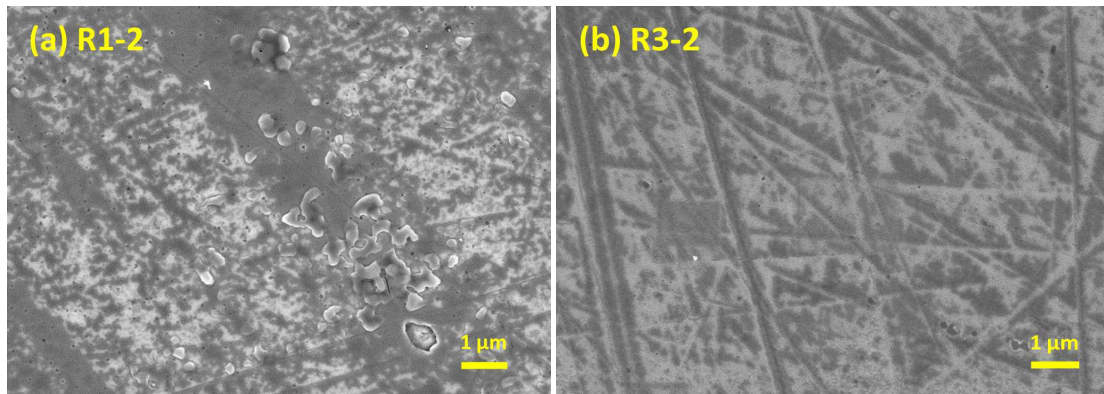


Figure 5.9: SEM images of mirror: (a) R1-2 after cleaning with He and (b) R3-2 after cleaning with He + Ar where Be contaminants are still present on the surface (contaminants are the light/whitish regions).

If we take a closer look to R1-1, R2-1 and R3-2, all cleaned with a mixture of Ar + He at 330 eV, one can observe that the film containing the highest amount of BeO needed less time to be removed. This is quite surprising as, according to Table 2.1, BeO is much harder to remove than Be metal. However, during the cleaning process, the whole Be present on the surface might become fully oxidized during the cleaning procedure. Similar effect is known to take place during reactive magnetron sputtering (target poisoning [40]). Hence the initial state of R1 and R2 should not be considered for the cleaning process but the reason for the faster cleaning of R2-1 is still not understood and additional investigations will be performed in a future campaign. For the samples cleaned with He it appears that mixed layer composed of Be and W (R3-1) are harder to etch away than pure Be layer (R2-2). As already stated, the Be-D co-deposited film from PISCES-B (P1, Be + D₂) was one the easiest film to sputter and is also supposed to be the closest to tokamak deposits.

To briefly resume, all types of contaminants could have been removed (in few cases, traces of Be were found). On an optical point of view, as can be seen in Table 5.5, the total reflectivity increased towards initial values but never to the full extent. When high Ar ion energies were employed for the cleaning or when contaminants remained on the surface, the diffuse reflectivity exceeded the initial value sometimes by up to 9 %.

Some mirrors free from Be contaminants but oxidized after the cleaning process in the JET-BeHF were cleaned in ESCA-1 facility to prove that optical properties could almost be restored to initial values. The oxidation of the Mo surface during the cleaning procedure could originate from the fact that: (i) due to limited availability of the BeHF, cleaned samples were directly removed from the vacuum, even if their temperature was not at room temperature. (ii) The vacuum chamber and gas lines were not leak tested because of safety constraints inherent to the JET-BeHF facility. Those two points are intrinsic to the system employed in this work. For ITER, a single cleaning step is expected to be sufficient to remove the contaminants while preserving the surface of FMs from oxidizing.

Cleaning in ESCA-1 facility

Samples R2-1, R2-2 and R3-1 were additionally plasma cleaned in Basel. Three different plasma conditions were used: either pure H₂, or a mixture of H₂ and Ar or pure He. As the chamber is connected in situ with the XPS chamber, the chemical state of the Mo surface was monitored to control the advancement of the cleaning process. Finally, ex situ reflectivity measurements were performed to confirm the end of cleaning.

Mirror	Conditions (pressure in Pa)	Cleaning time	Total R recovery (%)	
			400 nm	1600 nm
R3-1	(B-1) 1.5 Pa H ₂ ; 100 eV	4 h	48	86
	(B-2) 1.5 Pa H ₂ + Ar (50/50); 180 eV	4 h	98	94
R2-1	1.5 Pa H ₂ + Ar (50/50); 180 eV	5 h	100	97
R2-2	(B-1) 2 Pa He; 430 eV	10 h	81	61
	(B-2) 2 Pa He; 430 eV	7 h	104	83

The first trial was performed on R3-1 with H₂ where the idea was to reduce the oxidized Mo surface hence use chemical sputtering and not physical sputtering [106]. After the cleaning in the JET-BeHF and the few months needed to perform all the characterizations, the sample surface was almost fully covered with oxides (see Figure 5.10 (1)): 85 % of MoO₃ at 232.8 eV, 13 % of Mo₂O₅ at 231.5 eV and 2 % of Mo metal at 228 eV [107] inducing a low total reflectivity in the UV-Vis range as illustrated in Fig. 5.11. Exposing the sample to an H₂ plasma with 100 eV ion energy for 4 h, the MoO₃ was partially (33 %) reduced to MoO₂ as can be seen in Figure 5.10 (2) around 229.9 eV [107]. The main chemical state of Mo (66 %) is defined with a second peak localized around 228.3 eV and corresponding to a carbide (Mo₂C, [108]) According to Eren *et al.* in [73] this peak could also partially be attributed to molybdenum implanted with hydrogen: Mo-H (deuterium for [73]). An important reflectivity recovery was obtained in the UV-Vis range after this treatment but to fully remove the oxide, carbide and/or hydrogenated

Mo in a reasonable amount of time, Ar was incorporated in the process and the ion energy was increased to 180 eV. After 4 h exposure, the Mo was mainly in metallic form with smaller amounts of Mo₂C or Mo-H (see Figure 5.10 (3)). As the reflectivity was almost fully recovered, the cleaning was stopped even if all the Mo was not metallic. The two cleaning cycles performed with H₂ or mixed H₂ + Ar did not have an impact on the diffuse reflectivity.

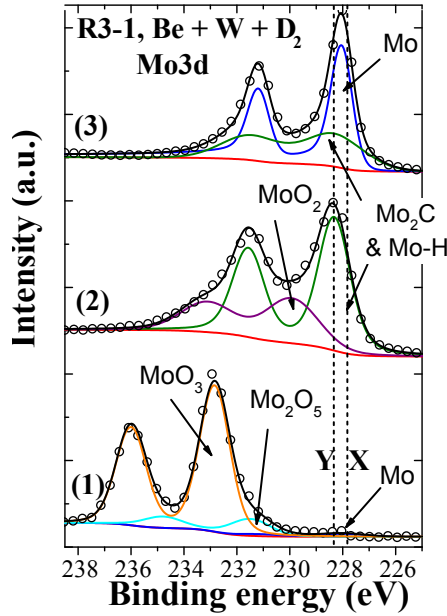


Figure 5.10: Mo3d core level spectra of sample R3-1 (1) before the cleaning in Basel, (2) after 4 h H₂ cleaning (B-1) and (3) after 4 h H₂ + Ar cleaning (B-2). The shown spectra are normalized for comparison. The open circles are the measured spectrum and the black lines correspond to the sum curve of all components represented in coloured lines. The vertical lines are given as eye guide for Mo metal at 227.8 eV (X) and Mo₂C & Mo-H at 228.3 eV (Y).

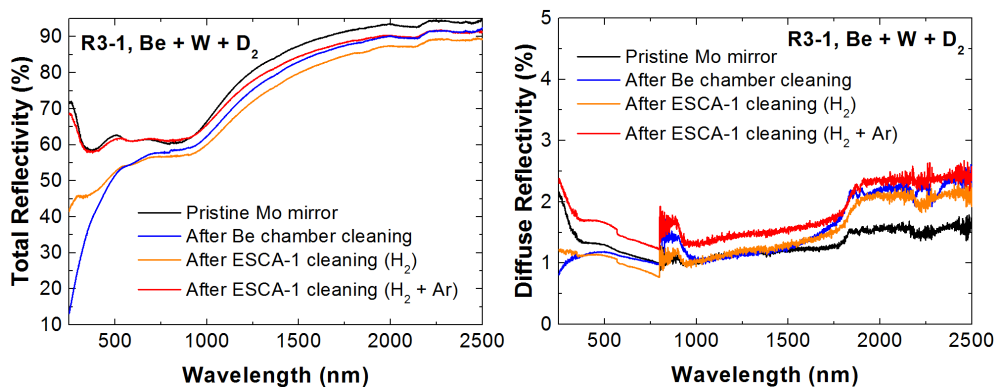


Figure 5.11: Total and diffuse reflectivity of R3-1 as pristine mirror, after cleaning in the Be chamber (J), after the first cleaning in Basel (B-1) and after the final cleaning in Basel (B-2).

Similar results were obtained for R2-1 cleaned with H₂ + Ar for 5 h. The was surface mainly composed of metallic Mo with some Mo₂C/Mo-H with a complete reflectivity recovery after cleaning.

Finally, as pure He was proven to efficiently remove Be and W deposits, FMs cleaning in ITER could be done using only this gas. Hence, removal of top oxidized Mo layer should also be

performed with pure He, tested in ESCA-1 facility on R2-2 (fully oxidized surface after cleaning in Be chamber). After 10 h of plasma exposure at 430 eV, the Mo was still oxidized but not anymore in a MoO_3 . The Mo3d core level spectra was fitted with two doublets, one at 229.2 eV, the second at 230.8 eV. The second signal at higher binding energies clearly corresponds to a MoO_2 state. The former peak could either originate from an unscreened state of MoO_2 [109] or from an oxide in an under stoichiometric state (MoO_x with $0 < x < 4$) [110]. Despite the fact that the Mo was not in a metallic state, the reduction of the oxide led to a non-negligible total reflectivity recovery in the UV-Vis range without increasing the diffuse reflectivity. An additional cleaning attempt was performed with He at 430 eV for 7 h and led to the full removal of the oxide Mo layer accompanied with a total reflectivity recovery. This cleaning trial with He establishes the possibility to use He for in situ cleaning procedures.

Summarizing the aforementioned results, 9 Mo mirrors contaminated with several types of deposits containing Be and W were cleaned in the Be chamber using RF plasma with He and/or Ar at different ion energies. For all the mirrors, the amount of contaminant was strongly reduced with some remaining traces of Be in few cases. He and Ar could both remove W containing deposits, while He was proven to offer a more gentle cleaning where the surface of the Mo mirror was preserved. The reflectivity was increased for all the samples although not fully recovered, especially in the UV-Vis range due to surface oxidation of the Mo mirrors as measured by XPS. Additional cleanings done in Basel proved that reflectivity could be fully recovered with either pure He or mixture of H_2 and Ar.

5.2 Tokamak deposits

So far, no experiments on plasma sputtering of real tokamak films containing Be have been performed, in contrary to laser cleaning [36, 111]. In parallel to the experiments above on laboratory Be and W deposits, 8 tokamak deposits grown in JET-ILW [27] on Mo and Rh-coated mirrors were plasma cleaned in the Be chamber (3.1.2), applying the same procedure as in section 5.1.3.

5.2.1 Mirrors in JET-ILW tokamak

The 8 mirror samples were $10 \times 10 \times 10 \text{ mm}^3$ cubes of polycrystalline Mo with one polished face. Among those 8 mirrors, 4 were coated with $1 \mu\text{m}$ of Rh at the University of Basel using magnetron sputtering [112]. The mirrors were exposed in JET-ILW in various locations of the tokamak including the divertor base (DB), the outer divertor (OD), inner divertor (ID) and the outer wall (OW) as illustrated in Figure 5.12 (a) and (b). The mirrors were fixed in so-called cassettes that were mounted in JET-ILW. Each mirror had its own channel and the distance of the mirrors in these channels could be varied. 0 cm corresponds to mirrors placed at the front end of channels (see Figure 5.12 (c) and (d)). That information is listed in Table 5.6 with characterizations of the deposits.

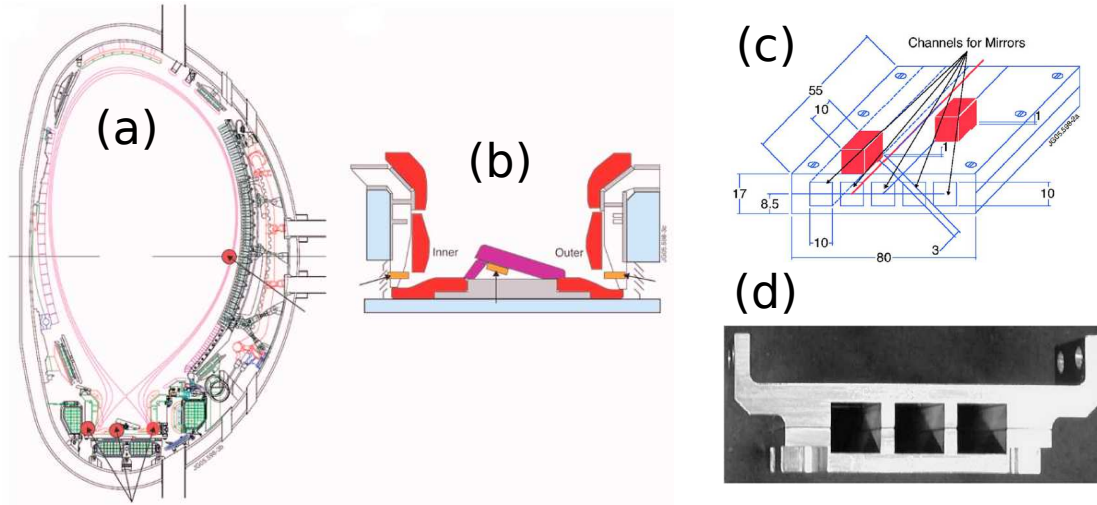


Figure 5.12: (a) and (b) Illustration of the location of mirrors in JET-ILW. (c) and (d) The mirrors were fixed in cassettes at various distance from the front end (position in the channel). Images are taken from [113].

Table 5.6: List of mirrors from JET-ILW and their location during exposure. NRA and ToF-ERDA characterisations were performed after exposure in JET-ILW and after cleaning in the Be chamber. Units are 10^{15} atoms per cm^2 . The equivalent Be thickness (in brackets) was calculated using the standard Be density of 1.848 g.cm^{-3} .

Mirror	Location	D	Be	C	N	O	Inc	W
61 Rh	OW 1.5 cm	0	94 (8 nm)	14	2.1	52	89	0
After cleaning	Be chamber	0	20 (2 nm)	4.5	0.6	8.9	20	0
69 Rh	ID 2.5 cm	180	710 (58 nm)	120	150	190	11	9.1
After cleaning	Be chamber	0	0.7 (< 1 nm)	5.6	0.9	4.1	4	0
77 Rh	OD 1.5 cm	520	5400 (437 nm)	51	130	590	57	0
After cleaning	Be chamber	130	460 (37 nm)	35	94	590	55	0
80 Rh	DB 0.0 cm	18	390 (32 nm)	87	22	420	20	33
After cleaning	Be chamber	0	2.2 (< 1 nm)	13	0.7	6.4	8.9	0
96 Mo	OW 0.0 cm	6	400.4 (32 nm)	44	4.4	100	3.8	0
After cleaning	Be chamber	1.4	86 (7 nm)	17	1	23	1.1	0
98 Mo	OW 1.5 cm	1.2	12 (1 nm)	38	1.6	17	2.8	0
After cleaning	Be chamber	0	0.1 (< 1 nm)	8.6	0.3	9.6	0.8	0
99 Mo	OW 3.0 cm	1.6	3.2 (< 1 nm)	32	1.2	11	2	0
After cleaning	Be chamber	0	0.3 (< 1 nm)	12	0.8	5.9	0.9	0
100 Mo	OW 4.5 cm	1.8	0.8 (< 1 nm)	30	0.8	5.4	1.6	0
After cleaning	Be chamber	0	0 (< 1 nm)	2.8	0.3	3.2	0.5	0

All the 4 Rh mirrors were heavily coated with typical JET elements (Be, inconels (Inc), N, C, O ...) and 77 Rh, close to a Be coater has the highest Be content of all. The inconels group denotes a sum of nickel, iron and chromium which cannot be separated. The mirrors optical properties were strongly degraded after the exposure as can be seen in [27] and Figure 1.10 with reflectivities well below those of Be from the handbook of Palik [85] (see 77 Rh in Figure 5.13). This confirms that even if material from the vessel can theoretically be highly reflective (Be, W), it will not necessarily be the case for the redeposited films. The 4 polycrystalline mirrors exposed in JET-ILW did not experience the same balance between deposition and erosion. As can be seen in table 5.6, 96 Mo suffered from high quantity of contaminants while mirror 98, 99 and 100 only had low deposition and probably experienced more erosion through plasma: the total reflectivity increased after plasma exposure compared to the reflectivity measured just before installation in JET-ILW probably due to the removal of the Mo surface oxide layer (see Figure 12 of [27]). Nevertheless, due to air storage for a few months between the retrieval of mirrors from JET and the plasma cleaning, the mirrors 98, 99 and 100 got oxidized again (see total reflectivity “After JET-ILW (J)” and “Before cleaning (J)”, Figure 5.15 (a)).

5.2.2 Cleaning in the Be chamber

All mirrors used in this study were characterized before and after the exposure in JET-ILW. The discharge conditions (gas, pressure, ion energy) can be found in Table 5.7 and were chosen accordingly to results of Be coated mirrors of the previous section.

Table 5.7: List of experimental conditions applied for each mirror in the Be chamber. When a gas mixture is used, the partial pressure ratio is expressed in brackets.

Mirror	Conditions (pressure in Pa)	Cleaning time	Total R recovery (%)	
			400 nm	1600 nm
61 Rh	0.5 Pa Ar; 230 eV	4h30	87.2	81.1
69 Rh	2 Pa He; 630 eV	15h	85.6	96.5
77 Rh	2 Pa He; 630 eV	7h	-3.8	-7.2
80 Rh	1 Pa He + Ar (90/10); 330 eV	11h	92.2	94.3
96 Mo	2 Pa He; 330 eV	6h30	67.6	45.5
98 Mo	2 Pa He; 630 eV	1h30	-91.1	44.1
99 Mo	2 Pa He; 230 eV	3h30	35.6	41.0
100 Mo	0.5 Pa Ar; 230 eV	1h30	22.1	97.5

Rhodium mirrors

During the etching process, deposits on mirror 61, 69 and 80 were reduced and for some entirely removed (see Table 5.6). Special attention has to be paid to W which was fully removed from mirror 69 and 80 by using either pure He at high energies (630 eV) or a mixture of He and Ar with lower energies (330 eV). The three previous mentioned mirrors exhibited similar post-cleaning behaviour: partial recovery of the total reflectivity, increase of the diffuse reflectivity (see example of 69 Rh in Figure 5.13) and metallic Rh surface after cleaning (measured by XPS). The diffuse reflectivity went from 1%, 2% and 2% to 7%, 11% and 17%, for 61, 69 and 80 Rh respectively. Based on those results, He and Ar at 340 eV damages mostly the mirror’s surface while Ar at 230 eV is the least harmful. Still, due to unknown damages during exposure in JET-ILW and different deposits and cleaning times, it is difficult to conclude on the most appropriate cleaning condition to use. For 77 Rh, the Be content decreased by more than 90 % although not fully removed due to lack of experimental time in the JET-BeHF. Because Be was still present the reflectivity did not change and did even slightly decrease.

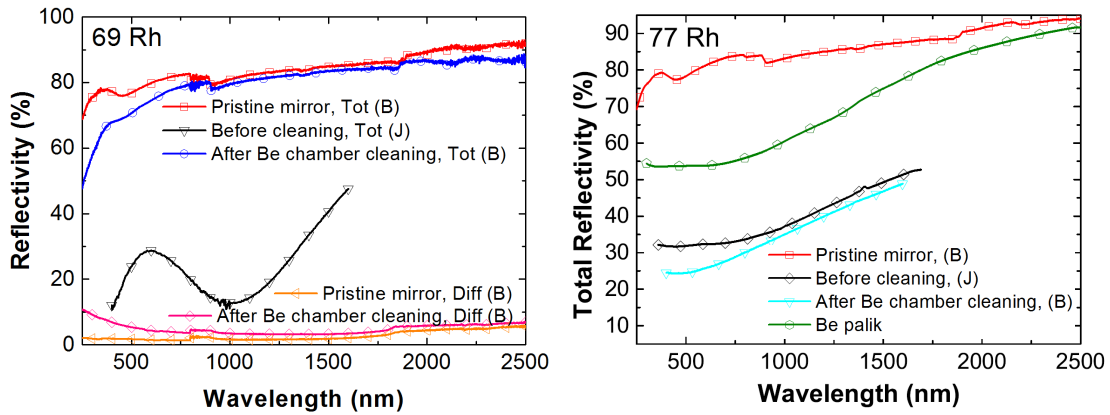


Figure 5.13: Total and diffuse reflectivity measured in JET (J) and/or Basel (B) before exposure in JET-ILW (denoted pristine mirror), after exposure in JET-ILW (before cleaning) and after cleaning in the Be chamber for mirror 69 and 77.

After cleaning in the Be chamber, Rh 77 exhibited buckling observed by SEM in Figure 5.14. EDX measurements performed on position A and B have shown that the dark grey surface is corresponding to the contaminants layer (mainly Be) while the light grey circles are Rh film. On the surface, the formation of bubbles of different sizes can be seen and for some of them the top layer is already delaminated. As SEM was not performed before the plasma cleaning, it is not known whether this phenomenon appeared during exposure in JET-ILW or during plasma treatment.

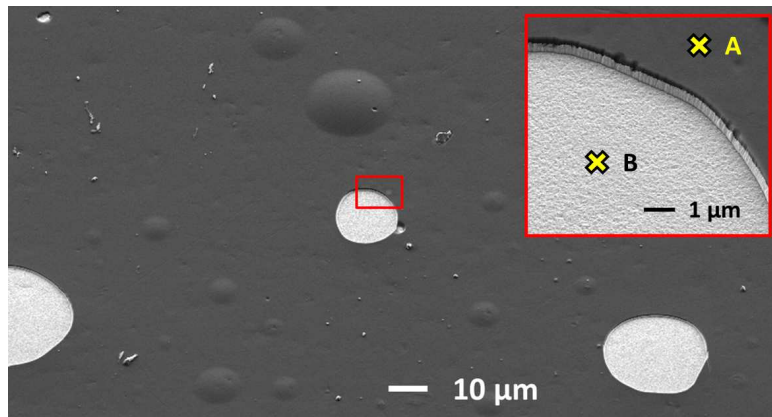


Figure 5.14: SEM image of mirror 77 after cleaning in the Be chamber with two different magnifications. EDX measurements were performed on point A and B.

Molybdenum mirrors

The contaminants were almost fully removed for 98, 99 and 100 Rh, and strongly decreased for mirror 96 as displayed in Table 5.6. Mirror 96 whose reflectivity was low after JET exposure experienced a consequent increase of its total reflectivity (see Table 5.7) while the diffuse reflectivity did not change. For mirror 98, 99 and 100, a small or non-existent increase in the total reflectivity was observed (see Figure 5.15 (a) by taking a closer look to the black curve “Before cleaning (J)” and the blue curve “After JET-BeHF cleaning (B)” while no increase was observed for the diffuse component (see Figure 5.15 (b)). As the contaminants were almost fully removed, the main explanation is the presence of an oxidized Mo surface: the reflectivity was

similar to calculated reflectivity of a Mo mirror oxidized over 15 nm and was confirmed by XPS measurements.

The cleaning of JET-ILW mirrors (Rh and Mo) deposited with Be, W and other tokamak impurities using RF plasma with He and/or Ar proved that this technique could significantly reduce the co-deposits thickness and improve the reflectivity in most of the cases. In contrary to Mo, Rh mirrors which are interesting for ITER due to their high initial reflectivity were fully metallic after cleaning and did not delaminate (except for mirror 77, where delamination was suspected to happen during JET exposure).

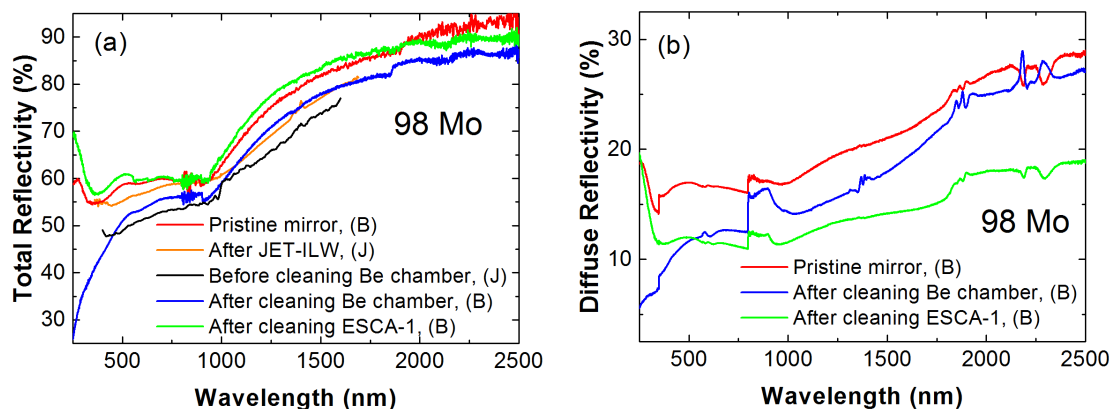


Figure 5.15: (a) Total reflectivity and (b) diffuse reflectivity measured in JET (J) and/or Basel (B) before exposure in JET-ILW (denoted pristine mirror), before and after cleaning in the Be chamber and after additional cleaning in ESCA-1.

Similarly to the samples coated with Be and W, some JET-ILW Mo mirrors were Be free but still oxidized and underwent a second cleaning in Basel in ESCA-1 facility (see Figure 5.15). More information can be found in our paper [8].

5.3 Summary

Regarding Al/W based laboratory deposits, porous morphologies could be obtained by mimicking ITER conditions. Also, dense and fully insulating films were produced either with ALD or reactive magnetron sputtering. Compact and flat alumina deposits were shown to be the hardest type of deposits to remove and were therefore chosen by ITER IO for further in situ plasma cleaning investigations (large size mirror and presence of B-field). Ar on the other hand was proven to be the best choice to remove Al-based deposits with approximately 230 eV ion energy. Lower ion energies would lead to low sputtering rates and induce too long cleaning time (experimentally verified), both for laboratory and ITER applications.

Cleaning experiments performed on Be and W (laboratory and JET-ILW deposits) were, to our knowledge, the first of their kind. The results indicate that He could be used as a process gas for ITER, even if contaminants are partially including W or if the Mo surface is oxidized (present on ITER FMs after air storage or in the case of steam ingress). For this specific campaign, a second cleaning step was mandatory in the present case due to oxidation of the Mo mirror in the vacuum chamber installed in the JET-BeHF but is not expected to be necessary for ITER due to the better vacuum conditions. Because the setup in the JET-BeHF lacked on characterization techniques, the cleaning was not always stopped at the right moment. For some samples, the removal was not complete while for others the surface of the mirror was already strongly sputtered, both cases leading to high diffuse reflectivities. The ideal case would correspond to strict removal of all contaminants (including oxidized Mo) with preservation of the mirror's surface.

A comparison between typical laboratory coatings and tokamak deposits can be performed looking at mirror 77 Rh. The cleaning of this specific mirror was performed with He at 630 eV, the same parameters as for P2-1, Be (J-2). For the JET-ILW mirror, contaminated with Be but also with typical tokamak species (deuterium, carbon, nitrogen, oxygen, Inconel components), the IBA analysis indicated a decrease of the Be content from 5400 to 460×10^{15} atoms per cm^2 in only 7 h of plasma treatment. This is more than 6 times faster than for P2-1. In section 5.1.2, porous Al/W based deposits (ITER-like) were found to be easier to sputter than compact Al_2O_3 films. Also, it was shown in section 5.1.3 that P1-type deposits (Be + D_2) produced in linear plasma device supposed to mimic ITER conditions, was the film that requested the less effort to be removed. The assumption that tokamak films are easier to sputter therefore seems confirmed by this additional cleaning campaign performed on JET-ILW deposits.

Plasma cleaning in ITER-like conditions

THIS chapter is devoted to cleaning results obtained in ITER-like conditions. Previous chapters demonstrated that in situ RF plasma cleaning of ITER-like contaminants was achievable in laboratory, working on small samples. The aim of this chapter is to prove that satisfactory results are not only observed in ordinary laboratory configurations but can also be obtained by increasing the size of mirrors towards real first mirror dimensions or in the presence of magnetic field similar to those expected in ITER. Investigations on the homogeneity of the etching process will be presented in section 6.1, from small mirrors up to real FM mock-ups. In section 6.2, results on the influence of a strong magnetic field (up to 3.5 T) on the cleaning properties will be presented. First quantitative hypotheses to explain the observed cleaning patterns will be given as well as first ever results of plasma cleaning in a tokamak (6.2.2). The implementation of in situ RF plasma cleaning in ITER is accompanied with some integration issues that should be solved. The third section 6.3 will thus be devoted to results obtained in the driven grounded electrode configuration, promoted by ITER Organization due to a simplified integration scheme. In diagnostic systems, a labyrinth made of mirrors is used and in the vicinity of the FM, there is a second one. We studied the cleaning of FMs but etched particles will go to the 2nd mirror. One possibility consists of running two discharge simultaneously. First trials were conducted in the B-field chamber and will be presented in section 6.4. To keep this chapter short, the results of the three last sections (6.2.2, 6.3 and 6.4) will be presented but will not be thoroughly developed.

6.1 Influence of size on the homogeneity

ITER optical diagnostics will rely on large FMs where the whole surface is used to extract the light towards the detectors. The aim of the following experiments was to verify that contaminants present on the surface of FMs could all be etched away, and, if possible, with homogeneous sputtering. Cleaning tests performed on small \varnothing 48 mm samples up to large mock-ups revealed the presence of strong edges effects while having a homogeneous sputtering process for the rest of the surface.

6.1.1 48 mm diameter mirror

Etching experiments were performed in the B-field chamber by setting the external magnetic field to zero. Although this chamber was initially designed to host 3 small mirrors (\varnothing 18 mm), new samples were produced to study erosion rates over the whole surface. They consist in larger polished Cu electrodes (\varnothing 48 mm), coated with approx. 200 nm of Mo using magnetron sputtering technique. The idea was to expose these samples to an RF discharge at 13.56 MHz and to measure how much Mo was etched away on several locations. The Mo thickness was

measured before and after cleaning using EDX analysis fitted with STRATAGem software (see section 3.2.2) and erosion rates can be calculated on different locations.

As experiments were performed in the B-field chamber, the side and backside of the electrode are fully shielded and the front side, where the electrode is normally at the same level than the shielding, is free. A cut of the electrode and shielding system is schematized in Figure 6.1. Typically in industry or laboratory, the RF power is applied to an electrode, larger than the sample to be plasma treated, on which the sample is mounted. By doing so, one can neglect edge effects on the sample. In our case, the whole electrode is the sample, as it will be in ITER. A representation of electric field lines were therefore added to the scheme for the aforementioned configurations but also for a specific case tested and presented after that where the electrode is raised compared to the shielding. From this schematic, one could assume the presence of edge effects for both configurations leading to higher ion fluxes on the perimeter as shown for example in [114].

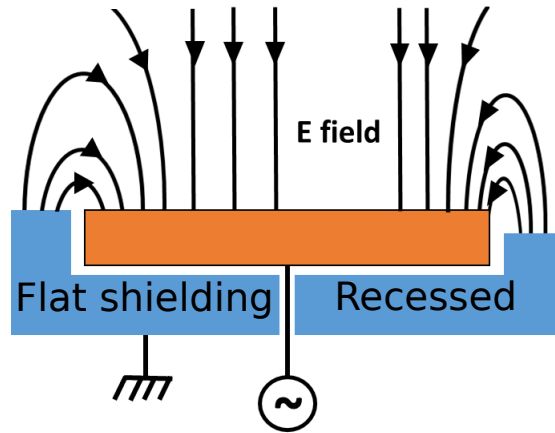


Figure 6.1: Schematic of the electric field distribution when the electrode is at the same level than the shielding (left part) and when the electrode is above the shielding (right part).

The first cleaning test with flat shielding was performed with Ar at 1.7 Pa as process gas, 13.56 MHz excitation frequency with 8 W RF power. These conditions led to a self-bias of -200 V and the discharge was sustained for ten hours to etch sufficient Mo away for analysis. The evolution of the Mo coated Cu sample with cleaning is depicted in Figure 6.2. A visual image taken after cleaning as well as Mo thickness measurements performed over one line (sufficient due to the axial symmetry of the discharge) exhibit the properties of the etching over the surface. Before starting the evaluation of the results, it is worth mentioning that narrow EDX scans were performed on one edge to increase the spatial resolution (the number of points was increased and the measurement area is narrowed down). This allowed resolving the edge effect between position 1 and 3 (not done for the other side, e.g. position 8 to 10).

Starting with the visual inspection, an orange ring is clearly visible on the edge of the sample indicating the presence of Cu on the surface, i.e. the removal of the Mo film in this region. This observation is consistent with the presence of edge effects introduced earlier and was corroborated with EDX measurements (no remaining Mo around position 1 and 10). In addition to the edge effect, a black ring appeared on the outer edge as shown in the inset. This ring corresponds to a so-called redeposition region, where some sputtered Mo from central region is redeposited, leading to this black appearance. This phenomenon was also observed in EDX analysis, a narrow scan of edge regions revealed a Mo amount equivalent to 180 nm, more than the initial thickness. Finally, the thickness measurements display an homogeneous Mo removal in the central region, approx. over 22 mm. Such inhomogeneous behaviour with presence of edge effects was never observed in previous chapters as samples were always smaller than the

6.1. Influence of size on the homogeneity

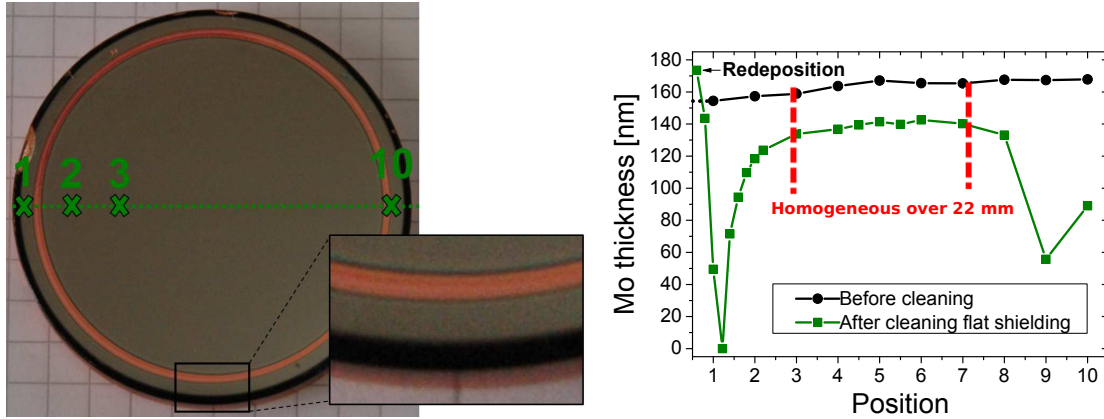


Figure 6.2: Image after cleaning and erosion profile of plasma cleaned sample where the grounded shielding was on the same level than the electrode.

driven electrode on which they were mounted.

As explained before, FMs installed in ITER should be able to collect as much light as possible, and thus a homogeneous cleaning should be present on the largest possible surface. Therefore, a new design was tested in the B-field chamber, where the electrode is slightly moved forward by the thickness of the electrode, e.g. 5.8 mm. The aforementioned discharge conditions were reproduced while the RF power had to be raised to 16 W to achieve the same self-bias due to the modified geometry. EDX measurements performed before and after plasma cleaning permitted the estimation of erosion rates in function of the position over one line, shown in Figure 6.3. They are displayed with the erosion rate of the previous sample, with flat shielding.

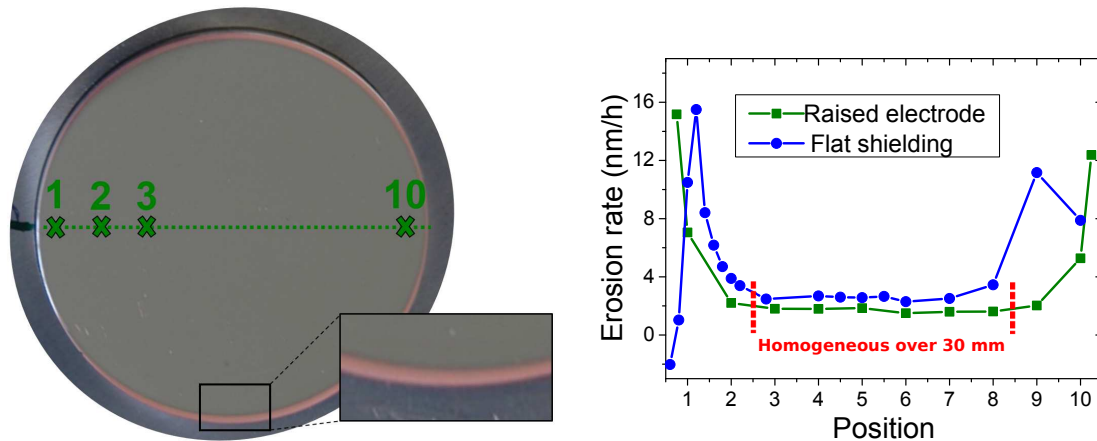


Figure 6.3: Image after cleaning and erosion profile of plasma cleaned sample where the grounded shielding was pulled back compared to the electrode.

Visually, the presence of edge effects can be seen, but now localized directly on the edge and without a noticeable redeposition region. The same behaviour is also observed on the erosion rates profile. Compared to the cleaning done with the flat shielding, the motion of edge effects towards the perimeter of the sample provides a homogeneous cleaning over 30 mm. Regarding the erosion rates in the center of the samples, they are equal to 2.5 nm/h for the flat shielding and slightly smaller for the raised electrode case (1.8 nm/h) probably due to the lower confinement of the discharge for the raised electrode geometry with its non-shielded edges.

Two different geometries were tested for etching properties. In both cases, the central region was sputtered homogeneously and edges effects were present. When the electrode was raised

compared to the shielding, the edge effects moved towards the perimeter of the sample leading to an increased area with constant erosion rate but were not suppressed. For ITER, those observations suggest that a sacrificial area of 1 cm is necessary for FMs. Although the central region of \varnothing 48 mm samples exhibited a homogeneous cleaning, further experiments mimicking real ITER FMs size will be presented in the following sections.

6.1.2 98 mm diameter mirror

An intermediate experiment between the aforementioned \varnothing 48 mm electrodes and real FMs size was performed on a \varnothing 98 mm polycrystalline Mo mirror coated with 260 nm thick porous Al/Al_{oxide} deposits as described in section 5.1. The cleaning cycles were performed with Ar at 0.5 Pa and with 13.56 MHz excitation frequency and self-biases of -200 V for 62 h followed by -350 V for 72 h. The complete results of this experiment are available in [6] and were chronologically performed before the experiments above and the acquisition of STRATAGem software. To briefly summarize, the etching was characterized by the presence of edge effects leading to a faster erosion on the perimeter of the mirror, but a homogeneous sputtering process was observed for the central region (80 mm over 98 mm). Due to the polycrystallinity of the mirror and relatively high Ar⁺ energies employed, the diffuse reflectivity of the mirror after cleaning reached values up to 50 % at $\lambda = 250$ nm. Compared to cleaning experiments performed in section 5.1.2 with similar deposits and slightly lower Ar ion energies, the present cleaning was much slower (0.03 compared to 0.56 nm/h). According to Table 5.2, the deposits should have been removed in approx. 8 h but more than 130 h were requested. This phenomenon is probably because the sample was removed from the vacuum chamber between each operation for EDX analysis, causing the full oxidation of the porous aluminium structure and shifting the sputter rate towards values measured for fully insulating dense alumina coatings (factor 12 in sputtering yield, see Table 2.1).

As the cleaning on \varnothing 98 mm mirror showed promising results, a last experiment was performed on a larger sample and will be discussed in the subsequent section.

6.1.3 Edge Thomson scattering mirror mock-up

In this section, plasma cleaning on a real size ITER FM, namely the ETS FM which is 200×300 mm², was simulated on a mock-up with similar dimensions. To combine large size of electrode with proper analysis of the sputtering process with EDX, XPS or spectrophotometry which are usually performed on small sample (typically 1–2 centimetres), experiments were based on 200×300 mm² metallic plates, in which mirrors insets for characterizations (up to 5) are embedded. To cover a wide range of scenario, three different plates were machined: a conductive SS one, an insulating Al anodized one (50 μ m of Al₂O₃ on the surface) and finally a half insulating/half conducting plate (Al metal in the middle and 50 μ m of Al₂O₃ on the edge). The picture of the ETS mock-up as well as a sketch of the half anodized mock-up are shown in Figure 6.4. The sputtering homogeneity and effectiveness were investigated with Mo mirrors coated with 25 nm of dense Al₂O₃ and inserted in each plate. Before alumina deposition, each inset was coated with 300 nm NiMo with magnetron sputtering. As discussed in section 4.2.4, almost constant ion flux and plasma potential over the surface of the mock-up (slight decrease towards the edges) were measured with Langmuir probe.

Experiments were performed in ESCA-1 sputter chamber where the ETS mock-up was placed in the middle of the chamber. Like previous experiments conducted in this chamber, 13.56 MHz was used as excitation frequency with Ar as a process gas at 0.5 Pa and a self-bias of -200 V. As EDX analysis were done before the procurement of STRATAGem software, the advancement of etching was quantified with the amount of Al measured compared to Mo. The SEM accelerating voltage was kept at 10 kV and, for example, 25 nm Al₂O₃ on a Mo mirror corresponds to 12 and 88 % of Al and Mo respectively. The quantification limit for EDX analysis is approx. 1 % and the final cleaning state, e.g. when Al(%) was below 2 %, was therefore characterized with XPS.

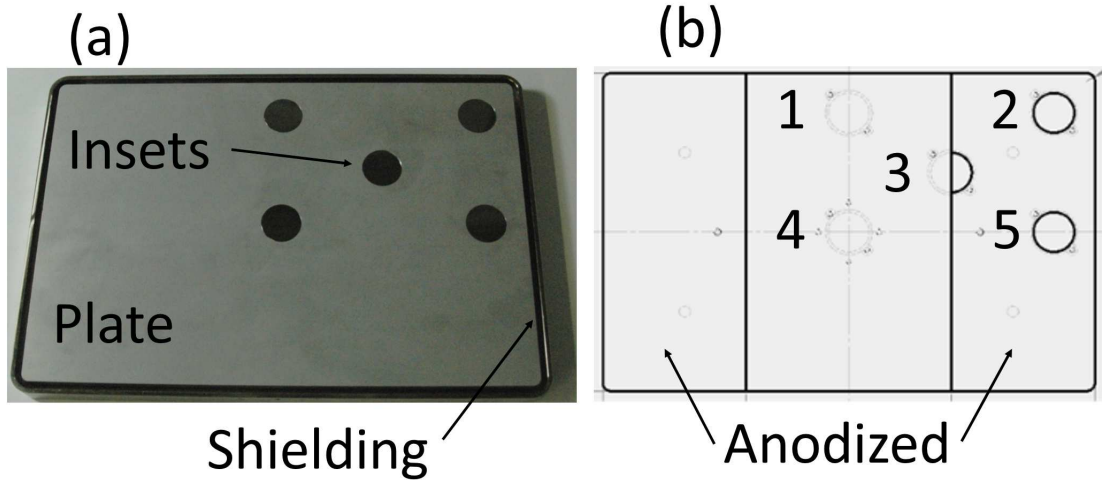


Figure 6.4: Picture of ITER's edge Thomson Scattering mirror mock-up where the plate is either SS or Al anodized. 5 Mo mirrors can be inserted. (b) Schematic of the half anodized aluminium plate with insets location.

Although three different experiments were performed, the focus is set on the results obtained with the SS (conducting) ETS mock-up. As already observed on numerous occasions, the Al_2O_3 coating strongly reduced the reflectivity of the Mo insets, especially in the visible range (Figure 6.5). The first cleaning lasted 6 h and revealed an insufficient cleaning time (EDX analysis, Figure 6.5). After 10 h additional etching, the Al_2O_3 contaminants were removed from samples # 1 to 5 with traces of Al still present on sample # 2, located on the edge. The optical properties of all mirrors are similar to the one shown in Figure 6.5 corresponding to sample # 3 except for sample # 2, still contaminated with some Al as confirmed with XPS measurements. No sample displayed noticeable diffuse reflectivity increase. The sputtering is nearly homogeneous from the center towards the edge and confirms the measurements performed with the Langmuir probe and conducted along the ETS mock-up. As the insets are located at a minimal distance of 25 mm from the perimeter of the electrode, no edge effects were observed. On the overall, a homogeneous cleaning over the conducting ETS mock-up with slightly smaller etching rate on the edge was confirmed.

Two more cleaning experiments were performed with a fully anodized Al ETS mock-up (insulating) and with a half-anodized one with the same conditions as described above. Compared to the SS ETS mock-up, those two experiments displayed similar trends: 16 h to remove the 25 nm of Al_2O_3 , recovery of the optical properties and finally slightly slower etching in the edge. Even for the half-anodized ETS mock-up, the etching properties on insets # 2, 3 and 4, surrounded by surfaces having different dielectric properties, were identical. These results confirm the universality of RF in situ plasma cleaning and are particularly relevant for ITER as it is not yet known whether deposits will be oxidized or not and if they will have the same dielectric properties over the surface. Still, based on the results above, one could assume that the whole surface of FMs will be etched homogeneously (omitting edge effects), even for mirrors as large as the ones designed for the ETS diagnostic or deposits having distinctive dielectric properties.

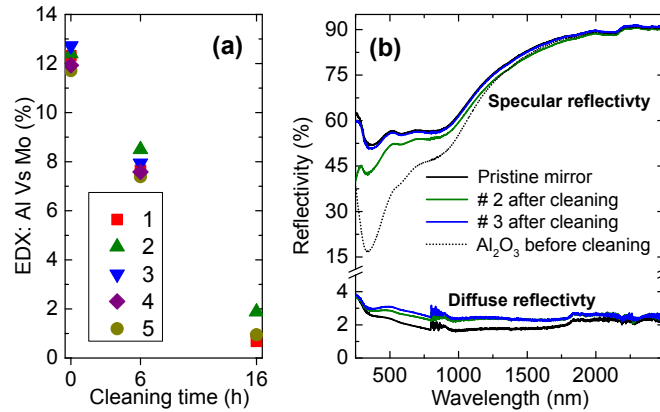


Figure 6.5: Ratio of EDX measurements for Al and Mo content as a function of cleaning cycle. Specular and diffuse reflectivity of mirrors cleaned in laboratory on the conducting ETS mock-up. For comparison, the reflectivity of the pristine and the nanocrystalline Mo deposited with 25 nm Al₂O₃ was plotted.

6.2 Plasma cleaning in the presence of a B-field

In ITER, simulations cannot predict the exact amount of deposits that will build up on each FM in a certain time. Ideally, in situ RF plasma cleaning should therefore be functional at all time, even if the magnetic field (at 3.5 T) is still on. The aim of the subsequent experiments in magnetic field was to come as close as possible to the real situation in ITER and to investigate the impact and homogeneity of sputtering under such condition. Before starting plasma etching experiments in high B-field (up to 3.5 T), first experiments were carried out in a magnetic field environment at the SULTAN facility [115] in EPFL-SPC Villigen, taking advantage of the residual magnetic field outside of SULTAN and equal to 0.35 T. SS mirrors, coated with 300 nm NcMo and dense Al₂O₃ were etched in the Be chamber (used there before its installation in the JET-BeHF) with different angles between the surface of the mirror and the magnetic field (0, 45 and 90°). Results of this study are accessible in our paper [6] and can be summarized as follow:

- It was possible to run an Ar discharge at 0.35 T for all configurations.
- Al₂O₃ films were removed from the Mo mirrors for all orientations of the B-field.
- A recovery of the reflectivity was observed but never to a full extent, mainly due to oxidation of the mirror.
- The cleaning performance seemed to be enhanced when the field lines are parallel to the mirror surface ($\alpha = 90^\circ$).

The promising results obtained in Villigen led to the design of the B-field chamber for new tests in Lausanne at higher B-field, mimicking actual field expected in ITER. All subsequent experiments were performed in the B-field chamber with capacitively coupled plasma using 13.56 MHz excitation frequency and Ar as a process gas. The RF power was set in order to obtain -200 V self-bias.

6.2.1 Cleaning in the B-field chamber

6.2.1.1 Preliminary results

First experiments in the B-field chamber were performed with 3 small mirrors used as insets as shown in Figure 3.4. The mirrors were SS substrate, coated with 300 nm of nanocrystalline Mo and 25 nm of dense Al₂O₃. The angle α is defined between the magnetic field lines and the

6.2. Plasma cleaning in the presence of a B-field

mirror surface normal as shown for example in Figure 6.6. Cleanings performed for $0^\circ < \alpha < 45^\circ$ exhibited a removal of the contaminant deposit accompanied by a recovery of optical properties (and no increase of diffusive component). When the B-field became more oblique to the surface, the situation changed displaying inhomogeneous sputtering and for parallel B field, region of strong etching and others dominated by redeposition were found as displayed in Figure 6.6. Also, while typical RF power between 10 and 20 W was requested to obtain -200 V bias for $0^\circ < \alpha < 85^\circ$, parallel B field led to a strong enhancement of the required RF power up to 300 W to reach the same self-bias.

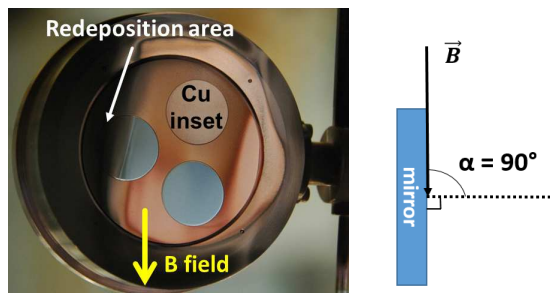


Figure 6.6: Picture of the electrode after etching at $\alpha = 90^\circ$ for 7 h. Two mirrors were embedded in the Cu electrode for characterization. A large area with net redeposition (black) is observed on the left of the electrode.

Using small mirrors inset, the characterization of the etching properties of the whole electrode is clearly incomplete as the sputtering is no longer homogeneous over the surface. Also, as cleaning was shown to be extremely inhomogeneous at parallel B field ($\alpha = 90^\circ$) with net redeposition area and problems to reach -200 V self-bias, the minimum angle for oblique fields was set to 85° in the subsequent experiments as well as for ITER diagnostic FMs.

6.2.1.2 Description new experimental campaign

A new experimental campaign was developed, where the whole sputtered electrode is analysed, as in section 6.1.1, by using thickness estimation with STRATAGem software (3.2.2). Cu electrodes coated with Mo were thus exposed to a magnetized plasma (3.5 T) and the Mo thickness was quantified before and after the erosion to estimate erosion rates with EDX analysis. The erosion rates profiles that will be shown subsequently were systematically obtained from samples where Mo was still present over the whole surface after the cleaning (the exposure time was set accordingly). In some cases, pictures of over-exposed samples will be added for visual information but one as to keep in mind that the etching profiles were performed on not completely etched Mo coatings. Two parameters are defined to characterize the etching with B-field:

1. R_{\neq} which represents the inhomogeneity due to the presence of the magnetic field and is the ratio between the highest and lowest erosion rates recorded on one sample.
2. $R_{B/no\ B}$, the ratio between the mean erosion rates measured for a given configuration with and without magnetic field. This value gives the speed increase in sputtering due to the presence of the B-field.

6.2.1.3 Perpendicular angle to the surface, $\alpha = 0^\circ$

The first cleaning attempt was done with the magnetic field normal to the surface of the electrode. During the discharge, a bright beam, stable in time, was observed in the central part of the plasma column where both ends were respectively located in the middle of the electrode and the center of the top cover of the vacuum chamber. A picture of this phenomenon is shown in Figure 6.7 and was clearly observed up to $\alpha = 45^\circ$. In magnetized plasmas, such regions of

enhanced light intensity are denominated as filaments and typically indicate strong changes in plasma parameters like charged particles density for example. Formation of filaments in strongly magnetized low-pressure RF plasma discharge was reported in very few publications in the field of complex dusty plasma [116–118]. In those studies, the magnetic field was going up to 2.3 T and was systematically oriented perpendicularly to the electrodes as in our experiment. The mechanism behind the formation of filaments is not clearly defined although Schwabe et al. [117] proposed an explanation based on density fluctuations that can no longer be balanced by the plasma due to the restricted transport of charged particles across the magnetic field lines and leading to region with enhanced ion densities. Visually, only one single filament was discerned in our experiment while other publications reported the presence of several filaments throughout the plasma column. The fact that we only observe one filament could originate from the localisation of the top cover slightly outside from the magnet. Recalling Figure 3.4 (d), the magnetic field is divergent outside of the solenoid. As the motion of electrons and ions is following the B-field lines that open outside of the magnet, the power emitted in the center of the electrode is less “spread” than on the edges, hence the power/volume ratio is larger in the central part of the plasma column. Additional tests should be performed with the grounded electrode being contained in the solenoid to confirm the above-mentioned theory. Erosion profiles performed on the horizontal, vertical and diagonals of the sample (see Figure 3.7) exhibited the same profile and the etching is thus perfectly symmetric around the center. Those profiles were averaged and are displayed in Figure 6.7.

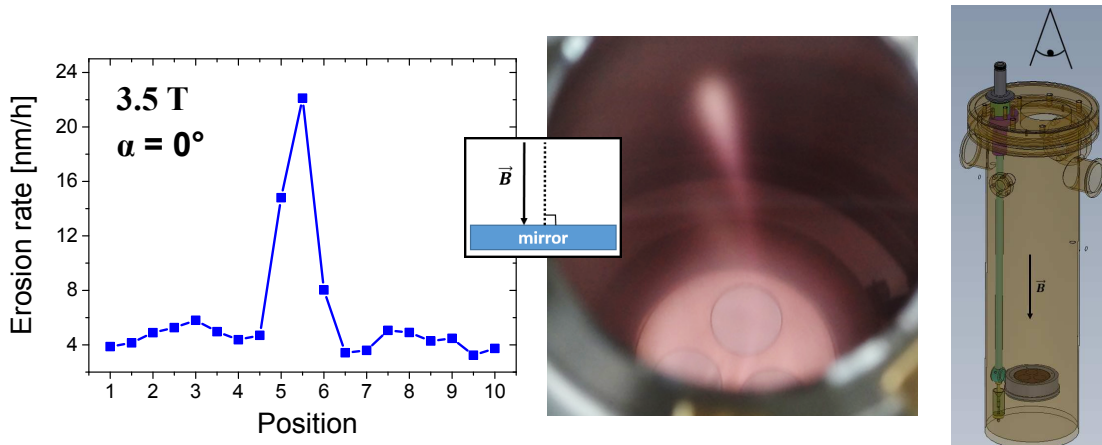


Figure 6.7: Erosion profile at 3.5 T and $\alpha = 0^\circ$. The data represent the average of 4 profile lines (horizontal, vertical and diagonal axis) that exhibited similar results. Picture of the discharge with the visible and stable filamentation going from the electrode center towards the top grounded cover and the angle of view for the picture is shown on the right. The low resolution is due to the magnetic field perturbing the camera.

Compared to experiments performed without B-field, three main effects are observed:

1. Absence of edge effects, attributed to the suppression of cross B-field transport.
2. Homogeneous sputtering over the surface except in the central part of the electrode with increased etching rates and $R_{\neq} = 7$.
3. The mean sputtering rate was increased with B-field and $R_{B/no B} = 3$.

A similar experiment was performed by Razdobarin *et al.* in [42] with an axial magnetic field of 0.05 T where suppression of edge effects as well as an increased erosion in the centre of the electrode was observed. They attributed the enhanced central erosion to redeposition coming from the grounded counter-electrode as the electrode gap was only 2 cm. In our test, the gap is set to 38 cm and the main reason for increased sputtering is allocated to the enhanced ion

density related to the strong filamentation observed visually. Still, the reason for the formation of filaments is not clear and the development of a procedure to reduce their effect on etching should be investigated further.

6.2.1.4 Oblique angle to the surface, $\alpha = 70^\circ$ and 85°

To cover the wide range of FMs configurations present in ITER, the electrode was tilted within the chamber to obtain more tangent magnetic field to the surface. In the subsequent experiments, α was varied from 70° to 85° with specific focus given on the most oblique case. Two erosion profile lines were systematically performed in horizontal and vertical directions to cover the asymmetric properties of the sputtering. In some cases, the orientation of the B-field was inverted. The “normal” mode consists of the B-field pointing downwards (as for the perpendicular experiment above) and is denoted by $+3.5$ T (see Figure 6.8 (a)) while -3.5 T is associated with an upward orientation.

The first results introduced correspond to cleaning performed with $\alpha = 85^\circ$ at upward or downward B-field. As previously stated in section 4.2.6, working with oblique B-field angles lead to a decrease of the self-bias for a constant RF power and thus, the power was almost tripled (21 instead of 8 W) to achieve -200 V self-bias. The main effects observed for etching in this configuration were:

1. Absence of edge effects.
2. Inhomogeneous sputtering over the surface with $R_{\neq} = 14$.
3. Increase of the mean sputtering rate with B-field and $R_{B/no\ B} > 200$.

Regarding the plasma discharge itself, no filamentation was observed neither in this configuration nor at $\alpha = 70^\circ$. On the erosion profiles presented in Figure 6.8, two main drift directions were observed, one along the horizontal direction, one along the vertical direction. The superposition of those two drifts led to the formation of a pattern which appears to resemble a yin-yang (see Figure 6.8 (a)). Taking a closer look to the horizontal positions for $+3.5$ T (resp. -3.5 T), a stronger etching appears on the right (left) part of the sample. The E-field is perpendicular to the surface and directed into the sample, and the $\mathbf{E} \times \mathbf{B}$ direction is depicted in Figure 6.8 for both magnetic configurations. Several studies conducted in magnetically enhanced reactive ion etching or RF capacitive coupled discharges with transverse B-field systematically exhibited an increased ion density and etching in the $\mathbf{E} \times \mathbf{B}$ direction [101, 119–123] although done at much lower B-field (maximum 20 mT). Surprisingly, in our experiments, the erosion rates followed the opposite direction of the $\mathbf{E} \times \mathbf{B}$ drift. The erosion rates that are measured represent the net erosion (the difference in thickness before and after etching), not to confound with gross erosion (total thickness removed from the surface). In fact, it was shown that a given amount of the total eroded material (gross erosion) could be redeposited on the surface and hence decrease the net erosion locally in the presence of grazing and strong B-fields (> 2 T) [124–126]. The driving effect of this phenomenon is the ionization of the sputtered Mo atoms within the MPS region and the E-field, directed towards the sample, can easily reattract the charged particles towards the surface. In experiments and simulations performed by Ding *et al.* in [125], the amount of redeposited Mo was found to be up to 67 % for an \mathbf{E} field of approx. 90 V and the location of the redeposition region is especially relevant for our work as it was found to be in the $\mathbf{E} \times \mathbf{B}$ direction. Hence, coming back to our experiments, more sputtering could effectively occur in the $\mathbf{E} \times \mathbf{B}$ direction, but nonetheless, due to redeposition, the inverse effect is seen in the net erosion displayed in Figure 6.8. Simulations of our experiments are still ongoing and will hopefully confirm the assumptions made earlier.

A second drift was observed in the vertical direction with much more erosion on the top of the sample for both upward and downward magnetic field configurations. The reason for this behaviour remains unclear although two hypotheses can be suggested. The first one is based on the difference in connection length between the top and bottom location of the electrode and the top grounded wall. The minimum, mean and maximum distance between the electrode

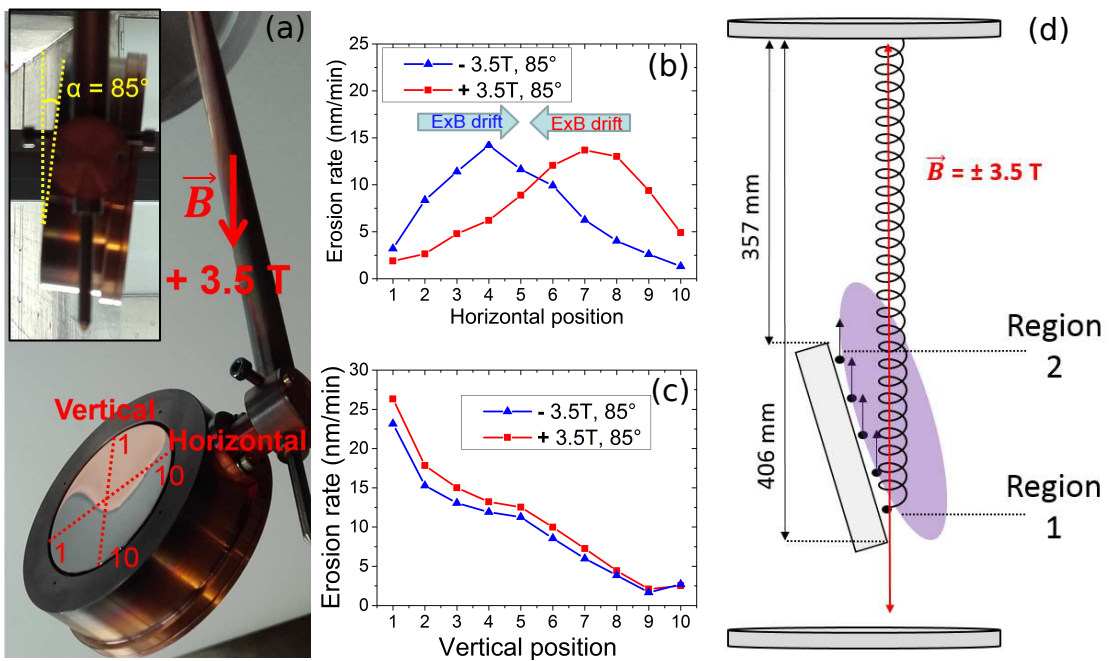


Figure 6.8: (a) Picture of sample exposed to plasma for 20 min at + 3.5 T and $\alpha = 85^\circ$. Location of the horizontal and vertical profile lines as well as the position of the two end measurements points (1 and 10) were added to the illustration. (b) Horizontal and (c) vertical erosion profile at $\pm 3.5\text{ T}$, $\alpha = 85^\circ$. (d) Schematic of electron motion for positive oblique angles. Region 1 (resp.2) corresponds to a low (resp. high) density region. The maximum and minimum distance between driven electrode and grounded top cover are given.

and the top grounded wall is respectively 357, 381 and 406 mm. The RF power emitted at the bottom of the electrode is therefore “used” over a larger distance leading to lower densities in this location and thus, to smaller erosion rates. The second hypothesis resides in an increase of the ion density in the top region of the sample due to the charged particles motion and is illustrated in Figure 6.8. Due to the strong B-field confinement, charged particles have a motion parallel to the magnetic field as they move from the electrode towards the grounded counter-electrode. In region 1, only electrons created in the bottom region will flow while for region 2, as all electrons move upward towards the counter-electrode, the electron flow is higher in this region. Hence, region 2 has a larger electron density and as electron-neutral collision is the main mechanism for ion production, region 2 possesses a larger ion density. Consecutively, more ions are available in region 2 for sputtering, leading to enhanced erosion rates. The two hypotheses just described would both lead to the same observation, namely an increased etching on the top of the electrode. By having a counter-electrode with the same tilt as the driven electrode, the ground to electrode distance would be the same for all locations on the sample and one could check the validity of the first hypothesis.

To confirm the hypotheses regarding drift in the horizontal and especially in the vertical direction, an additional experiment was performed by placing the sample at $\alpha = -85^\circ$ with $B = +3.5$ T. This configuration is similar to $\alpha = 85^\circ$ with $B = -3.5$ T rotated by 180° that was added in Figure 6.9 for comparison. Horizontal and vertical erosion profiles are shown in Figure 6.9 and display similar trends as discussed above.

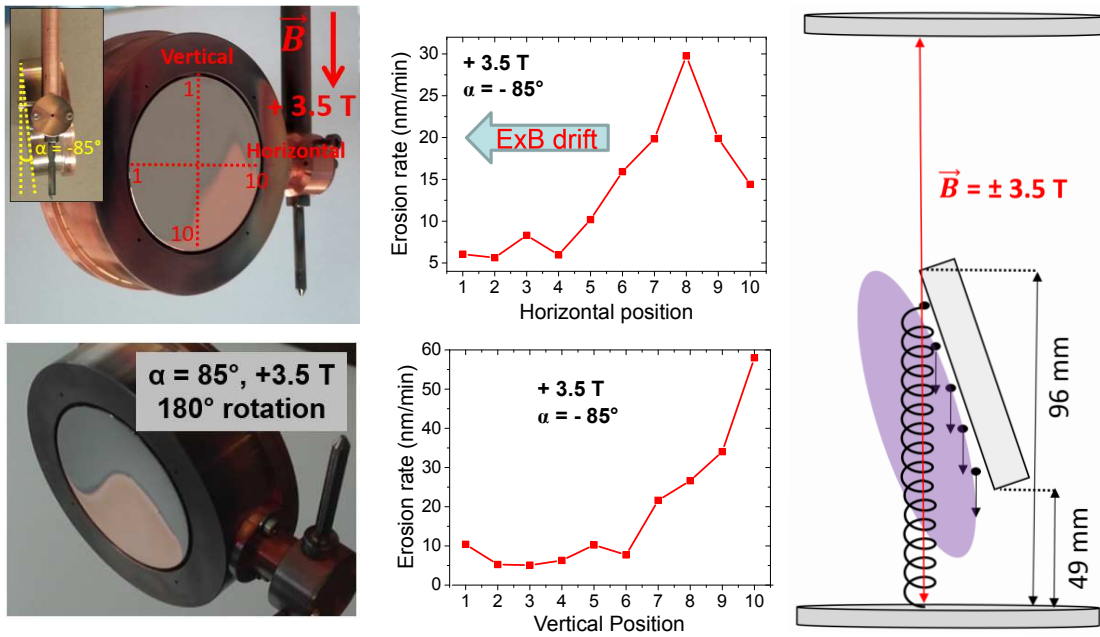


Figure 6.9: Horizontal and vertical erosion profile at $+3.5$ T, $\alpha = -85^\circ$. The configuration with $\alpha = 85^\circ$ and $B = -3.5$ T, rotated by 180° , was added for comparison.

Horizontally, the erosion is again larger in the opposite direction of the $\mathbf{E} \times \mathbf{B}$ drift. Vertically, the sample appears to be more eroded on the bottom which is the exact opposite as before but taking the location of the grounded counter-electrode in consideration, the same behaviour is observed, namely that a higher erosion rate is observed on region closer to the grounded electrode. The two hypotheses that were made before are valid in this particular configuration as:

1. For the connection length, the bottom, resp. top region is at 49, resp. 96 mm from the grounded electrode, e.g. the RF power emitted at the top region of the electrode is therefore “used” over a larger distance leading to smaller erosion rates.

2. The electrons now flow towards the bottom of the vacuum chamber and the bottom regions of the plasma have an increased electron stream across them, leading to larger ion densities and erosion rates.

Finally, two supplementary tests were conducted at $\alpha = 70^\circ$ and with recessed shielding (see Figure 6.1) at $\alpha = 85^\circ$. For the later one, the same horizontal and vertical erosion rates profiles were observed. At $\alpha = 70^\circ$, similar drifts were found although not as pronounced ($R_{\neq} = 5$) due to a smaller value of B_{\parallel} and a smaller difference in connection length. The mean sputtering rate with B-field is smaller than at $\alpha = 85^\circ$ and $R_{B/no\ B} = 82$. For oblique B-fields, a larger angle between surface normal and B-field leads to higher inhomogeneities in the cleaning while for perpendicular and oblique magnetic fields, a larger mean erosion rate was observed for bigger α and is due to the combination of two effects: (i) better confinement ($\mathbf{E} \times \mathbf{B}$) of charged particles as already observed in [127] and (ii) increased sputtering yield as ions hit the target at more oblique angle (see Figure 2.5 (c)).

Although strong erosion rates inhomogeneity were observed, it should not be forgotten that a stable discharge was obtained in those harsh conditions and that the whole sample was eroded. These results indicate that in situ RF cleaning could be operated in ITER and by tuning the gas and ion energy properly (for example He or D_2), avoiding substrate sputtering, the inhomogeneity issue could be minimized. Further investigations are mandatory to see if inhomogeneities could be decreased, for example by increasing the gas pressure or tuning the self-bias, e.g. E-field.

6.2.1.5 Working with ITER remnant B-field

If the cleaning inhomogeneities cannot be reduced at 3.5 T B-field and are asserted to be too high for in situ RF cleaning by ITER Diagnostic team, the magnets of ITER could potentially be turned-off. The residual magnetization due to the vacuum vessel would be equal to 0.4 mT. To show that cleaning in such conditions would result in an homogeneous etching, an experiment was conducted at $\alpha = 85^\circ$ and $B = + 0.4$ mT. The horizontal and vertical erosion rate profiles were measured but are not shown here as they are the same as for the case without B-field presented in section 6.1.1, Figure 6.2. No B-field related drift is observed when working with ITER remnant B-field values.

6.2.2 Cleaning in EAST tokamak

Based on the good results obtained previously, it was decided to do a cleaning trial with a large mirror, the ETS mock-up, in a tokamak with high magnetic field (1.7 T): EAST tokamak in China [128]. The ETS mock-up was introduced in EAST via the Material and Plasma Evaluation System (MAPES) [129] located in the H sector of EAST device. The ETS mock-up was localized on the FW (see Figure 6.10). The angle α is defined between the B-field and normal to the surface but in Figure 6.10, the angle between the surface and the B-field ($90^\circ - \alpha$) is represented where α is defined as before. All the results will be reported in a paper currently under review in Nuclear Fusion (*Plasma cleaning of ITER edge Thomson scattering mock-up mirror in EAST tokamak* by Rong Yan).

RF cleaning using Ne gas was carried out on the SS mock-up, with Mo mirrors coated with 10 nm Al_2O_3 at $\alpha = 70^\circ$ and 85° and showed promising results. The numbering system for the mirrors is the same as for the previous experiment (see Figure 6.4 or 6.12).

- It was possible to run a Ne discharge on a large mirror for several hours with a 1.7 T magnetic field. The achieved absolute self-bias was lower than for the laboratory experiments by a factor 2 and 10 for 70° and 85° inclined magnetic field angle respectively.
- Al was not removed in the shadow of large dust particles on the surface indicating that Ne ions are incoming with an oblique angle to the surface when the discharge is magnetized as shown in Figure 6.10. This behaviour was predicted by Chodura *et al.* (see section 2.4).

- The concept of plasma cleaning was successfully proved in EAST. All mirrors were etched at 70° and 85° . Total reflectivity was completely recovered for all the mirrors except for the edgiest one (# 2) cleaned for 85° case. The central inset mirrors systematically exhibited higher diffuse reflectivity and surface roughness. The cleaning was at least 40 times faster in EAST compared to laboratory experiments without magnetic field.

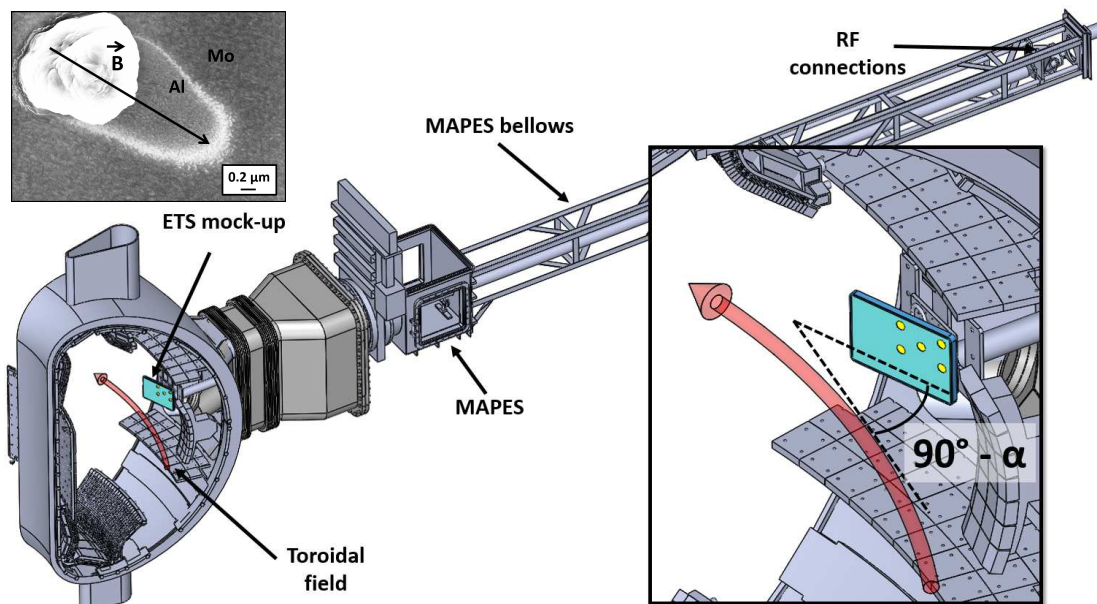


Figure 6.10: Illustration of the ETS mock-up fixed on the MAPES manipulator and inserted in EAST. The exact position and angle (α) between the surface of the ETS mock-up and the magnetic field is shown in the inset (here $\alpha = 70^\circ$). The toroidal field is represented by the red arrow. The location of the electrical RF connection is indicated on the schematic. SEM top view images after cleaning of the mirror #2 cleaned at $\alpha = 70^\circ$ where a dust particle is shadowing the Al deposits. The orientation of the B field is depicted.

The first cleaning trial exhibited promising results and further cleaning campaigns are foreseen. They will include plasma measurements with Langmuir probe as well as cleaning in the driven grounded electrode mode. However, to obtain a perfect mapping of the erosion rate over the whole surface, a similar method as the one employed in previous sections with large coated electrodes should be used in EAST.

6.3 Driven grounded electrode configuration

The working principle of this specific type of configuration was introduced in section 2.3, with first experimental measurements shown in section 4.2.5. Briefly, it consists of a regular capacitively coupled discharge where the DC component on the electrode is short-circuited, e.g. $V_{bias} = 0$ V. In case of an insulating films, negative charges can build-up on the surface and thus the normal capacitively coupled situation is restored. For conducting films, a high plasma potential develops to compensate for the loss of electrons. The sample as well as the walls are sputtered by high energy ions.

6.3.1 48 mm diameter mirror

Before coming to etching results, measurements of plasma parameters were performed with RFEA in the B-field chamber using the double electrode configuration (see Figure 6.15). Usually

those are done by applying RF directly to the analyser but in the present case, when the RFEA was short-circuited, the device was not working properly. The plasma was therefore run on a Cu electrode and the RFEA was embedded in a grounded counter electrode. Because the driven electrode and analyser were close to each other (approx. 5 cm, see Figure 6.15) and on the same potential, the measured ion energy distribution and flux on the RFEA can be assumed on the driven electrode. A similar measurement method was employed in [42]. In the normal CCP discharge mode, 10 W of RF power were needed to achieve a bias of -250 V, enabling a stable discharge for measurements. In this case, the maximum and average ion energy are respectively 260 and 167 eV with ion flux of 0.27 A.m^{-2} . When the electrode was short-circuited, the self-bias dropped to zero leading to an increase of the plasma potential. This induces that both driven and grounded electrodes are bombarded with ions having a maximum and mean ion energy of respectively 165 and 118 eV with 0.11 A.m^{-2} flux. With the same RF power, the sputtering is thus smaller both in flux and energy when passing to the short-circuited mode. The ion energy distributions of both modes are depicted in Figure 6.11. To compare etching properties of the short-circuited case to the one done in section 6.1.1, similar cleaning conditions were applied, but the RF power was doubled to increase the plasma potential and maintain the mean ion energy obtained at $V_{bias} = -200$ V (measured with RFEA). The etching rate was estimated by using the Cu electrodes coated with Mo followed by EDX analysis. The etching rate profile is presented in Figure 6.11.

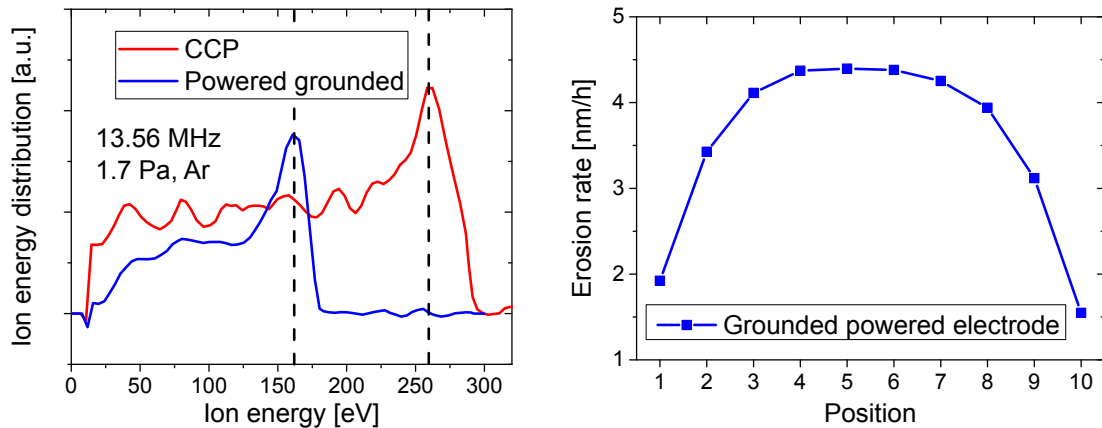


Figure 6.11: Ion energy distribution for argon plasma at -250 V equivalent self-bias for normal (CCP) and driven grounded electrode configurations.

Similarly to the experiment without DC short-circuit, the etching is symmetric around the central point of the electrode. The erosion is much more pronounced in the central region and edge effects have vanished. The inhomogeneity of the cleaning process could originate from the fact that the discharge is more confined in the central part, leading to higher plasma potential and densities in this region.

6.3.2 Edge Thomson scattering mirror mock-up

The tests were further extended to large mirror such as the ETS mock-up ($200 \times 300 \text{ mm}^2$). Equivalently to experiments performed in section 6.1.3, a fully insulating plate (anodized alumina) and a conducting plate (SS) were employed and small Mo mirror insets, coated with 25 nm Al_2O_3 were embedded in the plates to characterize the cleaning homogeneity. At the time of the experiments no RFEA measurements were not available and all the parameters were kept same as for the experiment in normal CCP case, including the RF power (80 W). From plasma potential measurements shown in Figure 4.9, we see that the expected potential at 80 W is 180 V and hence a maximum ion energy of 180 eV. For the same RF power, the normal CCP case has a bias of -200 V and a plasma potential of approx. 30 V, leading to a

maximum ion energy of 230 eV. In the driven grounded electrode mode, the ion energy is thus lower than for the normal case but still high enough to cause sputtering (RFEA measurements should be performed to confirm this assumption). For both different mock-ups, the results were quite surprising. For the insulating plate, after 6 h of cleaning, the amount of Al increased on all the inserts as can be seen in Figure 6.12 from cycle 0 (initial) to 1. When the electrode is fully insulating, negative charges can accumulate on the surface acting as a capacitance, and the situation is thus comparable to the normal case where a self-bias can develop. Yet in our case, we have two different surfaces. An anodized plate, composing the majority of the area and capable of handling large surface potential, and mirror insets, only covered with 25 nm of alumina, and thus, vulnerable to dielectric breakdown at much lower voltages. Therefore, one hypothesis explaining the obtained results assumes a large negative charging on the alumina plate accompanied by strong sputtering. A small fraction of the eroded Al is re-deposited (through collisions or ionization) on the whole surface, including on the insets. In the normal CCP mode, this wouldn't be an issue as the insets are equally sputtered but in the present case, the surface of insets cannot charge up negatively and ions are not accelerated with sufficient energy to compensate the re-deposition. This behaviour indicates a strong sputtering selectivity depending on the local surface dielectric properties. To our knowledge, it is the first time ever that such a property was reported for RF plasma discharges. Further investigations on this method are currently envisaged in our group but fall beyond the scope of this thesis.

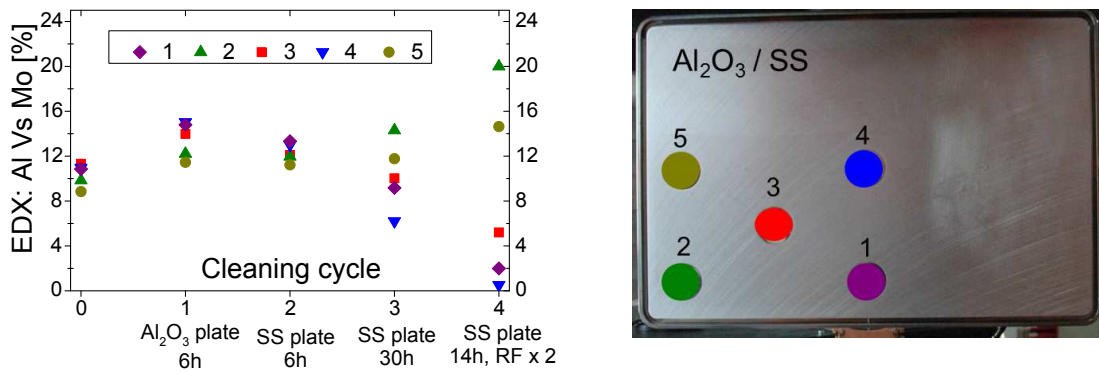


Figure 6.12: Ratio of EDX measurements for Al and Mo content as function of cleaning cycle. The first cycle was done on Al anodized plate. As it was not working, the samples were mounted into the SS plate for 3 further cleaning cycles. The RF power was doubled for the last one (#4).

As cleaning of insets when embedded in a large insulating electrode were not successful, they were placed in the SS plate as is (cycle #1 in Figure 6.12). Three cleaning cycles were performed and for the last one, the power was doubled (to speed up the process). Before analysing the results, it is worth mentioning that the ETS mock-up was placed vertically in the ESCA-1 cylindrical vacuum chamber. The left and right edges were thus closer to the walls (≈ 6 cm) than the middle of the ETS mock-up (≈ 13 cm). As can be seen from the EDX measurements, the Al amount was decreased for the most central insets (4, 1 and 3) and virtually increased for the edgy insets (5 and 2). In reality, the amount of Al did not increase on mirror 5 and 2 but stayed unchanged. In fact, EDX and XPS measurements confirmed the presence of iron (Fe), main component from the SS plate on those two mirrors, decreasing the EDX signal from Mo (leading to a virtual increase of the Al content). As the SS plate is conducting, the plasma potential strongly increases in that experiment (around 180 V for 80 W and 330 V for 160 W, estimated with linear fit see section 4.2.5), leading to sputtering of the wall. Because the discharge is confined in the vicinity of the driven electrode, the samples located in the centre (1, 3 and 4) have low re-deposition from the facing wall and are in net-erosion conditions, e.g. the Al content decreases. For samples 5 and 2, closer to the wall, they experienced much more re-deposition and are thus in net-deposition conditions. The Al of those samples is not sputtered

and even recovered with the main component of the ETS mock-up made of SS: Fe. Using this method in ITER would therefore only be possible if no surrounding walls are in close vicinity of the FMs.

6.3.3 Oblique and high B-field: $\alpha = 85^\circ$, ± 3.5 T

The aim of this experiment was to verify if a homogeneous etching was possible over $\varnothing 48$ mm electrode, for $\alpha = 85^\circ$ for both magnetic field orientations at 3.5 T. The same conditions were used as in section 6.2.1.4. Without going too much into details, similar behaviour as in normal CCP were observed here, namely a higher erosion on the top of the sample compared to the bottom (closer region to the top cover) and less erosion in the $\mathbf{E} \times \mathbf{B}$ direction. The image of the sample and erosion profile obtained at +3.5 T are shown in Figure 6.13 (a), (b) and (c). By changing the direction of the B-field, the vertical erosion profile stays unchanged while the horizontal one is rotated by 180° (not shown here). On the bottom left or right of both samples, a net re-deposition region of Cu is observed (dark orange spot on the pictures). This observation is particularly problematic for ITER as it implies that the surface of the FM cannot be sputtered entirely. When working in normal CCP case, this feature was not observed. The cleaning lasted 80 min and up to 10 nm of redeposited Cu was measured.

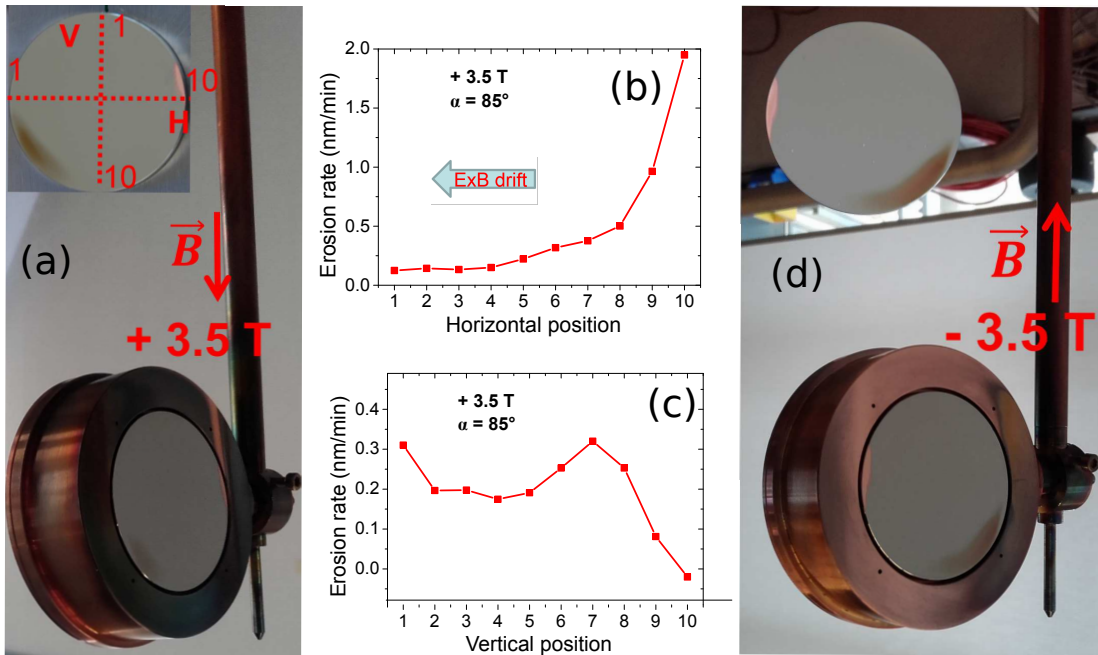


Figure 6.13: Picture and erosion profile for driven grounded electrode at 3.5 T and $\alpha = 85^\circ$. (a), (b) and (c) are for +3.5 T while (d) is for -3.5 T.

The origin of the Cu redeposition was investigated by performing several additional experiments. Based on the results, it seems that the Cu comes from the shielding. Indeed one experiment performed with lower exposure time to avoid the removal of Mo on the edge of the sample still had Cu redeposits. One possibility was also that Cu came from the wall of the chamber (from previous experiments) and the chamber was fully cleaned. Again Cu re-deposition was still observed. Finally, as the Cu is most likely originating from the shielding, one last experiment was done, trying to minimize the shielding etching. The shielding was therefore floating, allowing it to charge up to the floating potential (close to the plasma potential) to avoid ion sputtering. Again, this had no influence on the Cu re-deposition on the sample and posed the question of the ability to mitigate this effect for ITER.

6.3.4 Integration in ITER

Although worst results were obtained for the DC short-circuited plasma cleaning compared to the normal case, this method is still preferred by ITER, at least on an integration point of view. Indeed, almost all FMs will be water-cooled. To be able to simultaneously apply RF to the mirror and to cool them, three different possibilities exist:

1. Insulate the mirror electrically and provide cooling through a thermal (but not electrical) contact with a water cooled surface. It is not sure whether this solution can provide enough cooling to the FMs exposed to high neutron fluxes.
2. Connect the cooling water lines electrically to the mirror and decouple them from the grounded wall with an insulating contact at the vacuum vessel (see Figure 6.14 (a)). This solution has some issues: the feed-through should be made of an insulating material such as a ceramic, that could break leading to a so-called Loss-of-Cooling-Accident with water leak inside of the tokamak. Also, because the water is exposed to neutrons, it can become partially ionized. As the cooling water line are on DC-bias, this could lead to unpredicted currents or dissociation of the water molecules.
3. Integrating the cooling water lines in a stop band filter. The water pipe between the RF feed point and vacuum vessel feed-through forms a transmission line which is short-circuited at distance of $\lambda_{cable}/4$. This section is thus not seen by the RF generator. However, it is a DC short-circuit and prevents the development of V_{bias} on the mirror. This configuration represents the driven grounded electrode case. Such an integration scheme is shown in Figure 6.14 (b).

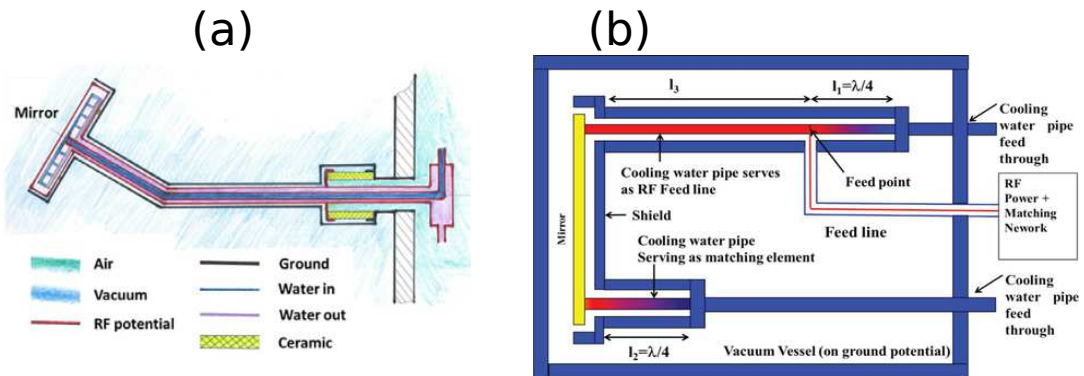


Figure 6.14: Illustration of two integration scheme for ITER. (a) is a based on an insulating feed-through and leads to normal CCP cleaning (with self-bias) and (b) is a schematic of the driven grounded electrode case where the water pipes are connected to the grounded vacuum vessel (without self-bias). Image (b) taken from [130].

For the last configuration using a stop band filter, pre-matching elements can be installed, contributing to a reduction of the power losses between the feed point and the mirror. This method was tested at the University of Basel with a 60 MHz CCP cleaning experiment. The required RF power to reach $V_{bias} = -270$ V could be reduced from 150 to 90 W by adding a 77 cm long open coaxial transmission line as pre-matching element (with a T-connector).

6.4 Double electrode

All the etching results presented up to now were limited to one driven electrode. However, in ITER the situation might more complicated as material eroded from the first mirror will also partially arrive at the second mirror (or third mirror in case of complex geometries as for

example the WAVS diagnostic, Figure 4.6). There might therefore be a need to clean those mirrors as well. One possibility would be to clean the several mirrors simultaneously. This can be achieved by using one RF power supply coupled to both mirrors or to feed independently each mirror with a unique RF power source. In both cases, if the RF frequency is the same, there will be a constant phase shift between the two RF signals. The influence of the phase shift as well as first etching results will briefly be introduced in the subsequent sections.

6.4.1 Phase shift influence

The following experiments were conducted in the B-field chamber with a double electrode configuration. To cover a wide range of angles between the mirror and the B-field orientation, 3 different arrangements were employed and are illustrated in Figure 6.15. Mirrors were either in parallel or anti-parallel configuration with an electrode gap between 1.5 and 7.5 cm, and each electrode was supplied with a unique RF source. The phase shift between them was controlled via a function generator and verified with an oscilloscope.

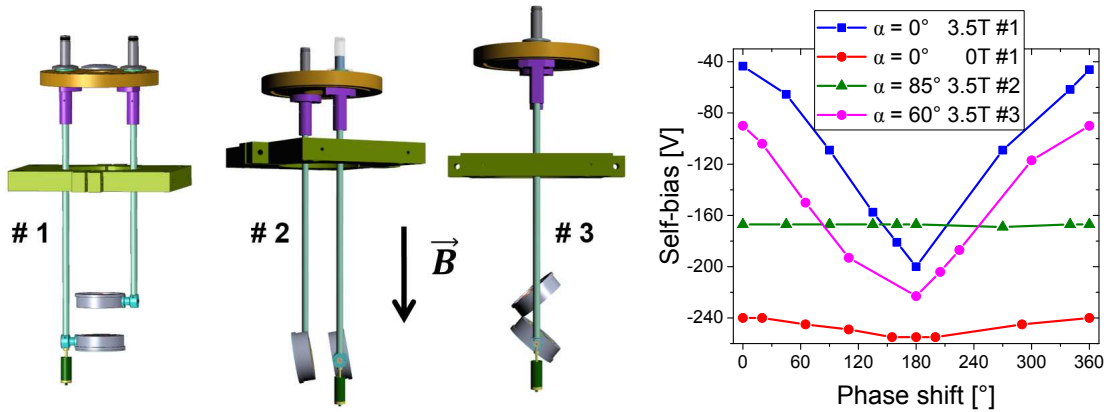


Figure 6.15: Illustration of the double electrode configuration with three different arrangements. #1 and #2 have parallel mirrors, #3 is anti-parallel mode. Configuration #1 is used to obtain $\alpha = 0^\circ$. Configuration #2 is employed for experiments at $\alpha = \pm 85^\circ$. Configuration #3 is employed for experiments at $\alpha = \pm 60^\circ$ Influence of the phase shift between the two electrodes on V_{bias} for different arrangements and magnetic field value.

Without B-field, the phase shift between the two electrodes has no influence on the bias value in all of the arrangements. With the B-field at +3.5 T, the situation changes due to the confinement of the discharge. At $\alpha = \pm 85^\circ$ (case # 2), the top and bottom walls of the chamber are still available as counter electrode, and the self-bias, although decreased due to the confinement, does not depend on the phase shift (Figure 6.15). When the angle is at 0° , the electrons can only move hardly to a grounded area (eventually they can get to the shielding of each opposite mirror). In that case, the phase shift between the electrodes plays an important role. When the mirrors have an 180° (0°) phase shift, they work together (against each other) and V_{bias} is the highest (smallest). Regarding the anti-parallel configuration (#3), the influence of the phase shift on the self-bias is situated between both cases mentioned above: a larger bias at 180° but only approx. 2 times smaller at 0° .

6.4.2 Etching profiles

The following experiments were performed in the B-field chamber with \varnothing 48 mm Cu electrodes coated with 200 nm Mo. The erosion is then characterized with EDX and STRATAGem software (see section 3.2.2). Vertical and horizontal erosion profile lines were systematically done but will not be shown. Only the main outcomes will be discussed subsequently. Without magnetic field, the phase shift was kept at 0° and with magnetic field, if a bias of -200 V could be achieved,

the same phase shift was conserved. Only one experiment with 3.5 T requested a phase shift of 180° , namely for arrangement #1 with $\alpha = 0^\circ$.

6.4.2.1 Without B-field

The first etching experiment was carried out on arrangement #1, and both electrodes have similar etching profiles, symmetric around the middle of the samples. The discharge conditions were kept the same as in section 6.1.1 and the RF power had to be slightly increased to achieve the -200 V bias (10 W instead of 8 W in single mode), originating from an increase in driven electrode area. Compared to the single electrode mode (see Figure 6.2), the only differences lie in the edge effect that is now recessed to the periphery of the sample (absence of re-deposition ring) and the erosion rate that is on average 1.7 times higher in double mode. The effect of re-deposition of Mo from one mirror to the other is thus not an issue (in the present case, the electrode gap d is 4 cm). No tests were conducted on arrangement #2 but similar erosion profiles as above are expected.

When the mirrors were arranged in anti-parallel configuration (arrangement #3), the situation was slightly different. On the horizontal axis, characterized by a constant electrode gap d , the erosion profile is the same as for the single electrode (see Figure 6.2). On the vertical axis, the erosion rate is the same as for the single electrode between the region with the largest electrode gap to the middle of the sample. Then, as the gap becomes smaller and smaller, the erosion rate stays constant and is not increasing again when going towards the edge, attributed to enhanced re-deposition in those regions.

Finally, one experiment was conducted in anti-parallel configuration (arrangement #3) but in the driven grounded electrode case. Again, the erosion profiles are similar to the single electrode case (see Figure 6.11) with on average smaller erosion rates (1.5 times smaller). The only difference appears in the electrode regions close to another (where the gap is the smallest). Indeed, no erosion was measured in the outer periphery of the samples, due to enhanced re-deposition.

6.4.2.2 With 3.5 T B-field

Four experiments in double electrode mode were performed at +3.5 T B field:

1. **Arrangement #1, $\alpha = 0^\circ$.** The erosion was the same on both mirrors with profile comparable to the double electrode mode without B-field. No strong central erosion as in the single mode at 3.5 T was observed (Figure 6.7). In comparison to the case without B-field, the erosion rates were 2.8 times higher.
2. **Arrangement #2, $\alpha = +/-85^\circ$.** The main drifts observed in the single electrode configuration at $\alpha = 85^\circ$ and -85° were again present in the double mirror mode: more erosion (i) horizontally in the inverse of the $\mathbf{E} \times \mathbf{B}$ direction and (b) vertically in the direction of the closest grounded wall (see Figure 6.8 and 6.9). Nevertheless, the mirror at $\alpha = 85^\circ$ exhibited net re-deposition regions, probably coming from the other electrode and consistent with the fact that the erosion rates were higher at $\alpha = -85^\circ$ in the single electrode case.
3. **Arrangement #3, $\alpha = +/-60^\circ$.** This situation is the most complicated to explain as no experiments were performed in single mirror configuration at 3.5 T. The main observation for this case is the presence of a non-negligible re-deposition area located in the middle of each sample (approx. 1.5×1.5 cm²).
4. **Arrangement #3, $\alpha = +/-60^\circ$, $V_{bias} = 0$ V.** The last test was done with both mirrors in the driven grounded electrode case. After more than 5 h (previous experiments lasted approx. 1 h), no erosion was measured by EDX analysis. This result indicates that the driven grounded electrode case might be problematic for cleaning several mirrors simultaneously in ITER in the presence of a magnetic field.

Conclusions and perspectives

7.1 Summary

WHEN beginning this thesis, the diagnostic scientific community was highly sceptical regarding the FMs issue, especially when the first simulations made by Kotov [30] showed that some diagnostic systems will experience strong reflectivity losses with as less as 4 ITER pulses. To solve this issue, in situ cleaning techniques are requested. The aim of this Ph.D. thesis was twofold: obtaining laboratory made deposits relevant to ITER and develop RF plasma cleaning intending to implement it in ITER optical diagnostic systems.

Plasma cleaning was quickly designated as the best solution and results presented in Chapter 4 highlighted one technique in particular: RF plasma cleaning, currently envisaged by ITER Organization diagnostic team as the most promising one. Indeed, the use of an external plasma source with DC-bias on the mirror will be inefficient on insulating deposits due to surface charging. Although promising results were found when employing an ion source, the difficulties regarding the implementation led to the withdraw of this technique for ITER. Two main configuration of RF discharges were studied in this work, capacitively coupled discharge and driven grounded electrode discharge. The discharges are defined by sheath and α heating, implying that the surface state of the mirror does not play a significant role in the sustaining mechanism. Switching from low RF (13.56 MHz) to higher RF frequencies such as 60 MHz permits to substantially increase the ion flux for a given ion energy by one order of magnitude. However, a strong increase in the RF power consumption was observed when changing to higher frequencies.

For complex geometries expected in ITER (small electrode gap or reduced wall area), ignition of plasma was always possible, but an increase in the pressure to 3 Pa was needed. In parallel, an increase of the mirror size towards the real-size of a FM ($200 \times 300 \text{ mm}^2$ for the ETS mock-up) was accompanied by an increase in the RF power consumption for a given self-bias. In the presence of a B-field, the confinement of the discharge led to a decrease of the self-bias for a given RF power. Those observations indicate that in situ RF discharges could be ignited and sustained in ITER, even in the case of complex geometries or presence of a magnetic field but will request higher RF powers to achieve a given self-bias.

In Chapter 5, a large variety of films was successfully cleaned restoring the initial high reflectance of mirrors and preserving their integrity. Dense and porous structures in metallic state as well as partially or fully oxidized based on Al (Be proxy), W and Be were obtained. The reflectivity of mirrors after contaminant deposition was found to strongly decrease with thin deposits, especially in the UV-Vis range. During the cleaning process, metallic Al or Be became oxidized and a similar behaviour is expected in ITER. For Al-based deposits, it was found that Ar at approx. 200 eV was the most appropriate gas to concede fast process with preservation of mirror integrity. When switching to Be, He was proven to be equivalently efficient as Ar but reduces roughening of Mo and Rh mirrors. Additionally, it was shown that removal of Mo oxide

Chapter 7. Conclusions and perspectives

is feasible with He. Finally, films from JET-ILW were proven to be easier to clean than those obtained from laboratory.

Two aspects of cleaning in ITER relevant conditions were mainly investigated in Chapter 6, cleaning large size mirrors and highly magnetized plasma. When performing experiments without B-field, it was shown that the etching process was homogeneous for samples up to $200 \times 300 \text{ mm}^2$, except for the periphery of the mirrors due to edge effects. It was also proven that the material of the mirror does not play a role in the etching process which is extremely positive for ITER as deposits might be inhomogeneous in thickness and composition on the surface of FMs.

In the presence of a magnetic field, a first experimental campaign at 3.5 T showed promising results except for parallel magnetic field to the surface ($\alpha = 90^\circ$). Several teams responsible of diagnostic systems have therefore implemented a minimum angle α between mirror normal and magnetic field equal to 85° . Further experimental campaigns showed that when the magnetic field was perpendicular to the surface ($\alpha = 0^\circ$), a strong plasma beam was observed in the centre of the discharge, probably responsible for the larger erosion rates observed in the central part of the sample. This filamentation could originate from the divergence of the B-field outside of the magnet, where the counter grounded electrode is located. When the angle between the B-field and the surface normal was increased (grazing angles), larger inhomogeneity were observed in vertical and horizontal directions. The horizontal drift was attributed to $\mathbf{E} \times \mathbf{B}$ drift of re-deposited particles. Regarding the vertical drift, two hypothesis were proposed. The first one is based on the difference in connection length between the electrode and the grounded counter-electrode. For the second one, the driving phenomenon is believed to be the electron motion leading to fluctuations in the plasma density. In EAST tokamak, all the insets were cleaned and no strong inhomogeneity were observed. Additional experiments were also performed in double electrode configuration and homogeneous etching profiles were obtained without magnetic field while experiments performed in the presence of a 3.5 T magnetic field exhibited inhomogeneous cleanings with area of net re-deposition.

In addition to normal capacitively coupled plasma, investigations were conducted on the driven grounded electrode configuration. In the case of an insulating electrode, the discharge behaves like the regular capacitively coupled plasma. When the electrode is conductive, a high plasma potential develops, leading to an equivalent sputtering of the electrode. On $\varnothing 48 \text{ mm}$ electrodes, the erosion profile was found to be homogeneous. For the ETS mock-up, two main trends were observed: (i) for the insulating plate, the insets were not eroded and the amount of alumina even increased. For the metallic plate, erosion was observed in the central part but not in the edges where re-deposition of material from the mirror took place. This behaviour is attributed to the sputtering of the wall. In the presence of a magnetic field (3.5 T) at a grazing angle ($\alpha = 85^\circ$), re-deposition of Cu from the shielding was observed on the electrode implying that region of net re-deposition are present. The use of this technique could thus be problematic in the presence of a magnetic field.

Re-deposition experiments were accomplished in the B-field chamber. The aim of this campaign was to estimate the ejection angle distribution of the sputtered particles (the ejection law) with and without B-field to provide experimental data for ITER. Results (not shown in this thesis) exhibited a \cos^n power law dependence for the ejection function with $n \approx 0.6$. With a 3.5 T B-field, the situation is much more complex. Indeed, the electrode is not any more sputtered homogeneously and a non-negligible fraction of eroded material is re-ionized in the plasma.

Finally, a campaign was started in the group to study the effect of multiple deposition/cleaning cycles on optical properties of mirrors. The tests were performed on Mo (poly, single and nanocrystalline) and Rh (nanocrystalline). The single and nanocrystalline Mo and Rh could withstand up to 34 cycles while polycrystalline Mo mirrors exhibited a strong increase of diffuse reflectivity. Those results will be published in [10].

7.2 Guidebook

Based on the results obtained in this thesis and discussion with responsible of several diagnostics and the ITER Organization diagnostic team, a guide for ITER, giving the baseline for a plasma cleaning scenario as well as requested additional experiments for proper implementation of in situ RF plasma cleaning in ITER is given below and will contain: (i) implications of the main thesis findings for ITER in situ RF cleaning and (ii) further experimental proposals to solve remaining issues and unknowns.

- **Guidance #1, Universality of RF plasma cleaning**

Results: In situ RF plasma cleaning was found to be effective on a large variety of deposits, including insulating deposits (shown to be the hardest deposits to remove). Cleaning in ITER could be performed with He, effective on Be/W deposits and strongly reducing the impact of etching on the mirrors optical properties. Also, He is efficient to sputter Mo oxide.

Implications: Future experimental tests regarding FMs cleaning could be performed with laboratory based deposits such as dense Al_2O_3 . In addition, FMs will be oxidized due to installation years before the beginning of operation or due to Loss-of-Cooling-Accident but oxide layers can be removed with He. Implanted species in the first nanometres of FMs can also be etched away.

Issue: One specific class of material was not investigated in the present thesis: nitrides. Indeed, due to nitrogen seeding in the fusion plasma, Be, W or Mo might form nitrides.

Solution: Investigations on cleaning of nitrides should be performed to assess the universality of RF cleaning for all types of contaminants that might be present in ITER.

- **Guidance #2, Chemical sputtering**

Goal: D_2 might be very effective for Be etching, especially when considering chemical erosion (formation of BeD), already present at very low ion energies (≈ 30 eV) [67].

Issue: The impact of O or W presence in the film is not known. Indeed the presence of BeO or Be_2W could disable chemical sputtering while films containing too much W might not be sputtered.

Proposal: An experimental campaign is currently investigating chemical sputtering in INFLPR and exhibits very promising results regarding pure Be deposits. Further experiments will be devoted to BeO and Be/W contaminant layers.

- **Guidance #3, Achieving a required self-bias in ITER**

Results: Higher excitation frequencies, complex wall geometries and presence of magnetic field will strongly increase the required RF power to achieve a given self-bias.

Issue: In this thesis, the impact of the above-mentioned conditions was studied independently and not together (either high frequency or complex geometries or magnetic field). Regarding transmission lines, the use of too high RF powers could lead to over-heating.

Proposal: Conduct an experimental campaign to investigate the synergetic effect of the above-mentioned conditions, for example in EAST tokamak. Optimize the RF power consumption by choosing adequate waveguides as well as pre-matching elements (see [130]).

- **Guidance #4, Edge effects**

Results: Enhanced erosion was measured on the periphery of the samples, due to edge effects.

Issue: The entire FM is designed to extract the light towards the detectors.

Proposal: Include a sacrificial periphery of about 1 cm in the FM design.

- **Guidance #5, Cleaning with oblique B-field**

Results: At B-fields up to 3.5 T and α up to 85° , strong inhomogeneity in the horizontal and vertical erosion profiles were observed.

Issue: The origin of vertical drifts should be verified. A way to reduce horizontal and vertical inhomogeneities should be found.

Proposal: Firstly, the hypothesis concerning the vertical drift via the connection length should be verified by using a tilted counter-electrode. If the inhomogeneity vanishes, a similar configuration could be employed in ITER. Secondly for horizontal inhomogeneities led by $\mathbf{E} \times \mathbf{B}$ drift, reducing the value of \mathbf{E} or \mathbf{B} would decrease the drift and an equilibrium between the re-deposition and the erosion could be found to balance both phenomena. The impact of a smaller pressure on the amount of re-deposition should be examined (fewer collisions and hence re-ionization).

- **Guidance #6, Tuning the B-field and FM geometry in ITER**

Goal: Optimize the strength of the B-field as well as the geometry of FMs in their grounded environment to reduce inhomogeneities while ensuring a fast cleaning process.

Issue: The question is complex due to the interconnection of several effects and can probably only be solved through simulations, benchmarked experimentally. Correct plasma parameters are mandatory for proper simulations.

Proposal: Characterisation of the plasma parameters ($T_e, n_e, n_i \dots$) should be performed. Langmuir probe measurements are planned to be done within the next months in EAST tokamak.

- **Guidance #7, Cleaning in high B-fields with strong inhomogeneities**

Goal: In the case where the B-field cannot be turned-off in ITER, remaining at 3.5 T, and that erosion inhomogeneities cannot be improved, a proper solution for FM cleaning should be found.

Results: Experimentally, cleaning in the presence of magnetic field did not lead to net re-deposition regions, indicating that contaminants can be etched away from the whole surface, although with different speeds. Also, He or D_2 could be used in ITER with the advantage of having a low sputtering yield on Mo or Rh.

Solution: By working below the sputtering threshold of Mo or Rh (for example by employing D_2 at 30 eV), inhomogeneity in sputtering would not be an issue. If this is not possible, the choice of gas and energy should be made in a way to have as large differences as possible in sputtering yield between mirror and contaminants.

- **Guidance #8, Determination of re-deposition pattern**

Proposal: Develop a numerical model to estimate the ejection law of eroded particles in the presence of a strong B-field.

- **Guidance #9, Driven grounded electrode configuration**

Results: Promising results were found in this configuration, with etching of insulating and conducting contaminants. For insulating deposits with different thicknesses, the thicker part was removed faster.

Implications: For FMs being coated unevenly by insulating deposits, the thicker regions will be eroded faster, leading to a homogeneous removal.

Results: Strong deposition of material from the counter-electrode was observed when the wall was too close to the mirror. In the presence of a magnetic field, re-deposition area appeared on the sample.

Solution: If this method is employed in ITER, special care has to be taken regarding the design of the optical components and the surrounding wall. Also, the magnetic field will have to be switched off during the cleaning process to avoid re-deposition areas.

- **Guidance #10, Estimation of cleaning advancement**

Issue: In ITER, an in situ monitoring of the cleaning advancement is mandatory.

Solution: Live reflectivity measurements similarly to the one done in Basel could be performed in ITER using a retro-reflector, a calibrated plasma scenario or a secondary optical path used for calibration. A method proposed by Dickheuer *et al.* [131] based on Doppler shift could also be implemented in ITER.

Results: Optical emission spectroscopy of the cleaning plasma could be performed. First promising results were shown in [87].

Results: When the discharge are governed by γ heating, the surface properties of the electrode are influencing the plasma parameters (n_e , n_i ...) through secondary electron emission. The discharges employed in this work were governed by α heating being extremely insensitive to the surface properties.

Proposal: By increasing the self-bias and pressure briefly, the discharge could enter a γ mode heating. Depending on the state of the surface (metallic, insulating ...), the plasma density will change. By properly calibrating the discharge, it could be possible to get information on the surface state.

List of Figures

1.1	Fusion reactions cross sections	6
1.2	Schematic view of a tokamak	7
1.3	Divertor configuration	8
1.4	ITER reactor and construction site	9
1.5	ITER cutaway	10
1.6	Diagnostic systems in ITER	11
1.7	Optical layout for diagnostics	11
1.8	Sectional view of ITER vessel	12
1.9	Reflectance of W mirrors	13
1.10	JET-ILW First Mirror	14
1.11	Mirror exposed in PISCES-B	14
2.1	Symmetric and asymmetric discharges	20
2.2	Illustration of DC-coupled and capacitively coupled electrodes	22
2.3	Magnetic pre-sheath	25
2.4	Linear collision cascade	26
2.5	Sputtering yield	27
3.1	Drawing of ESCA-1	32
3.2	Capacitively coupled plasma	33
3.3	Experimental setup used in JET-BeHF	33
3.4	B-field chamber	34
3.5	Schematic view of the XPS method	35
3.6	Electron-trajectory SEM	36
3.7	Thickness estimation with EDX	37
3.8	Description of the behaviour of the light at the interface between two media	38
3.9	PVD growth model	42
3.10	Top/bottom magnetron configuration	43
4.1	Evolution of in-situ relative reflectivity measurements	46
4.2	XPS spectra of the porous Al/Al _{oxide} films exposed to external plasma source	47
4.3	SEM pictures of the porous Al/Al _{oxide} films exposed to external plasma source	47
4.4	Self-bias and ion flux as a function of the applied RF power	49
4.5	Ion energy distribution for different pressures and RF frequencies	50
4.6	Schematic of the WAVS front end mirrors	52
4.7	Smaller grounded electrodes configuration	52

List of Figures

4.8	Plasma potential and ion flux on ETS mock-up	55
4.9	Plasma potential and ion flux on driven grounded ETS mock-up	56
4.10	PIC-MCC simulation of CCP plasma discharge	58
4.11	Evolution of self-bias with B-field strength	59
5.1	50 % Reflectivity drop for a Mo mirror coated with porous Al/Al _{oxide}	62
5.2	Characterizations of facing magnetron deposits	63
5.3	Reflectivity measurements of the porous Al/Al _{oxide} /W films exposed to RF plasma	64
5.4	XPS measurements of the porous Al/Al _{oxide} and W films exposed to RF plasma	65
5.5	Reflectivity measurements of Be coated mirrors	66
5.6	Reflectivity measurements of cleaned sample P1-1 in JET-ILW	70
5.7	SEM of cleaned samples from UCSD	70
5.8	Reflectivity measurements of cleaned sample R3-2 in JET-ILW	72
5.9	SEM of cleaned samples from INFLPR	72
5.10	XPS of cleaned Be coated samples in Basel	74
5.11	Reflectivity of cleaned Be coated samples in Basel	74
5.12	Locations of mirrors in JET-ILW	76
5.13	Reflectivity measurements of JET-ILW mirrors	78
5.14	SEM images of JET-ILW mirror 77	78
5.15	Reflectivity measurements of JET-ILW mirrors	79
6.1	E field distribution for B-field electrode	82
6.2	Erosion profile after plasma cleaning on \varnothing 48 mm sample, flat shielding	83
6.3	Erosion profile after plasma cleaning on \varnothing 48 mm sample, retracted shielding	83
6.4	ETS mock-up	85
6.5	Experiment ETS-SS mock-up	86
6.6	Picture of the electrode after etching at $\alpha = 90^\circ$	87
6.7	Erosion profile at 3.5 T, $\alpha = 0^\circ$	88
6.8	Erosion profile at ± 3.5 T, $\alpha = 85^\circ$	90
6.9	Erosion profile at + 3.5 T, $\alpha = - 85^\circ$	91
6.10	Illustration of the ETS mock-up installed in EAST	93
6.11	Ion energy distribution for power grounded electrode case	94
6.12	Experiment ETS mock-up DC grounded	95
6.13	Picture and erosion profile for driven grounded in B-field	96
6.14	Illustration of two integration scheme for ITER.	97
6.15	Illustration of the double electrode configuration.	98

List of Tables

1.1	Main parameters of ITER	9
2.1	Sputtering yield at 200 eV	28
2.2	Damage threshold for sputtering	29
4.1	Measurements plasma properties	50
4.2	Measurements plasma properties for different grounded area	53
4.3	Measurements plasma properties for different driven electrode area	53
4.4	Wavelength for different frequencies	54
4.5	Results from simulations	57
5.1	Production of contaminants	62
5.2	Cleaning results for laboratory deposits	64
5.3	Be coated mirrors characteristics	66
5.4	Fitting parameters for Be films	67
5.5	Experimental conditions Be cleaning	68
5.6	JET-ILW mirrors	76
5.7	Cleaning results for JET-ILW mirrors	77

Bibliography

- [1] E. Mukhin, V. Semenov, A. Razdobarin, S. Y. Tolstyakov, M. Kochergin, G. Kurskiev, K. Podushnikova, S. Masyukevich, D. Kirilenko, A. Sitnikova *et al.*, “First mirrors in ITER: material choice and deposition prevention/cleaning techniques,” *Nuclear Fusion*, vol. 52, no. 1, p. 013017, 2011.
- [2] M. Walsh, P. Andrew, R. Barnsley, L. Bertalot, R. Boivin, D. Bora, R. Bouhamou, S. Ciattaglia, A. Costley, G. Counsell *et al.*, “ITER diagnostic challenges,” in *Fusion Engineering (SOFE), 2011 IEEE/NPSS 24th Symposium on*. IEEE, 2011, pp. 1–8.
- [3] F. Leipold and R. Reichle, “Workshop First Mirror Surface Recovery at ITER IO, Aix en Provence, France,” 23-24.04.2013. [Online]. Available: <https://user.iter.org/?uid=G8TEVV>
- [4] M. De Bock, R. Barnsley, M. Bassan, L. Bertalot, B. Brichard, I. Bukreev, J. Drevon, F. Le Guern, R. Hutton, M. Ivantsivskiy *et al.*, “ITER perspective on fusion reactor diagnostics—A spectroscopic view,” *Journal of Instrumentation*, vol. 11, no. 08, p. P08010, 2016.
- [5] M. Bassan, P. Andrew, G. Kurskiev, E. Mukhin, T. Hatae, G. Vayakis, E. Yatsuka, and M. Walsh, “Thomson scattering diagnostic systems in ITER,” *Journal of Instrumentation*, vol. 11, no. 01, p. C01052, 2016.
- [6] L. Moser, R. Steiner, F. Leipold, R. Reichle, L. Marot, and E. Meyer, “Plasma cleaning of ITER first mirrors in magnetic field,” *Journal of Nuclear Materials*, vol. 463, pp. 940–943, 2015.
- [7] L. Moser, L. Marot, B. Eren, R. Steiner, D. Mathys, F. Leipold, R. Reichle, and E. Meyer, “Towards plasma cleaning of ITER first mirrors,” *Nuclear Fusion*, vol. 55, no. 6, p. 063020, 2015.
- [8] L. Moser, L. Marot, R. Steiner, M. Newman, A. Widdowson, D. Ivanova, J. Likonen, P. Petersson, G. Pintsuk, M. Rubel *et al.*, “Plasma cleaning of beryllium coated mirrors,” *Physica Scripta*, vol. 2016, no. T167, p. 014069, 2016.
- [9] L. Moser, R. Doerner, M. Baldwin, C. Lungu, C. Poroniscu, M. Newman, A. Widdowson, E. Alves, G. Pintsuk, J. Likonen, A. Hakola, R. Steiner, L. Marot, and E. Meyer, “Investigation and plasma cleaning of first mirrors coated with relevant ITER contaminants: beryllium and tungsten,” *Nuclear Fusion*, 2017. [Online]. Available: <http://iopscience.iop.org/10.1088/1741-4326/aa73e2>
- [10] L. Moser, L. Marot, R. Steiner, R. Reichle, F. Leipold, C. Vorpahl, F. Le Guern, U. Walach, S. Alberti, I. Furno, R. Yan, J. Peng, M. Ben Yaala, and E. Meyer, “Plasma cleaning of ITER first mirrors,” *Physica Scripta*, vol. 2017, 2017.
- [11] J. D. Lawson, “Some criteria for a power producing thermonuclear reactor,” *Proceedings of the Physical Society. Section B*, vol. 70, no. 1, p. 6, 1957. [Online]. Available: <http://stacks.iop.org/0370-1301/70/i=1/a=303>
- [12] S. Atzeni and J. Meyer-ter Vehn, *The Physics of Inertial Fusion: Beam-Plasma Interaction, Hydrodynamics, Hot Dense Matter*. Oxford University Press on Demand, 2004, no. 125.
- [13] P. C. Stangeby *et al.*, *The plasma boundary of magnetic fusion devices*. Institute of Physics Publishing Bristol, 2000, vol. 224.

Bibliography

- [14] *Web page of ITER*, Std. [Online]. Available: <http://www.iter.org/>
- [15] I. P. E. G. on Confinement, Transport, I. P. E. G. on Confinement Modelling, Database, and I. P. B. Editors, "Chapter 2: Plasma confinement and transport," *Nuclear Fusion*, vol. 39, no. 12, p. 2175, 1999. [Online]. Available: <http://stacks.iop.org/0029-5515/39/i=12/a=302>
- [16] M. Walsh, P. Andrew, R. Barnsley, L. Bertalot, R. Bouhamou, L. Caplat, N. Casal, G. Counsell, M. Dapena, M. De Bock *et al.*, "Integration of diagnostics on ITER," in *Fusion Engineering (SOFE), 2015 IEEE 26th Symposium on*. IEEE, 2015, pp. 1–8.
- [17] K. Ebisawa, A. Costley, A. Donne, G. Janeschitz, S. Kasai, A. Malaquias, G. Vayakis, C. Walker, S. Yamamoto, and V. Zaveriaev, "Plasma diagnostics for INTER-FEAT," *Review of Scientific Instruments*, vol. 72, no. 1, pp. 545–550, 2001.
- [18] T. Sugie, "12th Meeting of the ITPA Topical Group Diagnostic," 26 - 30 March 2007, PPPL, Princeton.
- [19] A. Litnovsky, P. Wienhold, V. Philipps, G. Sergienko, O. Schmitz, A. Kirschner, A. Kreter, S. Droste, U. Samm, P. Mertens *et al.*, "Diagnostic mirrors for ITER: a material choice and the impact of erosion and deposition on their performance," *Journal of Nuclear Materials*, vol. 363, pp. 1395–1402, 2007.
- [20] S. Lindig, M. Balden, V. K. Alimov, A. Manhard, C. Höschen, T. Höschen, B. Tyburska-Püschel, and J. Roth, "Sub-surface structures of ITER-grade W (Japan) and re-crystallized W after ITER-similar low-energy and high-flux D plasma loadings," *Physica Scripta*, vol. 2011, no. T145, p. 014039, 2011.
- [21] V. Voitsenya, A. Costley, V. Bandourko, A. Bardamid, V. Bondarenko, Y. Hirooka, S. Kasai, N. Klassen, V. Konovalov, M. Nagatsu *et al.*, "Diagnostic first mirrors for burning plasma experiments," *Review of scientific instruments*, vol. 72, no. 1, pp. 475–482, 2001.
- [22] M. Joanny, J. Travere, S. Salasca, L. Marot, E. Meyer, C. Thellier, C. Cammarata, G. Gallay, and J. Ferme, "Achievements on engineering and manufacturing of ITER first mirrors mock-ups," in *Fusion Engineering (SOFE), 2011 IEEE/NPSS 24th Symposium on*. IEEE, 2011, pp. 1–6.
- [23] M. Rubel, J. Coad, G. De Temmerman, A. Hakola, D. Hole, J. Likonen, I. Uytendhouwen, A. Widdowson, J.-E. Contributors *et al.*, "First Mirrors Test in JET for ITER: An overview of optical performance and surface morphology," *Nuclear Instruments and Methods in Physics Research Section A: Accelerators, Spectrometers, Detectors and Associated Equipment*, vol. 623, no. 2, pp. 818–822, 2010.
- [24] M. Rubel, D. Ivanova, J. Coad, G. De Temmerman, J. Likonen, L. Marot, A. Schmidt, A. Widdowson, J.-E. contributors *et al.*, "Overview of the second stage in the comprehensive mirrors test in JET," *Physica Scripta*, vol. 2011, no. T145, p. 014070, 2011.
- [25] M. Richou, C. Martin, P. Delhaes, M. Couzi, W. Saikaly, C. Brosset, B. Pégourié, A. Litnovsky, V. Philipps, P. Wienhold *et al.*, "Physico-chemical characteristics of carbon deposits collected in TEXTOR and Tore Supra tokamaks," *Carbon*, vol. 45, no. 14, pp. 2723–2731, 2007.
- [26] A. Litnovsky, M. Matveeva, A. Herrmann, V. Rohde, M. Mayer, K. Sugiyama, K. Krieger, V. Voitsenya, G. Vayakis, A. Costley *et al.*, "First studies of ITER-diagnostic mirrors in a tokamak with an all-metal interior: results of the first mirror test in ASDEX Upgrade," *Nuclear Fusion*, vol. 53, no. 7, p. 073033, 2013.
- [27] D. Ivanova, M. Rubel, A. Widdowson, P. Petersson, J. Likonen, L. Marot, E. Alves, A. Garcia-Carrasco, G. Pintsuk, J.-E. Contributors *et al.*, "An overview of the comprehensive First Mirror Test in JET with ITER-like wall," *Physica Scripta*, vol. 2014, no. T159, p. 014011, 2014.
- [28] L. Marot, E. Meyer, M. Rubel, D. Ivanova, A. Widdowson, J. Coad, J. Likonen, A. Hakola, S. Koivuranta, G. De Temmerman *et al.*, "Performances of Rh and Mo mirrors under JET exposure," *Journal of Nuclear Materials*, vol. 438, pp. S1187–S1191, 2013.
- [29] G. De Temmerman, M. Baldwin, R. Doerner, D. Nishijima, R. Seraydarian, K. Schmid, F. Kost, C. Linsmeier, and L. Marot, "Beryllium deposition on International Thermonuclear Experimental Reactor first mirrors: Layer morphology and influence on mirror reflectivity," *Journal of applied physics*, vol. 102, no. 8, p. 083302, 2007.
- [30] V. Kotov, D. Reiter, A. Kukushkin, and H. Pacher, "Numerical estimates of the ITER first mirrors degradation due to atomic fluxes," *Fusion engineering and design*, vol. 86, no. 9, pp. 1583–1586, 2011.

- [31] V. Kotov, "Engineering estimates of impurity fluxes on the ITER port plugs," *Nuclear Fusion*, vol. 56, no. 10, p. 106027, 2016.
- [32] V. Kotov, D. Reiter, A. Litnovsky, A. Krimmer, A. Kirschner, and Y. Krasikov, "Passive protection of the ITER diagnostic mirrors," *Physica scripta*, vol. 2011, no. T145, p. 014071, 2011.
- [33] B. Kim, H. G. Lee, C. Seon, S.-G. Oh, and Y. K. Kim, "Suppression of Ag deposition by Ar gas in mtorr range and its implication to mitigation of impurity deposition on first mirrors," *Current Applied Physics*, vol. 15, no. 12, pp. 1615–1619, 2015.
- [34] D. A. C. Bardawil, P. Mertens, G. Offermanns, W. Behr, N. Hawkes, Y. Krasikov, I. Balboa, W. Biel, and U. Samm, "Design overview of the ITER core CXRS fast shutter and manufacturing implications during the detailed design work," *Fusion engineering and design*, vol. 96, pp. 746–750, 2015.
- [35] A. Litnovsky, M. Matveeva, L. Buzi, L. Vera, Y. Krasikov, V. Kotov, A. Panin, P. Wienhold, V. Philipps, D. C. Bardawil *et al.*, "Studies of protection and recovery techniques of diagnostic mirrors for ITER," *Nuclear Fusion*, vol. 55, no. 9, p. 093015, 2015.
- [36] M. Wisse, L. Marot, A. Widdowson, M. Rubel, D. Ivanova, P. Petersson, R. Doerner, M. Baldwin, J. Likonen, E. Alves *et al.*, "Laser-assisted cleaning of beryllium-containing mirror samples from JET and PISCES-B," *Fusion engineering and design*, vol. 89, no. 2, pp. 122–130, 2014.
- [37] A. Maffini, L. Moser, L. Marot, R. Steiner, D. Dellasega, A. Uccello, E. Meyer, and M. Passoni, "In situ cleaning of diagnostic first mirrors: an experimental comparison between plasma and laser cleaning in ITER-relevant conditions," *Nuclear Fusion*, vol. 57, no. 4, p. 046014, 2017.
- [38] I. Arkhipov, A. Gorodetsky, R. Zalavutdinov, V. Bukhovets, A. Zakharov, E. Mukhin, A. Razdobarin, V. Semenov, K. Vukolov, T. Mukhammedzyanov *et al.*, "Development of plasma cleaning techniques for in-vessel optical components in ITER," *Journal of Nuclear Materials*, vol. 415, no. 1, pp. S1210–S1213, 2011.
- [39] V. Bukhovets, A. Gorodetsky, R. K. Zalavutdinov, A. Zakharov, E. Mukhin, and A. Razdobarin, "Sputtering of W and Al in D₂/O₂ plasma cleaning discharge," *Journal of Nuclear Materials*, vol. 463, pp. 255–257, 2015.
- [40] T. Kuschel and A. von Keudell, "Ion-enhanced oxidation of aluminum as a fundamental surface process during target poisoning in reactive magnetron sputtering," *Journal of Applied Physics*, vol. 107, no. 10, p. 103302, 2010.
- [41] A. Rogov, Y. Kapustin, and A. Alekseev, "Application of the penning discharge for cleaning mirrors in optical diagnostics of the ITER," *Instruments & Experimental Techniques*, vol. 58, no. 1, 2015.
- [42] A. Razdobarin, A. Dmitriev, A. Bazhenov, I. Bukreev, M. Kochergin, A. Koval, G. Kurskiev, A. Litvinov, S. Masyukevich, E. Mukhin *et al.*, "RF discharge for in situ mirror surface recovery in ITER," *Nuclear Fusion*, vol. 55, no. 9, p. 093022, 2015.
- [43] J. Peng, L. Chen, R. Yan, J. Chen, D. Zhu, R. Ding, Q. Wang, and Z. Zhang, "Comparative investigations of stainless steel and molybdenum first mirrors cleaning using radio frequency plasma," *Fusion Engineering and Design*, vol. 112, pp. 317–323, 2016.
- [44] R. Yan, R. Ding, J. Chen, and L. Chen, "Experimental studies of first mirror exposure and surface recovery on EAST," *Journal of Nuclear Materials*, vol. 463, pp. 948–951, 2015.
- [45] M. Smiley, R. O'Neill, J. Vasquez, C. Lasnier, A. McLean, R. Feder, M. Smith, A. Jariwala, B. Stratton, D. Johnson *et al.*, "Design update of the ITER upper wide angle viewing system," *Fusion Engineering and Design*, 2017.
- [46] M. A. Lieberman and A. J. Lichtenberg, *Principles of plasma discharges and materials processing*. John Wiley & Sons, 2005.
- [47] K. Köhler, J. Coburn, D. Horne, E. Kay, and J. Keller, "Plasma potentials of 13.56-MHz RF argon glow discharges in a planar system," *Journal of Applied Physics*, vol. 57, no. 1, pp. 59–66, 1985.
- [48] K. Al-Assadi, "Radio frequency sheath characteristics in a plasma sputtering system," *Vacuum*, vol. 43, no. 4, pp. 287–290, 1992.
- [49] E. Kawamura, V. Vahedi, M. Lieberman, and C. Birdsall, "Ion energy distributions in rf sheaths; review, analysis and simulation," *Plasma Sources Science and Technology*, vol. 8, no. 3, p. R45, 1999.

Bibliography

- [50] N. S. J. Braithwaite, "Introduction to gas discharges," *Plasma sources science and technology*, vol. 9, no. 4, p. 517, 2000.
- [51] H. Smith, C. Charles, and R. Boswell, "Breakdown behavior in radio-frequency argon discharges," *Physics of Plasmas*, vol. 10, no. 3, pp. 875–881, 2003.
- [52] O. Popov and V. Godyak, "Power dissipated in low-pressure radio-frequency discharge plasmas," *Journal of applied physics*, vol. 57, no. 1, pp. 53–58, 1985.
- [53] G. Collins and J. Tendys, "Measurements of potentials and sheath formation in plasma immersion ion implantation," *Journal of Vacuum Science & Technology B: Microelectronics and Nanometer Structures Processing, Measurement, and Phenomena*, vol. 12, no. 2, pp. 875–879, 1994.
- [54] A. Aanesland, C. Charles, R. Boswell, and M. Lieberman, "Grounded radio-frequency electrodes in contact with high density plasmas," *Physics of plasmas*, vol. 12, no. 10, p. 103505, 2005.
- [55] A. Aanesland, C. Charles, R. Boswell, and Å. Fredriksen, "Helicon plasma with additional immersed antenna," *Journal of Physics D: Applied Physics*, vol. 37, no. 9, p. 1334, 2004.
- [56] R. Chodura, "Plasma-wall transition in an oblique magnetic field," *The Physics of Fluids*, vol. 25, no. 9, pp. 1628–1633, 1982.
- [57] R. Chodura, "Numerical analysis of plasma-wall interaction for an oblique magnetic field," *Journal of Nuclear Materials*, vol. 111, pp. 420–423, 1982.
- [58] A. DeWald, A. Bailey, and J. Brooks, "Trajectories of charged particles traversing a plasma sheath in an oblique magnetic field," *The Physics of fluids*, vol. 30, no. 1, pp. 267–269, 1987.
- [59] J. P. Gunn, "The influence of magnetization strength on the sheath: Implications for flush-mounted probes," *Physics of Plasmas*, vol. 4, no. 12, pp. 4435–4446, 1997.
- [60] Y. Yamamura and H. Tawara, "Energy dependence of ion-induced sputtering yields from monatomic solids at normal incidence," *Atomic data and nuclear data tables*, vol. 62, no. 2, pp. 149–253, 1996.
- [61] N. Matsunami, Y. Yamamura, Y. Itikawa, N. Itoh, Y. Kazumata, S. Miyagawa, K. Morita, R. Shimizu, and H. Tawara, "Energy dependence of the yields of ion-induced sputtering of monatomic solids," *Unknown*, vol. 1, 1983.
- [62] H. Bay and J. Bohdansky, "Sputtering yields for light ions as a function of angle of incidence," *Applied Physics A: Materials Science & Processing*, vol. 19, no. 4, pp. 421–426, 1979.
- [63] R. T. Sawyer, J. L. Abraham, E. Daniloff, and L. S. Newman, "Secondary ion mass spectroscopy demonstrates retention of beryllium in chronic beryllium disease granulomas," *Journal of occupational and environmental medicine*, vol. 47, no. 12, pp. 1218–1226, 2005.
- [64] L. Marot, C. Linsmeier, B. Eren, L. Moser, R. Steiner, and E. Meyer, "Can aluminium or magnesium be a surrogate for beryllium: A critical investigation of their chemistry," *Fusion engineering and design*, vol. 88, no. 9, pp. 1718–1721, 2013.
- [65] R. Doerner, A. Grossman, S. Luckhardt, R. Seraydarian, F. Sze, D. Whyte, and R. Conn, "Response of beryllium to deuterium plasma bombardment," *Journal of nuclear materials*, vol. 257, no. 1, pp. 51–58, 1998.
- [66] C. Steinbrüchel, "On the sputtering yield of molecular ions," *Journal of Vacuum Science & Technology A: Vacuum, Surfaces, and Films*, vol. 3, no. 5, pp. 1913–1915, 1985.
- [67] C. Björkas, K. Vörtler, K. Nordlund, D. Nishijima, and R. Doerner, "Chemical sputtering of Be due to D bombardment," *New Journal of Physics*, vol. 11, no. 12, p. 123017, 2009.
- [68] *ALADDIN Database*, Std. [Online]. Available: <http://www-amdis.iaea.org/ALADDIN>
- [69] T. Goodman *et al.*, "Experience in integrated control of the multi-megawatt electron cyclotron heating system on the TCV tokamak: the first decade," *Nuclear Fusion*, vol. 48, no. 5, p. 054011, 2008.
- [70] S. Hüfner, *Photoelectron spectroscopy: principles and applications*. Springer Science & Business Media, 2013.
- [71] J. Walls and R. Smith, "Surface science techniques," *Vacuum*, vol. 45, no. 6-7, pp. 649–652, 1994.
- [72] R. Hesse, T. Chassé, and R. Szargan, "Peak shape analysis of core level photoelectron spectra using UNIFIT for WINDOWS," *Fresenius' journal of analytical chemistry*, vol. 365, no. 1, pp. 48–54, 1999.

- [73] B. Eren, L. Marot, M. Langer, R. Steiner, M. Wisse, D. Mathys, and E. Meyer, "The effect of low temperature deuterium plasma on molybdenum reflectivity," *Nuclear Fusion*, vol. 51, no. 10, p. 103025, 2011.
- [74] J. Goldstein, D. E. Newbury, P. Echlin, D. C. Joy, A. D. Romig Jr, C. E. Lyman, C. Fiori, and E. Lifshin, *Scanning electron microscopy and X-ray microanalysis: a text for biologists, materials scientists, and geologists*. Springer Science & Business Media, 2012.
- [75] J. Pouchou and F. Pichoir, "Electron probe X-ray microanalysis applied to thin surface films and stratified specimens," *Scanning Microscopy International(USA)*, pp. 167–190, 1992.
- [76] D. G. Rickerby and J.-F. Thiot, "X-ray microanalysis of thin film layered specimens containing light elements," *Microchimica Acta*, vol. 114, no. 1, pp. 421–429, 1994.
- [77] F. Galbert, "Measurement of carbon layer thickness with EPMA and the thin film analysis software STRATAGEM," *Microscopy and Microanalysis*, vol. 13, no. S03, pp. 96–97, 2007.
- [78] H. Bennett and J. Porteus, "Relation between surface roughness and specular reflectance at normal incidence," *JOSA*, vol. 51, no. 2, pp. 123–129, 1961.
- [79] M. Wisse, B. Eren, L. Marot, R. Steiner, and E. Meyer, "Spectroscopic reflectometry of mirror surfaces during plasma exposure," *Review of scientific instruments*, vol. 83, no. 1, p. 013509, 2012.
- [80] R. L. Merlino, "Understanding langmuir probe current-voltage characteristics," *American Journal of Physics*, vol. 75, no. 12, pp. 1078–1085, 2007.
- [81] C. Hayden, D. Gahan, and M. Hopkins, "Ion energy distributions at a capacitively and directly coupled electrode immersed in a plasma generated by a remote source," *Plasma Sources Science and Technology*, vol. 18, no. 2, p. 025018, 2009.
- [82] M. Volmer and A. Weber, "Keimbildung in übersättigten Gebilden," *Z. phys. Chem*, vol. 119, no. 3/4, pp. 277–301, 1926.
- [83] P. Barna and M. Adamik, "Fundamental structure forming phenomena of polycrystalline films and the structure zone models," *Thin solid films*, vol. 317, no. 1, pp. 27–33, 1998.
- [84] B. Eren, L. Marot, A. Litnovsky, M. Matveeva, R. Steiner, V. Emberger, M. Wisse, D. Mathys, G. Covarel, and E. Meyer, "Reflective metallic coatings for first mirrors on ITER," *Fusion Engineering and Design*, vol. 86, no. 9, pp. 2593–2596, 2011.
- [85] E. D. Palik, *Handbook of optical constants of solids*. Academic press, 1998, vol. 3.
- [86] B. Eren, L. Marot, M. Wisse, D. Mathys, M. Joanny, J.-M. Travère, R. Steiner, and E. Meyer, "In situ evaluation of the reflectivity of molybdenum and rhodium coatings in an ITER-like mixed environment," *Journal of Nuclear Materials*, vol. 438, pp. S852–S855, 2013.
- [87] Y. Kapustin, A. Rogov, D. Vukolov, A. Gorbunov, and KTO team, "The integration of DC/PDC cleaning system electrodes into H-alpha diagnostic first mirror unit," January. [Online]. Available: <https://user.iter.org/default.aspx?uid=U5XTHL>
- [88] V. Godyak and R. Piejak, "Abnormally low electron energy and heating-mode transition in a low-pressure argon RF discharge at 13.56 mhz," *Physical review letters*, vol. 65, no. 8, p. 996, 1990.
- [89] V. A. Godyak, R. Piejak, and B. Alexandrovich, "Measurement of electron energy distribution in low-pressure RF discharges," *Plasma sources science and technology*, vol. 1, no. 1, p. 36, 1992.
- [90] C. Deegan, "Characterisation of the heating mechanisms in a capacitively coupled argon RF discharge," Ph.D. dissertation, School of Physical Sciences, Dublin City University, July 1999.
- [91] A. Melzer, R. Flohr, and A. Piel, "Comparison of probe measurements and emission spectroscopy in a radiofrequency discharge," *Plasma Sources Science and Technology*, vol. 4, no. 3, p. 424, 1995.
- [92] M. Surendra and D. B. Graves, "Particle simulations of radio-frequency glow discharges," *IEEE Transactions on Plasma Science*, vol. 19, no. 2, pp. 144–157, 1991.
- [93] M. Surendra and D. Graves, "Capacitively coupled glow discharges at frequencies above 13.56 MHz," *Applied physics letters*, vol. 59, no. 17, pp. 2091–2093, 1991.
- [94] W. Schwarzenbach, A. Howling, M. Fivaz, S. Brunner, and C. Hollenstein, "Sheath impedance effects in very high frequency plasma experiments," *Journal of Vacuum Science & Technology A: Vacuum, Surfaces, and Films*, vol. 14, no. 1, pp. 132–138, 1996.

Bibliography

- [95] A. Perret, P. Chabert, J.-P. Booth, J. Jolly, J. Guillon, and P. Auvray, "Ion flux nonuniformities in large-area high-frequency capacitive discharges," *Applied physics letters*, vol. 83, no. 2, pp. 243–245, 2003.
- [96] H. Schmidt, "Characterization of a high-density, large-area VHF plasma source," Ph.D. dissertation, EPFL, 2006.
- [97] Z. Donko, "Particle simulation methods for studies of low-pressure plasma sources," *Plasma Sources Science and Technology*, vol. 20, no. 2, p. 024001, 2011. [Online]. Available: <http://stacks.iop.org/0963-0252/20/i=2/a=024001>
- [98] M. Turner, D. Hutchinson, R. Doyle, and M. Hopkins, "Heating mode transition induced by a magnetic field in a capacitive rf discharge," *Physical review letters*, vol. 76, no. 12, p. 2069, 1996.
- [99] S. Avtaeva, M. Mamytbekov, and D. Otorbaev, "Diagnostics of magnetically enhanced RF discharges in methane, argon and methane-argon mixtures," *Journal of Physics D: Applied Physics*, vol. 30, no. 21, p. 3000, 1997.
- [100] D. Hutchinson, M. Turner, R. Doyle, and M. Hopkins, "The effects of a small transverse magnetic field upon a capacitively coupled RF discharge," *IEEE transactions on plasma science*, vol. 23, no. 4, pp. 636–643, 1995.
- [101] S. You, T. Hai, M. Park, D. Kim, J. Kim, D. Seong, Y. Shin, S. Lee, G. Park, J. Lee *et al.*, "Role of transverse magnetic field in the capacitive discharge," *Thin Solid Films*, vol. 519, no. 20, pp. 6981–6989, 2011.
- [102] Z. Sun, X. Shi, and E. Liu, "High rate deposition of diamond-like carbon films by magnetically enhanced plasma CVD," *Thin Solid Films*, vol. 355, pp. 146–150, 1999.
- [103] S. You, C. Chung, K. Bai, and H.-Y. Chang, "Power dissipation mode transition by a magnetic field," *Applied physics letters*, vol. 81, no. 14, pp. 2529–2531, 2002.
- [104] S. Lee, S. You, H.-Y. Chang, and J. Lee, "Electron and ion kinetics in magnetized capacitively coupled plasma source," *Journal of Vacuum Science & Technology A: Vacuum, Surfaces, and Films*, vol. 25, no. 3, pp. 455–463, 2007.
- [105] V. D. Bruggeman, "Berechnung verschiedener physikalischer Konstanten von heterogenen Substanzen. i. Dielektrizitätskonstanten und Leitfähigkeiten der Mischkörper aus isotropen Substanzen," *Annalen der physik*, vol. 416, no. 7, pp. 636–664, 1935.
- [106] K. Sabat, P. Rajput, R. Paramguru, B. Bhoi, and B. Mishra, "Reduction of oxide minerals by hydrogen plasma: An overview," *Plasma Chemistry and Plasma Processing*, vol. 34, no. 1, pp. 1–23, 2014.
- [107] J. Baltrusaitis, B. Mendoza-Sanchez, V. Fernandez, R. Veenstra, N. Dukstiene, A. Roberts, and N. Fairley, "Generalized molybdenum oxide surface chemical state XPS determination via informed amorphous sample model," *Applied Surface Science*, vol. 326, pp. 151–161, 2015.
- [108] K. Oshikawa, M. Nagai, and S. Omi, "Characterization of molybdenum carbides for methane reforming by TPR, XRD, and XPS," *The Journal of Physical Chemistry B*, vol. 105, no. 38, pp. 9124–9131, 2001.
- [109] D. O. Scanlon, G. W. Watson, D. Payne, G. Atkinson, R. Egdell, and D. Law, "Theoretical and experimental study of the electronic structures of MoO₃ and MoO₂," *The Journal of Physical Chemistry C*, vol. 114, no. 10, pp. 4636–4645, 2010.
- [110] J.-G. Choi and L. Thompson, "XPS study of as-prepared and reduced molybdenum oxides," *Applied Surface Science*, vol. 93, no. 2, pp. 143–149, 1996.
- [111] C. Skinner, C. Gentile, and R. Doerner, "Simultaneous imaging/reflectivity measurements to assess diagnostic mirror cleaning," *Review of Scientific Instruments*, vol. 83, no. 10, p. 10D512, 2012.
- [112] L. Marot, G. De Temmerman, P. Oelhafen, G. Covarel, and A. Litnovsky, "Rhodium coated mirrors deposited by magnetron sputtering for fusion applications," *Review of scientific instruments*, vol. 78, no. 10, p. 103507, 2007.
- [113] M. J. Rubel, G. De Temmerman, J. Coad, J. Vince, J. R. Drake, F. Le Guern, A. Murari, R. Pitts, C. Walker, J.-E. Contributors *et al.*, "Mirror test for International Thermonuclear Experimental Reactor at the JET tokamak: An overview of the program," *Review of scientific instruments*, vol. 77, no. 6, p. 063501, 2006.

- [114] E. Macak, W.-D. Münz, and J. Rodenburg, "Plasma–surface interaction at sharp edges and corners during ion-assisted physical vapor deposition. Part I: Edge-related effects and their influence on coating morphology and composition," *Journal of applied physics*, vol. 94, no. 5, pp. 2829–2836, 2003.
- [115] P. Bruzzone, A. Anghel, A. Fuchs, G. Pasztor, B. Stepanov, M. Vogel, and G. Vecsey, "Upgrade of operating range for SULTAN test facility," *IEEE transactions on applied superconductivity*, vol. 12, no. 1, pp. 520–523, 2002.
- [116] U. Konopka, M. Schwabe, C. Knapek, M. Kretschmer, G. Morfill, L. Boufendi, M. Mikikian, and P. Shukla, "Complex plasmas in strong magnetic field environments," in *AIP Conference Proceedings*, vol. 799, no. 1. AIP, 2005, pp. 181–184.
- [117] M. Schwabe, U. Konopka, P. Bandyopadhyay, and G. Morfill, "Pattern formation in a complex plasma in high magnetic fields," *Physical review letters*, vol. 106, no. 21, p. 215004, 2011.
- [118] E. Thomas Jr, U. Konopka, R. L. Merlino, and M. Rosenberg, "Initial measurements of two- and three-dimensional ordering, waves, and plasma filamentation in the magnetized dusty plasma experiment," *Physics of Plasmas*, vol. 23, no. 5, p. 055701, 2016.
- [119] H. Shin, K. Noguchi, X.-Y. Qian, N. Jha, G. Hills, and C. Hu, "Spatial distributions of thin oxide charging in reactive ion etcher and MERIE etcher," *IEEE electron device letters*, vol. 14, no. 2, pp. 88–90, 1993.
- [120] M. Tanabe, A. Matsuda, T. Sunada, H. Fujimoto, and T. Hayashi, "Reactive ion etching of Al alloy films in a rotating magnetic field," *Japanese journal of applied physics*, vol. 32, no. 2R, p. 747, 1993.
- [121] C.-Y. Hsu, L.-Y. Chen, and F. C.-N. Hong, "Properties of diamond-like carbon films deposited by ion plating with a pulsed substrate bias," *Diamond and related materials*, vol. 7, no. 6, pp. 884–891, 1998.
- [122] E. Barnat, P. Miller, and A. Paterson, "RF discharge under the influence of a transverse magnetic field," *Plasma Sources Science and Technology*, vol. 17, no. 4, p. 045005, 2008.
- [123] Y. Fan, Y. Zou, J. Sun, T. Stirner, and D. Wang, "Study of the effects of a transverse magnetic field on radio frequency argon discharges by two-dimensional particle-in-cell-Monte-Carlo collision simulations," *Physics of Plasmas*, vol. 20, no. 10, p. 103507, 2013.
- [124] R. Ding, P. Stangeby, D. Rudakov, J. Elder, D. Tskhakaya, W. Wampler, A. Kirschner, A. McLean, H. Guo, V. Chan *et al.*, "Simulation of gross and net erosion of high-Z materials in the DIII-D divertor," *Nuclear Fusion*, vol. 56, no. 1, p. 016021, 2015.
- [125] R. Ding, D. Rudakov, P. Stangeby, W. Wampler, T. Abrams, S. Brezinsek, A. Briesemeister, I. Bykov, V. Chan, C. Chrobak *et al.*, "Advances in understanding of high-Z material erosion and re-deposition in low-Z wall environment in DIII-D," *Nuclear Fusion*, vol. 57, no. 5, p. 056016, 2017.
- [126] N. Mellet, J. Gunn, B. Pégourié, Y. Marandet, C. Martin, and P. Roubin, "Tungsten erosion by impurities and redeposition: focus on the magnetised sheath," *Plasma Physics and Controlled Fusion*, vol. 59, no. 3, p. 035006, 2017.
- [127] T. Ibehej and R. Hrach, "Computational Study of Sheath Structure in the Presence of Magnetic Field," *WDS 12 Proceedings of Contributed Papers: Part II – Physics of Plasmas and Ionized Media*, vol. Prague, no. eds. J. Safrankova and J. Pavlu, pp. 81–86, 2012.
- [128] J. Li, H. Guo, B. Wan, X. Gong, Y. Liang, G. Xu, K. Gan, J. Hu, H. Wang, L. Wang *et al.*, "A long-pulse high-confinement plasma regime in the Experimental Advanced Superconducting Tokamak," *Nature physics*, vol. 9, no. 12, pp. 817–821, 2013.
- [129] F. Ding, G.-N. Luo, R. A. Pitts, A. Litnovsky, X. Gong, R. Ding, H. Mao, H. Zhou, W. R. Wampler, P. C. Stangeby *et al.*, "Overview of plasma–material interaction experiments on EAST employing MAPES," *Journal of Nuclear Materials*, vol. 455, no. 1, pp. 710–716, 2014.
- [130] F. Leipold, R. Reichle, C. Vorpahl, E. Mukhin, A. Dmitriev, A. Razdobarin, D. Samsonov, L. Marot, L. Moser, R. Steiner *et al.*, "Cleaning of first mirrors in ITER by means of radio frequency discharges," *Review of Scientific Instruments*, vol. 87, no. 11, p. 11D439, 2016.
- [131] S. Dickheuer, O. Marchuk, C. Brandt, and A. Pospieszczyk, "Spectral Emission of fast non-Maxwellian Atoms at metallic Surfaces in low density Plasmas," in *69th Annual Gaseous Electronics Conference*, 2016.

List of Symbols and Abbreviations

Symbols

ω : Angular frequency
 A_g : Area grounded electrode
 I_g : Current grounded electrode
 C_g : Capacitance grounded electrode
 A_d : Area driven electrode
 I_d : Current driven electrode
 C_d : Capacitance driven electrode
 λ_D : Debye length
 d : Electrode gap
 e : Elementary charge
 E : Electric field
 E : Energy
 E_B : Binding energy
 $h\nu$: Photon energy
 λ_{MFP} : Mean free path
 λ : Wavelength
 λ_0 : Wavelength in vacuum
 λ_{cable} : Wavelength in transmission line
 ρ_i : Larmor radius
 m_e : Electron mass
 m_i : Ion mass
 n_e : Electron density
 n_i : Ion density
 p : Pressure
 q : Charge particle
 R_a : Average roughness
 R_{rms} : Root mean square roughness
 R_{Tot} : Total reflectivity
 R_{Diff} : Diffuse reflectivity
 R_{Spec} : Specular reflectivity
 \tilde{R} : Relative reflectivity
 R_{\neq} : Inhomogeneity factor
 $R_{B/no B}$: Ratio erosion rates

T: Temperature
 T_e : Electron temperature
 T_i : Ion temperature
 v : Velocity
V: Voltage
 V_0 : RF Voltage
 V_{bias} : Self-bias
 V_{Brk} : Breakdown voltage
 V_p : Plasma potential

Elements and other materials

Al: Aluminum
Ar: Argon
Au: Gold
Be: Beryllium
C: Carbon
Cu: Copper
D: Deuterium
H: Hydrogen
He: Helium
Inc: Inconels
Mg: Magnesium
Mo: Molybdenum
N: Nitrogen
Ne: Neon
O: Oxygen
PTFE: Polytetrafluoroethylene
Rh: Rhodium
Si: Silicon
SS: Stainless steel
T: Tritium
W: Tungsten

List of Symbols and Abbreviations

Experimental

ALD: Atomic layer deposition
EDX: Energy dispersive X-ray (analysis)
ERDA: Elastic recoil detection analysis
ESCA: Electron spectroscopy for chemical analysis
IBA: Ion beam analysis
QMB: Quartz micro-balance
NRA: Nuclear reaction analysis
PVD: Physical vapor deposition
RBS: Rutherford backscattering spectrometry
RFEA: Retarding field energy analyser
SEM: Scanning electron microscopy
SIMS: Secondary ion mass spectroscopy
TVA: Thermionic vacuum arc
XPS: X-ray photoelectron spectroscopy
XRD: X-ray diffraction

Units

°: Degrees
°C: Degrees Celcius
Å: Ångströms
eV: Electron volts
Hz: Hertz
K: Kelvin
Pa: Pascal
g: Grams
h: Hours
m: Meters
min: Minutes
s: Seconds
V: Volts
W: Watts
Ω: Ohms
T: Tesla

Facilities

ASDEX Upgrade: Axially Symmetric Divertor Experiment Upgrade
BeHF: Beryllium Handling Facility
EAST: Experimental Advanced Superconduct-

ing Tokamak

EPFL: Ecole Polytechnique Fédérale de Lausanne
INFLPR: National Institute For Laser and Radiation Physics
ITER: International Thermonuclear Experiment Reactor
JET: Joint European Torus, ILW: ITER-like Wall
MAPES: Material and Plasma Evaluation System in EAST
SPC: Swiss Plasma Center
TEXTOR: Tokamak Experiment for Technology Oriented Research
UCSD: University of California San Diego

ITER technical

CXNs: Charge eXchange Neutrals
CXRS: Charge eXchange Recombination Spectroscopy
ETS: Edge Thomson Scattering
FW: First Wall
FMs: First Mirrors
PFCs: Plasma Facing Components
WAVS: Wide Angle Viewing System

Others

AC: Alternative current
CCP: Capacitively coupled plasma
DC: Direct current
 E_{Th} : Sputtering threshold
LTP: Low-temperature plasma
MPS: Magnetized pre-sheath
RF: Radio frequency
SE: Secondary electrons
UV: Ultraviolet
Vis: Visible
NIR: Near-infrared
UHV: Ultra-high vacuum
Y: Sputtering yield

Acknowledgements

It is never an easy task to write down acknowledgements on paper, but in the present case, it is with a lot of envy that I do it. The majority of the results presented in this thesis were achieved at the University of Basel in the surface physics facilities of Prof. Dr. Ernst Meyer but also in close collaborations with several top-leading institutions.

First of all, I would like to thank Prof. Dr. Ernst Meyer for giving me the opportunity to carry out this thesis. Although the topic of this thesis does not fall in his domain of predilection, his wide knowledge in science, encouraging comments and liberty he allocates to Ph.D. student made everything possible.

This thesis was done under the supervision of Dr. Laurent Marot, my advisor. When I first met him, I did not intend to do a Ph.D. thesis and thought that doing my Master thesis with him, I would have the chance to add my modest contribution to the ITER project. After 6 months under his supervision and a trip together to the ITER Organization site, I decided to extend the adventure for four more years, probably the best decision I ever made, after the one of marrying my wife but I will come to that later ... He provided the best possible working environment for me, sharing his knowledge and skills with me, providing me a rigorous and unconstrained framework at the same time. No matter what, I knew he would stand behind me. Thank you Boss!

Furthermore, I want to thank Roland Steiner, the engineer and endless source of knowledge of our group. I needed six months to understand that he is not only believing that he is always right but he truly is. Even after 4 years spent with him, I am still amazed when he recounts experiences they performed 20 or even 30 years ago in the group. He awoke the engineer sleeping inside of me, this little kid that used to play with his Lego, and for that I am very grateful.

During my Master thesis, I had the chance to meet responsible of the ITER Organization whose motivated me to continue my work: Mike Walsh and Roger Reichle. Thank you for believing in our work and always supporting us through the years. Also, I am very grateful to Frank Leipold, Christian Vorpahl and Frédéric Le Guern for the scientific discussions.

I was given the opportunity to travel to the whole world to conduct my experiences. I always spent an unforgettable time, both scientifically and socially. Thanks to the JET Be-HF team, Ian, Anna, Mark and Charlie, the team from the SPC, Ivo, Stefano, Stéphane and Miguel, and the EAST team, Rong, Jiao and Baoguo.

My special thanks go to all our group members, for their support and for making these 4 years the best working experience I will probably ever have. Sara, Marwa, Dilek, Tobias, Zhao, Matze, Res, Carl, Antoine, Rémy, Marcin, Shigeki, Thilo and Alexis I will all miss you a lot ... A part of our group, two more persons were always supporting me and making my days: Olha and Zack, don't change and stay as you are!

In addition, I would like to express my gratitude to the electrical and mechanical workshop

Acknowledgements

of our department but also to the team of the ‘Nano Imaging Lab’ in Basel.

I am very thankful to all my friends, Jacques, Sophie, Jules, Marie, Nicolas Elodie, Anthony, Sandrinette, Raphaël, Hakim, Marine, Lionel, Richir, Stéphanie, Fabien, Céline and Simon. Especially I want to thank Sandrine, who never forgot me.

Finally, I would like to thank my family. My parents who always supported me during my studies and my brother, Fabian, who never stopped believing in me. Little bro, now it is your turn, I believe in you!

Keeping the best part for the end, I would like to thank my wife. Every day I feel myself blessed for meeting her almost 10 years ago. I will never forget this moment, you dressed as a Hippie, me as a clown... Remember how we laughed when we discussed explaining how we met to our children. I guess will have few more years to come out with a good story for Margot. You truly are an exceptional woman, always supportive and patient. If it were not for you, I would not be doing a Ph.D. Like they say, behind every man, there is a woman, and you never quit. This work, I dedicate to you, “mon chou”.

List of publications & communications

Peer-reviewed journal publications

The original contents of this PhD thesis have led to the publication of the following peer-reviewed papers, ordered by year:

- **L. Moser**, L. Marot, R. Steiner, R. Reichle, F. Leipold, C. Vorpahl, F. Le Guern, U. Walach, S. Alberti, I. Furno, R. Yan, J. Peng, M. Ben Yaala and E. Meyer. Plasma Cleaning of ITER First Mirrors. Submitted to *Physica Scripta*.
- R. Yan, **L. Moser**, B. Wang, J. Peng, C. Vorpahl, F. Leipold, R. Reichle, R. Ding, J. Chen, L. Mu, R. Steiner, E. Meyer, M. Zhao, J. Wu and L. Marot. Plasma cleaning of ITER edge Thomson scattering mock-up mirror in EAST tokamak. Under revision in *Nuclear Fusion*.
- K. Thodkar, D. Thompson, F. Lüönd, **L. Moser**, F. Overney, L. Marot, C. Schönenberger, B. Jeanneret and M. Calame. Restoring the electrical properties of CVD graphene via physisorption of molecular adsorbates. Submitted to *ACS Applied Materials & Interfaces*.
- L. Marot, S. Coda, S. Kajita, **L. Moser**, R. Steiner, and E. Meyer. TCV mirrors cleaned by plasma. Under revision in *Nuclear Materials & Energy*.
- **L. Moser**, R.P. Doerner, M.J. Baldwin, C.P. Lungu, C. Porosnicu, M. Newman, A. Widdowson, E. Alves, G. Pintsuk, J. Likonen, A. Hakola, R. Steiner, L. Marot, E. Meyer and JET Contributors. Investigation and plasma cleaning of first mirrors coated with relevant ITER contaminants: beryllium and tungsten. *Nuclear Fusion* 2017. <https://doi.org/10.1088/1741-4326/aa73e2>.
- A. Maffini, **L. Moser**, L. Marot, R. Steiner, D. Dellasega, A. Uccello, E. Meyer and M. Passoni. In situ cleaning of diagnostic first mirrors: an experimental comparison between plasma and laser cleaning in ITER-relevant conditions. *Nuclear Fusion*, **57**, 046014, 2017.
- **L. Moser**, L. Marot, R. Steiner, M. Newman, A. Widdowson, D. Ivanova, J. Likonen, P. Petersson, G. Pintsuk, M. Rubel, E. Meyer and JET Contributors. Plasma cleaning of beryllium coated mirrors. *Physica Scripta*, **T167**, 014069, 2016.
- F. Leipold, R. Reichle, C. Vorpahl, E. E. Mukhin, A. M. Dmitriev, A. G. Razdobarin, D. S. Samsonov, L. Marot, **L. Moser**, R. Steiner, E. Meyer. Cleaning of first mirrors in ITER by means of radio frequency discharges. *Review of Scientific Instruments*, **87**, 11D439, 2016.

List of publications & communications

- M.F.M. De Bock, R. Barnsley, M. Bassan, L. Bertalot, B. Brichard, I.M. Bukreev, J.M. Drevon, F. Le Guern, R. Hutton, M. Ivantsivskiy, H.G. Lee, F. Leipold, P. Maquet, L. Marot, V. Martin, P. Mertens, A. Mokeev, **L. Moser**, E.E. Mukhin, S. Pak, A.G. Razdobarin, R. Reichle, C.R. Seon, F. Seyvet, S. Simrock, V. Udintsev, G. Vayakis and C. Vorpahl. ITER perspective on fusion reactor diagnostics - A spectroscopic view. *Journal of Instrumentation*, **11.08**, P08010, 2016.
- **L. Moser**, B. Eren, M. Wisse, R. Steiner, D. Mathys, R. Reichle, F. Leipold, L. Marot, and E. Meyer. Towards plasma cleaning of ITER first mirrors. *Nuclear Fusion*, **55**, 063020, 2015.
- **L. Moser**, R. Steiner, F. Leipold, R. Reichle, L. Marot, E. Meyer. Plasma cleaning of ITER First Mirrors in magnetic field. *Journal of Nuclear Materials*, **463**, 940–943, 2015.
- S. Iyyakkunnel, L. Marot, B. Eren, R. Steiner, **L. Moser**, D. Mathys, M. Dueggelin, P. Chapon, E. Meyer. Morphological changes of tungsten surfaces by low-flux helium plasma treatment and helium incorporation via magnetron sputtering. *ACS applied materials & interfaces*, **6**, 11609–11616, 2014.
- L. Marot, C. Linsmeier, B. Eren, **L. Moser**, R. Steiner, E. Meyer. Can aluminium or magnesium be a surrogate for beryllium: A critical investigation of their chemistry. *Fusion Eng. Des.*, **88**, 1718–1721, 2013.

Scientific communications

Due to the large number, only presentations in which L. Moser was first author will be listed:

- **L. Moser**, L. Marot, R. Steiner, R. Reichle, F. Leipold, S. Alberti, I. Furno and E. Meyer. *Influence of high magnetic field on plasma sputtering of ITER First Mirrors*. 31th Meeting of the ITPA Topical Group on Diagnostics. ITER Organization (France), November 2016. Oral presentation.
- **L. Moser**, L. Marot, R. Steiner, S. Alberti, I. Furno, F. Leipold, R. Reichle and E. Meyer. *Investigation of erosion patterns in highly magnetized CCP for ITER First Mirrors applications*. Swiss Physical Society Annual Meeting, Lugano (Switzerland), August 2016.
- **L. Moser**, L. Marot, R. Steiner, R. Reichle, F. Leipold, S. Alberti, I. Furno and E. Meyer. *Influence of high magnetic field on plasma sputtering of ITER First Mirrors*. FuseNet PhD Event 5. Prague (Czech Republic), November 2015. Oral presentation.
- **L. Moser**, L. Marot, R. Steiner, R. Reichle, F. Leipold, S. Alberti, I. Furno and E. Meyer. *Advancement/update on plasma cleaning in magnetic field*. 29th Meeting of the ITPA Topical Group on Diagnostics, ITER Organization (France), 05 November 2015. Oral presentation.
- **L. Moser**, L. Marot, R. Steiner, S. Alberti, I. Furno, F. Leipold, R. Reichle and E. Meyer. *Influence of high magnetic field on plasma sputtering of ITER First Mirrors*. Swiss Physical Society Annual Meeting, Vienna (Austria), September 2015.
- **L. Moser**, L. Marot, R. Steiner, M. Newman, A. Widdowson, D. Ivanova, R. P. Doerner, C. P. Lungu, C. Porosnicu, J. Likonen, E. Alves, P. Petersson, G. Pintsuk, M. Rubel, E. Meyer and JET Contributors. *Plasma cleaning of Be coated mirrors*. 15th International Conference on Plasma-Facing Materials and Components for Fusion Applications (PFMC-15). Aix en Provence (France), May 2015. Poster presentation.
- **L. Moser**, R. Steiner, D. Mathys, R. Reichle, F. Leipold, L. Marot, E. Meyer, S. Alberti and I. Furno. *Plasma Cleaning of First Mirrors in ITER-like conditions*. 1st EPS Conference on Plasma Diagnostics. Villa Mondragone (Italy), April 2015. Poster presentation and price for Best Student Poster.

- **L. Moser**, L. Marot, R. Steiner, R. Reichle, F. Leipold, S. Alberti, I. Furno and E. Meyer. *Plasma cleaning in ITER-like conditions*. 27th Meeting of the ITPA Topical Group on Diagnostics, ITER Organization (France), 03–07 November 2014. Oral presentation.
- **L. Moser**, L. Marot, R. Steiner, M. Husistein, M. Jenni, B. Stepanov, P. Bruzzone, S. Alberti, I. Furno and E. Meyer. *Influence of magnetic field on plasma sputtering of ITER First Mirrors*. Swiss Physical Society Annual Meeting, Fribourg (Switzerland), July 2014.
- **L. Moser**, R. Steiner, R. Reichle, F. Leipold, L. Marot and E. Meyer. *Plasma cleaning of ITER first mirrors in magnetic field*. 21st International Conference on Plasma Surface Interactions in Controlled Fusion Devices Conference (PSI-21). Kanazawa (Japan), May 2014. Poster presentation.
- **L. Moser**, L. Marot, R. Steiner, R. Reichle, F. Leipold, S. Alberti, I. Furno and E. Meyer. *Plasma cleaning in ITER-like conditions*. 2nd Mirror Cleaning Workshop. ITER Organization (France), 09–10 February 2014. Oral presentation.
- **L. Moser**, L. Marot, R. Steiner, B. Eren, R. Reichle, F. Leipold, M. Husistein, M. Jenni, B. Stepanov, P. Bruzzone and E. Meyer. *RF plasma cleaning for ITER First Mirror*. 25th Meeting of the ITPA Topical Group on Diagnostics. ITER Organization (France), 15–18 October 2013. Oral presentation.
- **L. Moser**, B. Eren, M. Wisse, R. Steiner, D. Mathys, R. Reichle, F. Leipold, L. Marot and E. Meyer. *Towards Plasma Cleaning of ITER First Mirrors*. 14th International Conference on Plasma-Facing Materials and Components for Fusion Applications (PFMC-14). Jülich (Germany), May 2013. Poster presentation.
- **L. Moser**, L. Marot, R. Steiner, B. Eren and E. Meyer. *Development of a Concept Design for a Plasma Sputtering Cleaning System for ITER Diagnostic First Mirrors*. 1st Mirror Cleaning Workshop. ITER Organization (France), April 2013. Oral presentation.

Curriculum Vitae

Lucas Moser – 12 rue des Landes – 68220 Héisingue France

📞 +33 677932736 • ✉ lucas.moser.pro@gmail.com
🌐 <https://www.linkedin.com/in/lucas-moser-900725a2/>

Currently a last year Ph.D. in applied physics with focus on plasma-material interactions. Passionate about science I am interested in interdisciplinary activities and hands-on projects with technical and engineering issues.

Key skills

- **Technical skills:** Plasma and Vacuum techniques, Thin Films coatings, Ion-induced surface modification, Plasma catalysis.
- **Characterization techniques:** X-Ray Photoelectron Spectroscopy, Scanning Electron Microscopy, Energy Dispersive X-Ray Analysis, Ellipsometry, Langmuir probe, Retarding Field Energy Analyser, Plasma Optical Emission Spectroscopy.
- **Management:** Management of lab projects with undergraduate students, responsible for vacuum facility, supervision of international experimental campaigns.
- **Communication:** Academic writing, reports for project advancement, conference talks and poster presentations, excellent interpersonal skills and effective team player.
- **Programming:** Matlab, TeX, Pack Office
Also basic knowledge of SolidWorks and LabView.

Education

- **University of Basel, Switzerland** **2013–present**
Ph.D. student in Physics
Plasma cleaning of diagnostic First mirrors for the nuclear fusions machine ITER.
- **University of Basel, Switzerland** **2010–2012**
Master of Physics
Focus in Nanomechanics and Solid-state physics.

- **University of Strasbourg, France** **2009–2010**
Bachelor in Physics, 3rd year
Physics and Engineering Sciences.
- **Highschool A. Schweizer, Mulhouse, France** **2007–2009**
“Classes Préparatoires aux Grandes Ecoles”
Mathematics, Physics and Chemistry.
- **Highschool J. Mermoz, Saint-Louis, France** **2007**
Baccalauréat Scientifique

Languages

- **French:** Native speaker
- **German:** Fluent
- **English:** Fluent
- **Portuguese:** Beginner

Interests and extra-curricular activity

Outdoor sport, Swimming, Yoga, Gardening, DIY, modelling, reading.

Publications and Awards

- All first-author and co-authored publications are available on:
https://nanolino.unibas.ch/pages/group.htm?id=group&subid=lucas_moser
- Commendation during the ITER Recognition Ceremony held in December 2014.
<https://www.iter.org/newsline/-/2153>
- Poster Prize at the 1st EPS Conference on Plasma Diagnostics held in Frascati, Italy, April 2015.